Magnetoresistance Effects in Emerging Two-dimensional Materials and Chiral Nanostructures

by

Seyedamin Firouzeh

A thesis submitted in partial fulfillment of the requirements for the degree of

Doctor of Philosophy

In
Microsystems and Nanodevices

Department of Electrical and Computer Engineering
University of Alberta

Abstract

Spintronics, also known as "spin-based electronics," merges electronics and magnetism at the nanoscale and holds great promise for emerging quantum technologies and the next generation of data storage and sensing devices. Reducing the size of current spintronics devices with conventional magnetic materials presents a challenging task. To overcome these challenges, researchers are exploring several approaches, two of which will be investigated in this thesis.

The first approach relies on the two-dimensional (2D) van der Waals (vdW) materials due to their mechanical flexibility and sensitivity to band structure and defect engineering. These properties make them attractive candidates for future spintronic applications with further miniaturization. Recently 2D magnetic materials have been discovered, which exhibit large magnetoresistance (MR) effects, albeit only at cryogenic temperatures, limiting their practicality. To further investigate this issue, this thesis focuses on vanadium diselenide (VSe_2), a promising 2D material which has the potential for exhibiting room temperature ferromagnetism at the monolayer level. We have established a reproducible nanofabrication method to investigate thin flakes of this material in an out-of-plane geometry. We have observed significant positive linear MR effects (~60–70%) at room temperature, under a relatively small magnetic field range of 12kG. The MR originates due to the intrinsic inhomogeneity in the current-perpendicular-to-plane (CPP) transport path. Moreover, this phenomenon displays remarkable thermal stability and progressively enhances with rising temperatures.

The second approach involves the use of chiral organic molecules, allowing us to exploit the so-called "chirality-induced spin selectivity" (CISS) effect in 1D and 2D systems. However, there are challenges in terms of feasibility, understanding, and reliable control of the phenomenon, especially in 1D and 2D systems, which are topics of much discussion and debate. In this regard, the general consensus is that spin–orbit coupling is an essential element needed to observe the CISS effect, but there is currently a lack of experimental evidence to support this claim. We studied the CISS effect in chiral functionalized 1D systems (carbon nanotubes (CNTs)) to investigate this claim. Additionally, transfer of CISS phenomenon from 1D to 2D materials is an uncharted avenue of research. We explore the CISS effect in 2D chiral graphene films and systematically investigate its properties under different conditions.

Overall, we report new results which are relevant for future magnetic and spintronic devices. We also describe possible avenues of further investigations based on the results in this thesis.

Preface

Some of the research reported in this thesis (Chapters 5, 6, Appendix B) forms part of an international research collaboration, led by Dr. Luis Álvarez de Cienfuegos, Universidad de Granada in Spain, with Dr. S. Pramanik being the lead collaborator at the University of Alberta.

Regarding Chapters 1 and 2, the literature review and manuscript composition are my original work. Section 2.9 of this chapter has been published as a review article as **Seyedamin Firouzeh**, M. A. Hossain, J. M. Cuerva, L. Álvarez de Cienfuegos, S. Pramanik, (2024), "*Chirality-Induced Spin Selectivity in Composite Materials: A Device Perspective*" Accounts of Chemical Research, 20056-20066. Our group, including myself, M. A. Hossain and S. Pramanik, were involved with the concept formation and manuscript composition of magnetoresistance experiments and electrical concepts. Our collaborators, L. Álvarez de Cienfuegos and J. M. Cuerva from Universidad de Granada in Spain, were involved with the manuscript composition addressing the chemical synthesis aspects of the article.

Regarding Chapters 3 and 4 (VSe_2 MR Devices), the nanofabrication of devices, sample characterization, data collection, data analysis, and manuscript composition are my original work. Parts of Chapters 3 and 4 of this thesis have been published as **Seyedamin Firouzeh,** M. W. Rahman, S. Pramanik, (2022), "*Thermally-driven large current-perpendicular-to-plane magnetoresistance in ultrathin flakes of vanadium diselenide*" Journal of Physics: Condensed Matter, 34(49), 495802. M. W. Rahman assisted with substrate cleaning at the pre-nanofabrication stage. S. Pramanik was the supervisory author and was involved with concept formation and manuscript composition.

Chapter 5 of this thesis has been published as **Seyedamin Firouzeh**, S. Illescas-Lopez, M. A. Hossain, J. M. Cuerva, L. Álvarez de Cienfuegos, S. Pramanik, (2023), "*Chirality-induced spin selectivity in functionalized carbon nanotube networks: The role of spin–orbit coupling*" The Journal of Chemical Physics, 159(3). Nanofabrication of devices, sample characterization, data collection, data analysis, and manuscript composition are my original work. M. A. Hossain assisted with substrate cleaning at the pre-nanofabrication stage. S. Pramanik was the supervisory author and was involved with concept formation and manuscript composition. L. Álvarez de Cienfuegos and J. M. Cuerva were involved with sample functionalization, CD measurements, and manuscript composition addressing the chemical synthesis concepts of the article.

Chapter 6 of this thesis has been published as **Seyedamin Firouzeh**, S. Illescas-Lopez, M. A. Hossain, J. M. Cuerva, L. Álvarez de Cienfuegos, S. Pramanik, (2023), "*Chirality-Induced Spin Selectivity in Supramolecular Chirally Functionalized Graphene*" ACS nano, 17(20), 20424-20433. Nanofabrication of devices, sample characterization, data collection, data analysis, and manuscript composition are my original work. M. A. Hossain assisted with substrate cleaning at the pre-nanofabrication stage and metal deposition. S. Pramanik was the supervisory author and was involved with concept formation and manuscript composition. L. Álvarez de Cienfuegos and J. M. Cuerva were involved with sample functionalization, CD measurements, and manuscript composition addressing the chemical synthesis concepts of articles.

Dedication

To my beloved wife, Fatemeh, for your unwavering support, love, and patience throughout this journey. Your encouragement has been my greatest source of strength.

To my mother, for your endless love, sacrifices, and belief in my dreams. Your wisdom and guidance have been my constant inspiration.

Acknowledgments

I would like to express my deepest gratitude to all those who have supported and guided me throughout my PhD journey.

First and foremost, I want to express my heartfelt gratitude to my wife for her steadfast support, love, and patience.

I am profoundly thankful to my mother for her unconditional love, sacrifices, and faith in my aspirations.

I owe a profound debt of gratitude to my supervisor, Dr. S. Pramanik, for your invaluable mentorship, insightful guidance, and unwavering support. Your dedication and expertise have been instrumental in shaping this work and in my development as a researcher.

I would also like to extend my sincere thanks to the members of my supervisory committee, Dr. Manisha Gupta, and Dr. Xihua Wang, for their constructive feedback, guidance, and encouragement throughout the course of my research.

A special thank you goes to the nanofabrication staff, whose expertise and assistance have been crucial to the successful completion of my experimental work.

Finally, I would like to acknowledge all my colleagues and friends who have provided support, encouragement, and companionship throughout this journey. Your camaraderie has made this experience truly enriching and memorable.

Thank you all for your invaluable contributions to this thesis and to my academic journey.

Table of contents

Table of Figures

Chapter 1: Thesis Objectives

Spintronics, a field combining electronics and magnetism, relies on ferromagnetic materials like iron (Fe) and nickel (Ni). These materials remain magnetic even after the removal of an external magnetic field because their magnetic domains stay aligned due to strong internal interactions. This property characterizes them as ferromagnetic materials. Notable device applications are giant magnetoresistance (GMR) and tunnel magnetoresistance (TMR) devices, which consist of stacks of ferromagnetic and non-ferromagnetic materials. A common geometry is the current-perpendicular-to-plane (CPP) geometry, in which device current flows normal to the planar surface [1].

However, traditional ferromagnetic materials face significant challenges at the nanoscale. At reduced sizes, thermal energy can equal or surpass the energy needed to maintain the magnetic alignment of the domains. As a result, thermal fluctuations can randomize the net magnetization of the domains, causing them to lose their magnetic alignment and related properties once the external magnetic field is removed. This property leads to one of the main challenges for spintronic devices in the nanoscale domain at room temperature. [2].

To address these challenges, we explore two potential solutions, defining Project 1 and Project 2, as shown in Figure 1.1. The former involves replacing traditional ferromagnetic materials with suitable 2D materials and measuring their magnetic behavior in CPP geometry at room temperature (Chapters 3 and 4). The latter explores utilizing the chirality-induced spin selectivity (CISS) effect and employing chiral composite compounds in 1D and 2D systems to create ferromagnet-free spintronic devices (Chapters 5, 6, and the appendix).

In the context of the first project, the goal is to identify 2D materials that could maintain magnetism at the nanoscale and/or exhibit strong magnetoresistance properties especially at high temperature. One possible choice is two-dimensional (2D) magnetic materials like chromium germanium telluride ($Cr_2Ge_2Te_6$) or iron germanium telluride (Fe_3GeTe_2) [3, 4]. These materials can exhibit significant magnetic properties, but only at very low temperatures (below 100K), which limits their practical device applications. Another option is transition metal dichalcogenides (TMDs).

Unfortunately, while explored members of TMDs can show large magnetoresistance properties under strong magnetic fields, they fail to maintain these properties at higher temperatures [5, 6]. Additionally, they are not inherently ferromagnetic as explained in Chapter 2.

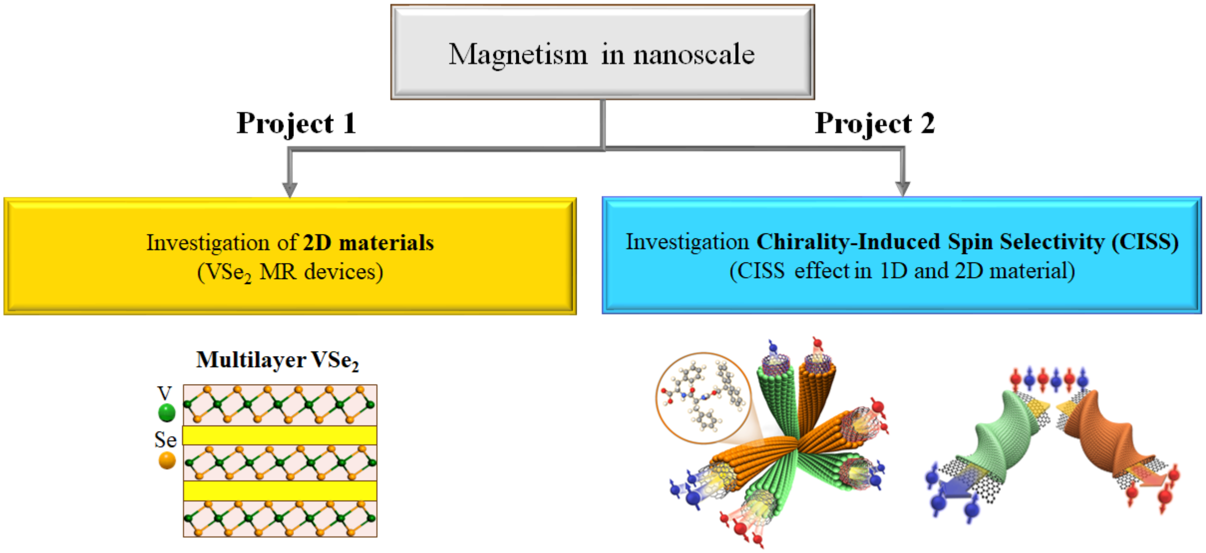

Figure 1.1: Schematic showing the components of this thesis.

As elaborated in Chapter 2, recent studies have highlighted vanadium diselenide (VSe_2), a member of the TMD family, as a potential monolayer ferromagnet [7]. Despite ongoing debates and controversies regarding the origin and nature of ferromagnetism in VSe_2, its metallic form presents several advantages. These include resilience to oxidation for an acceptable period and unique charge density wave (CDW) properties, both explained in detail in Chapters 2 and 4. These attributes make VSe_2 a compelling material for exploring its magnetoresistance properties.

In addition, most research on this topic has been performed in the current-in-plane (CIP) geometry, presumably due to the ease of device nanofabrication. However, the current-perpendicular-to-plane (CPP) geometry could show significant magnetoresistance properties, similar to the GMR/TMR devices [1]. This geometry is often avoided due to fabrication difficulties and issues like pinholes and short circuits. To overcome these challenges and explore VSe_2 in CPP geometry, we established a reproducible three-step nanofabrication process that allows us to sandwich VSe_2 flakes of varying thicknesses between metallic contacts while avoiding pinholes and short circuits. This methodology, detailed in Chapters 3 and 4, enables a more accurate assessment of VSe_2's magnetoresistance properties in a CPP configuration.

In the context of the second project, we explore the chirality-induced spin selectivity (CISS) effect in chiral molecules and their composite materials. The CISS effect could eliminate the dependency of spintronic devices on ferromagnetic materials and address their scaling problems, as explained in Chapter 2. Due to CISS effect, chiral molecules can act as spin filters and induce highly spin-polarized currents at the atomic scale [8]. However, pure chiral molecules are insulators and carry low current as explained in Chapter 2. This limitation motivates us to explore the CISS effect in better conductive materials that can accept the chiral structure of molecules and form supramolecular chiral nanostructures, as described in Chapters 5 and 6.

As clarified in Chapter 2, the origin of the CISS effect, particularly in hybrid chiral nanostructures, remains under research and debate. The general consensus is that the spin-orbit coupling (SOC) of the chiral medium plays a critical role [9, 10], as explained in Chapters 2 and 5. However, experimental evidence is lacking. In Chapter 5, we address this key point by using functionalized carbon nanotubes (CNTs) and adjusting their SOC by manipulating the diameter of the CNTs. This chapter sheds light on how the strength of the SOC affects the CISS effect.

After demonstrating the role of SOC, we attempted to transfer the CISS effect from a 1D system to a 2D system by using graphene instead of CNTs. We investigated CISS in the 2D system using a self-assembly based functionalization method, as explained in Chapter 6 and the appendix. We aimed to elucidate the reasons for the presence of the CISS effect in 2D systems and gain a deeper understanding of CISS in this hybrid system, as detailed in Chapter 6 and the appendix.

In conclusion, the integration of electronics and magnetism in spintronics heavily relies on ferromagnetic materials, which face some formidable challenges at the nanoscale. Addressing some of these issues, in this thesis we proposed two projects: one aiming to identify 2D materials that exhibit high-temperature magnetoresistance properties, and the other exploring the chirality-induced spin selectivity effect in better-conductive media (chiral hybrid nanostructures). Overall, our research, detailed across chapters, contributes to the field of spintronics by exploring innovative materials and emerging phenomena. In the next chapter, a comprehensive overview and general background of Project 1 and Project 2 are elucidated.

Chapter 2: Background

2.1 Introduction

The growth of chip making industry is driven by Moore's law, which is facing drastic challenges in further shrinking the size of transistors to obtain higher computational power [11]. Therefore, researchers are seeking new concepts of electronics that can sustain the growth of computing power. One such promising concept is to use the spin of electrons instead of its charge, an area which is known as "spintronics" [12]. By harnessing spin, computations can in principle be done without generating heat, potentially leading to energy-efficient quantum computing technologies [13]. Spin-based concepts can also lead to ultra-high capacity hard drives[14] and magnetic and biological sensors [15]. However, the operation of spintronic devices relies on magnetic materials, which are difficult to miniaturize, because they tend to lose their magnetic properties below a certain length scale. In a macroscopic piece of magnetic material (like iron), the magnetic moments of the domains are aligned in the same direction, resulting in a strong, noticeable magnetic effect. However, when magnetic materials are reduced to nanoscale dimensions, the total magnetic moment of the material may become sensitive to thermal fluctuations. As the size of the magnetic domains decreases, the thermal energy becomes comparable to or even greater than the energy required to maintain the magnetic alignment. Consequently, the magnetic moments of these nanoparticles become highly unstable, fluctuating randomly with temperature changes [16], resulting in superparamagnetism, which exhibits no hysteresis in the magnetic response [17]. In superparamagnetic materials when an external magnetic field is applied, the magnetic moments of the nanoparticles align with the field, giving the material an apparent magnetization. By removing the external magnetic field, the thermal fluctuations cause the randomization of magnetic moments which leads to loss of the net magnetization [18]. Therefore, there is a need to explore alternative materials and physical concepts that can potentially eliminate the need of traditional magnetic materials in spintronic devices.

Two-dimensional (2D) materials have become increasingly important in the field of nanomagnetism and spintronics due to their unique electronic, optical, and magnetic properties [4]. These flexible materials are composed of a single layer, or a few layers of atoms arranged in a two-dimensional lattice structure. Magnetic devices based on 2D materials could have smaller footprints and consume less power compared to their traditional counterparts [19]. Therefore, research in "two-dimensional" (2D) magnetic materials has recently attracted significant worldwide attention. Most of the contemporary 2D magnetic materials, however, require cooling down to cryogenic temperature to show large magnetic effects [20]. On the other hand, there has been significant activity in the area of “chirality-induced spin selectivity” or CISS, in which chirality of a medium can polarize spins [10]. In the case of organic molecules, it can occur even at room temperature [8]. Chirality can be transferred from chiral molecules to various achiral inorganic materials via chemical functionalization, which can induce the CISS effect in the inorganic materials [21]. This could offer a promising way of generating spins without using ferromagnets. Therefore, in this dissertation, we will investigate two lines of research: (a) magnetotransport phenomena in emerging 2D magnets such as VSe_2 (Chapter 3-4) and (b) CISS effect in 1D (Chapter 5) and 2D (Chapters 6 and Appendix B) materials such as carbon nanotubes and graphene respectively.

2.2 Spintronics

Spintronics, or "spin-based electronics," is a cutting-edge field of physics and electronics that aims to exploit the spin of electrons in addition to their charge for processing and storing information [22]. Unlike conventional electronics that rely solely on the charge of electrons, spintronics utilizes both the charge and the spin of electrons, which opens exciting possibilities for next-generation electronic devices. Spin-based phenomena, such as giant magnetoresistance (GMR) and tunneling magnetoresistance (TMR), have enabled the development of advanced magnetic storage technologies like magnetic hard drives and magnetic random-access memory (MRAM) [23].

Historically, the concept of spin-polarized current was introduced in 1988 with the discovery of GMR in (001) Fe/ (001) Cr multilayers [24]. This groundbreaking discovery revolutionized the data storage industry in the subsequent decades. The discovery of GMR by P. Grünberg and A. Fert was awarded the Nobel prize in physics in 2007 [25]. GMR is a quantum effect observed in magnetic multilayers, where adjacent ferromagnetic thin films are separated by nonmagnetic thin films. The relative magnetic orientations in the ferromagnetic layers strongly influence the electrical resistance due to spin-dependent charge transport in them. In general, a parallel orientation between the ferromagnetic layers corresponds to lower electrical resistance, while an antiparallel orientation gives higher resistance [26]. Ferromagnetic transition metals such as iron and nickel, which show strong ferromagnetism and high compatibility with existing technologies, have been extensively used over the past decade to study GMR and related devices. The GMR ratio can be defined as $\frac{\Delta \mathrm{R}}{R} = \frac{\mathrm{R}\uparrow\downarrow - \mathrm{R}\uparrow\uparrow}{\mathrm{R}\uparrow\uparrow}$; where, $\mathrm{R}\uparrow\uparrow$ and $\mathrm{R}\uparrow\downarrow$ are the resistivity for parallel and antiparallel orientation, respectively [23].

The discovery of GMR led to a family of spintronic devices that rely on spin-dependent charge transport. These include TMR (or magnetic tunnel junction (MTJ)) devices [27], spin valves [28], spin field effect transistors [29], etc. All these spintronic devices heavily rely on magnetic materials such as Ni and Co since they act as reservoirs of spin polarized electrons. As discussed before, these ferromagnetic materials are difficult to miniaturize, due to the fact that they lose their magnetic properties below a certain length scale. The emerging area of two-dimensional van der Waals (vdW) materials (e.g. graphene, boron nitride, and transition metal dichalcogenides (TMDs) [30, 31]) with sub-nanometer single-layer thickness can be highly relevant for miniaturizing spintronic devices. Some of these vdW materials behave as 2D magnets, while the others are non-magnetic. Thus, in principle, a properly created heterojunction of these 2D layers can act as GMR devices.

2.3 Graphene and Transition metal dichalcogenides (TMDs)

Graphene is considered to be the first 2D material in which carbon atoms are arranged in a planar hexagonal lattice. Graphene, a building block of graphite, attracted attention due to its mechanical, electronic and light absorption properties [32]. In 2004, graphene was isolated from graphite by using mechanical exfoliation technique. It was shown that the obtained monocrystalline graphitic films are stable under ambient conditions. They are metallic and they have remarkably high quality [33, 34]. Later, Andre Geim and Konstantin Noveselov were awarded the 2010 Nobel Prize in Physics for isolating monolayer graphene sheets. Similar mechanical exfoliation approach can be used for isolating other 2D layers from layered vdW crystals [35].

The family of transition metal dichalcogenides (TMDs) has been explored extensively in the recent past. These materials have a chemical formula MX_2, where M represents transition metal elements such as Ti, V, Ta, and W, and X represents chalcogen elements such as S, Se and Te. This group of materials is formed by van der Wals (vdW) forces stacking and holding together the atomic layers. Therefore, these materials can be easily peeled off in single layers as in graphene. In each individual layer, there are three atomic planes in an X-M-X configuration, whereby a single plane of transition metal atoms (M) is sandwiched between two planes of chalcogen atoms (X). The particular combination of transition metal and chalcogen elements brings about the extremely diverse range of properties in these materials that can be classified as semiconductors (e.g., MoS_2, WS_2), semimetals (e.g., WTe_2, $TiSe_2$), metals (e.g., NbS_2, VSe_2), and superconductors (e.g., $NbSe_2$, TaS_2) [36-39]. Many of these properties also differ depending on the structural polytypes of one particular compound.

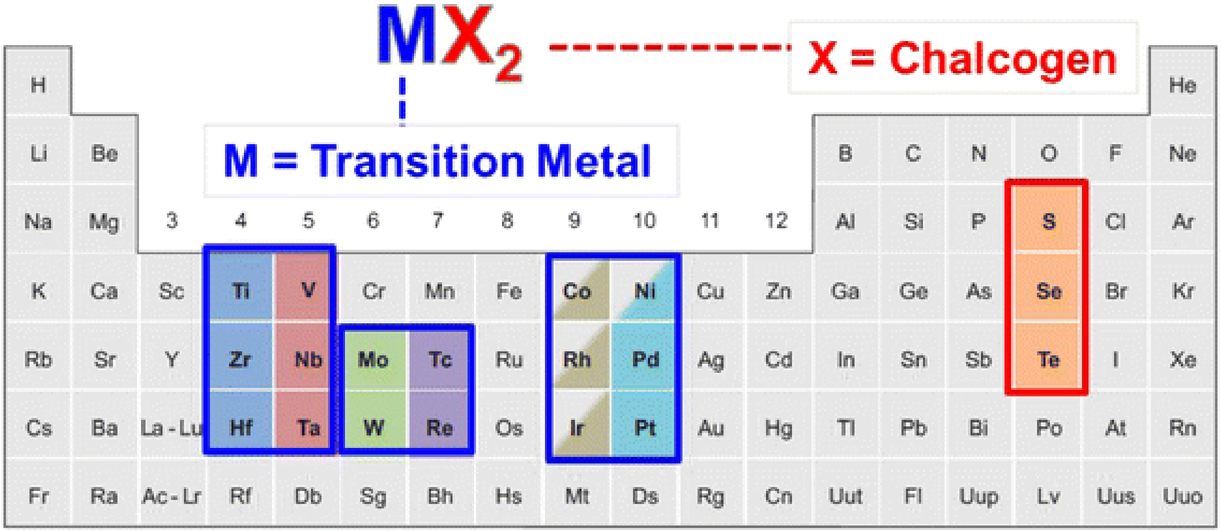

Figure 2.1: Periodic table showing transition metal and chalcogen atoms. There exists a large number of TMD materials, consisting of various combinations of 16 transition metals and three chalcogen atoms [40].

There are two main ways of arranging the layers of 2D materials in a crystal lattice structure: 1T and 2H. These stacking arrangements have different symmetries and result in distinct electronic and optical properties. For instance, 2H-MoS_2 is semiconducting, whereas 1T-MoS_2 is metallic [41]. Although TMDs and their bulk properties have been investigated and documented since the late 1950s, their monolayer or few-layer forms have been available only recently. The reduced geometry is expected to have a profound effect on the performance of fundamental particles and quasi-particles (e.g., electrons, phonons, excitons) due to quantum confinement effects [42]. Therefore, in these nanostructures the electronic transitions the density of states, and strength of interactions are different compared to the bulk. For example, 2H molybdenum disulphide (MoS_2), which normally exists as a semiconductor with an indirect band gap in the bulk, becomes a direct band gap semiconductor in the monolayer form [43]. In addition, these properties were demonstrated to change progressively with decreasing thickness as the material goes from 3D to the 2D limit [44]. Hence, they are excellent candidates for a variety of applications due to this tunable nature [45]. Moreover, by stacking individual layers of different 2D materials, such as graphene, TMDs and hexagonal boron nitride (h-BN), new devices can be studied [46, 47]. Even though the emerging field of 2D materials refocused the researchers' attention on TMDs, still there are important questions surrounding the bulk properties of TMDs, which are still being investigated [48].

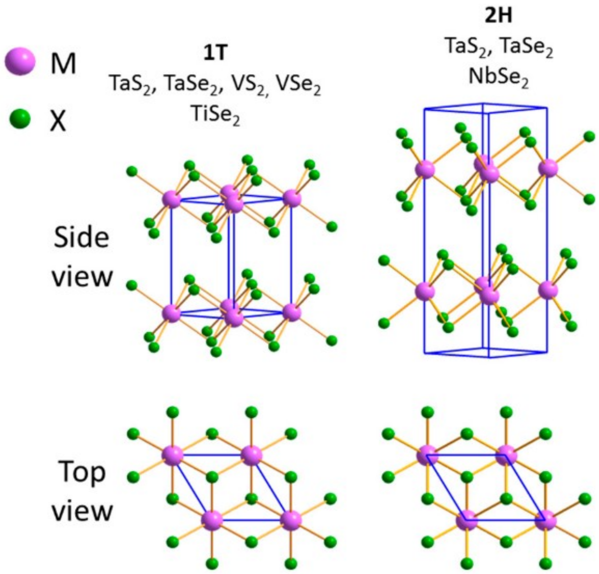

Figure 2.2: Schematics of structural polytypes of 2D TMD materials: 1T (tetragonal symmetry) and 2H (hexagonal symmetry) [49].

As mentioned above, TMDs exhibit numerous structural polytypes [50], the common ones being 1T and 2H, where the letters represent trigonal and hexagonal symmetry of the unit cells, respectively, and the numbers denote the layers included in the unit cell [51]. In Figure 2.2, the crystal structures of the two most stable polytypes are demonstrated. The 1T compounds typically have the vertical lattice distance of $6-7$Å. The 2H polytypes normally have approximately double vertical lattice length, in the range of 12 - 14 Å.

2.4 Charge density waves (CDWs)

In many materials with highly anisotropic crystal and electronic structures, formation of a new ground state may occur at sufficiently low temperatures. This ground state is characterized by a periodic lattice distortion, accompanied by a periodic modulation of the charge density, which is known as the charge density wave (CDW) [52, 53]. As a result of the electronic structure reconstruction, there is an overall minimization of the system energy.

In order to describe the phenomenon of CDW, a clear concept of the electronic structure of solids is required, including several fundamental quantum mechanical theories. A simplified theory is presented here based on the Sommerfeld model of metals. CDW is then introduced in its simplest form as theorised by Rudolf Peierls in 1955 for the case of a one-dimensional (1D) linear metallic chain [54].

2.4.1 Sommerfeld model

In 1920, Sommerfeld applied the Pauli exclusion principle to the free electron gas of metals and resolved the thermal anomalies of the early Drude model. The offered model is a quantum mechanical theory capable of explaining many of the observed electronic properties of metals [55, 56]. The quantisation of electronic energy states within a solid is the result of quantum mechanics, allowing the presence of only a certain number of states per unit volume of phase space. In the Sommerfeld model, electrons are treated as nearly-free particles moving in a periodic potential created by the crystal lattice. The main assumption is that the periodic crystal potential is weak and can be treated as a perturbation to the behavior of free electrons. The model assumes that the electrons move independently, as if they were free particles with no electron-ion or electron-electron interactions. This assumption simplifies the calculations and allows for a tractable theoretical description of the electron behavior. While the Sommerfeld model provides a more accurate and sophisticated description of electron behavior in metals than the classical Drude model, it still does not explicitly involve the concept of charge wave density, which is a more detailed aspect of quantum mechanical behavior in crystalline solids.

2.4.2 Peierls transition

Peierls explained CDW formation in a simple one-dimensional system, based on energy considerations related to the electronic structure [32]. Assume a one-dimensional linear metallic chain, as depicted in Figure 2.3, at zero temperature. Without any particle interaction, the ground state is defined by electrons filled up to the Fermi level E_F. The lattice in this case is arranged in a regular spacing of atoms with separation *a* and uniform charge density. The Fermi level represents the highest energy level that is occupied by electrons at absolute zero temperature. At this temperature, the electronic energy levels in the material are primarily determined by the band structure and the periodic lattice potential. The electrons tend to occupy the lowest energy states to minimize their total energy, $\mathrm{E_{total_a}}$.

As the temperature increases, due to electron-phonon interaction, the system becomes more dynamic, allowing thermally excited electrons to explore a broader range of energy states. At a specific critical temperature, in some materials the thermal energy may become sufficient to drive a phase transition. The transition occurs when the electronic energy bands are partially filled near the Fermi level, and the strength of the electron-phonon interaction is sufficient to induce lattice instability, known as Peierls instability. In this state, there is a tendency for electrons to lower their energy by pairing with lattice vibrations. This pairing creates a distortion in the periodic lattice and the potential experienced by the electrons. Hence, the atoms in the crystal lattice shift from their original positions to a new configuration. The lattice distortion causes the electronic band structure to split into smaller energy sub-bands. The Fermi level now falls in the middle of an energy sub-band and the system gains the new total energy, $\mathrm{E_{total_b}}$. The electrons are arranged in a way that the lower energy states, created by the band splitting, are more populated. This results in a lower total energy for the system, $\mathrm{E_{total_b}} < \mathrm{E_{total_a}}$. This periodic density modulation is known as" charge density wave" (CDW).

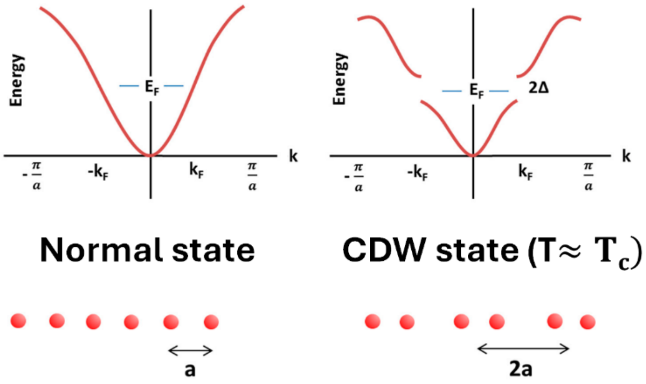

Figure 2.3: Illustration of transition from the normal state to the charge-density-wave state in one dimension. The atomic displacements lead to the formation of a "superlattice" resulting in opening of an electronic energy band gap [49].

The CDW state can be characterized as either commensurate or incommensurate. In a commensurate CDW, the period of the density wave modulation λ_{CDW} is an integer multiple of the period of the underlying distorted lattice, a. This means the CDW density modulation aligns with the periodicity of the lattice distortion, and the CDW is in phase with the underlying lattice. In an incommensurate CDW, the period of the density wave modulation does not match the periodicity of the underlying distorted lattice in a simple integer multiple relationship [57].

2.5 CDW properties of TMDs

It has been shown that TMDs exhibit anomalies in the temperature-dependence of electrical [58-60], magnetic [61] and thermal [62] properties, indicating the presence of phase transitions in them. As discussed above, when a material undergoes a transition to a CDW state, it results in the formation of a superlattice, which is a repeating pattern of charge-rich and charge-poor regions in the crystal lattice. This superlattice formation can be observed in diffraction experiments [63]. In a majority of TMDs, the higher transition temperature belongs to the incommensurate phase and at a lower temperature, by further decreasing the total energy, the electronic order locks into a commensurate geometry. For example, in 2H-$TaSe_2$, a transition occurs at 122K to a CDW which is incommensurate with the underlying lattice. It is followed by lock-in to commensurate CDW at a lower temperature of 90K [64]. 1T-$TiSe_2$ shows the commensurate CDW ($2a_0 \times 2a_0 \times 2c_0$) at 202K and 1T-$VSe_2$ has been reported to possess incommensurate CDW ($4a_0 \times 4a_0 \times 3.18c_0$) at 110K [65].

2.6 Electrical properties of TMDs

In TMDs, the electronic band structure is determined by the interaction of the p-orbitals of the chalcogen atoms and the d-orbitals of the metal atoms, leading to distinct valence (V_B) and conduction (C_B) bands. The Fermi surface, which describes the distribution of electron energy states in momentum space, plays a crucial role in understanding the electronic behavior of these materials. In this context, the Fermi surface of 1T-TMDs exhibits intriguing features characterized by elliptical electron pockets, derived from the metal d-band at the M-point of the Brillouin zone [66]. The nature of these electron pockets varies depending on whether the TMDs are of group-IV or group-V compounds. Specifically, for group-IV TMDs such as Ti, Zr, and Hf, the Fermi surface appears either as small-closed ellipses or larger open ellipses, signifying differences in their electronic behavior [67, 68]. Among the group-IV TMDs, Zr and Hf exhibit properties of small band gap semiconductors, while Ti TMDs display characteristics of semimetals. In contrast, group-V TMDs, such as V, Nb, and Ta TMDs, exhibit a fundamentally different electronic nature, with no band gap, and the lowest energy conduction band unequivocally crosses the Fermi level [67, 68]. The interplay between metal and chalcogen orbitals results in diverse electronic behaviors, ranging from semiconducting to semimetallic properties. Understanding these electronic features is crucial for harnessing the potential of TMDs in designing next-generation electronic devices with enhanced functionality and performance.

2.7 Magnetoresistance phenomena in TMDs

Magnetoresistance (MR) effects in TMDs have been studied extensively in recent years with different device geometries and under various orientations of applied external magnetic field. The layer thickness, stacking order and defects can significantly influence the MR effects [5, 69-71]. The prominent magnetoresistance effects observed in TMDs are: (a) weak localization and weak antilocalization [6, 72] and (b) linear MR [5, 37]. A brief overview of these effects is provided below, and detailed description of these effects is available in the cited references.

2.7.1 Weak localization and weak antilocalization

The wave nature of an electron in a material can typically be detected by quantum interference effects at low temperatures [73]. Weak localization (WL) is such a quantum interference effect that occurs in mildly impure conductive materials and results in a negative MR. In the presence of impurities, defects, or disorder in the crystal lattice of a material, the motion of electrons can be significantly affected. When electrons move through the material, they can scatter off these imperfections, causing them to change direction and path multiple times. There is a finite probability for the conduction electrons to diffuse in a closed loop, through multiple scattering centers and reach the starting point or the origin [74]. These partial waves returning to the origin result in constructive interference. This constructive interference increases electron’s tendency (or, probability) to remain at the origin, leading to a localization effect, and this causes a slight decrease in intrinsic conductivity of the material at low temperatures. This phenomenon is known as “weak localization”. By applying an external magnetic field, it affects the phase of the electron wavefunctions in the closed loops. This phase change alters the interference pattern and leads to destructive interference, effectively reducing the above localization effect of the electrons [74]. As a result, the conductivity increases with magnetic field, and the material exhibits negative MR [6]. This negative MR due to weak localization effect is generally observed at low temperatures where the wave nature of the electron is preserved because of the absence of phase-breaking scattering events (such as phonons).

On the other hand, the presence of spin-orbit interaction in some material can lead to an intriguing effect known as weak antilocalization (WAL). Spin-orbit coupling is an interaction between the electron's spin and its motion due to the presence of electric fields from the atomic nuclei. In the presence of strong spin-orbit coupling the electronic energy bands split into spin-split bands. The electrons with different spin orientations experience slightly different scattering potentials. These spin-dependent scattering events alter the phase coherence between different quantum paths. Quantum paths with different phases can interfere destructively, leading to the suppression of backscattering and the emergence of weak antilocalization [75]. Applying an external magnetic field results in the reduction of destructive interferences that are responsible for the WAL phenomenon. This suppression enhances the localization effect via increased backscattering, which leads to an increase in electrical resistance in the presence of a magnetic field. Therefore, a positive magnetoresistance emerges as a result of the applied magnetic field in such materials [76].

2.7.2 Linear MR

A theory of linear MR has been given by Parish and Littlewood to explain the appearance of large, non-saturating positive MR effect in some materials [77]. This theory is mainly based on the inhomogeneity of the material, which was modeled as a random array of resistive disks. For magnetic field applied perpendicular to the plane, Lorentz force causes charge carriers to rotate in circular trajectories (cyclotron orbits) in each individual disk. This induces a transverse voltage called Hall voltage in the direction perpendicular to both magnetic field and bias direction. Since Hall voltage increases linearly with magnetic field, the resultant MR in the bias direction also exhibits a linear response. However, Hall voltage alone cannot completely describe this large, non-saturating MR effect. As mentioned above, in this model, the inhomogeneity of materials has been modeled as the random arrangement of resistive disks. In materials with inherent randomness, multiple current paths can be generated, dispersing in various directions and regions of the material. This randomness leads to variations in the mobility of charge carriers across the crystal structure. Consequently, certain regions of the material exhibit higher mobility, enabling charge carriers to move more freely, while other regions impede their motion with lower mobility. In materials with inhomogeneous mobility, regions with higher mobility contribute less to the overall electrical resistance compared to regions with lower mobility.

When an external magnetic field is applied, charge carriers in the regions with higher mobility experience less scattering, resulting in smaller contributions to the magnetoresistance (MR). Conversely, charge carriers in regions with lower mobility encounter stronger scattering, leading to larger MR contributions. Considering all regions of the material, ref. [77] showed that the application of an external magnetic field amplifies the mobility difference between these regions, and induces positive magnetoresistance. This phenomenon is characterized by a non-saturating increase in electrical resistance with the magnetic field strength.

2.8 Recent studies on vanadium diselenide (VSe_2) and its magnetic properties

Recent interest in VSe_2 is due to the theoretical calculations predicting ferromagnetism in monolayer 2H-VSe_2 [78-82]. This is surprising, because bulk VSe_2 is paramagnetic, and no ferromagnetism is expected in most 2D materials. In addition, experimentally, VSe_2 consistently exhibits the 1T structure and no reproducible evidence of 2H-VSe_2 has been found in bulk or thin layer forms. Most of the experimental works on VSe_2 have been on the bulk form. Bulk VSe_2 is metallic (due to half-filled V-3d band) with a 1T structure. The vanadium metal atom is octahedrally configurated with respect to the selenium atoms. The lattice constants are $a = b = 0.335$ nm and $c = 0.610$ nm. As mentioned earlier, 1T-VSe_2 demonstrates a CDW transition at 110K [83]. Several techniques have been used for the synthesis of thin VSe_2 flakes such as mechanical exfoliation [84], liquid exfoliation [85, 86], chemical vapor deposition (CVD) [87], and molecular beam epitaxy [88].

Bonilla, Xu and Yu et. al. [7, 86] reported strong room temperature ferromagnetism in mono- and ultrathin layers of 1T VSe_2. Although the origin of the observed ferromagnetism is still under debate [6, 89-93], initial studies have indicated that VSe_2 is relatively air-stable [94], with potentially high Curie temperature of monolayers, which make it a promising exploratory candidate for 2D magnetic devices. Being a CDW material, ground state of monolayer VSe_2 exhibits an intriguing competition between ferromagnetic order and the CDW order [7, 95].

Current-perpendicular-to-plane (CPP) charge transport and MR effects in VSe_2 multilayers has attracted significant theoretical attention in recent years [96-99]. This is motivated by the fact that bilayer VSe_2 in 2H (trigonal prismatic) phase is an antiferromagnetic vdW crystal i.e. magnetic V atoms are coupled ferromagnetically within the plane, whereas the adjacent atomic planes are coupled antiferromagnetically. This is reminiscent of GMR devices, where an external magnetic field can be used to align the layer magnetizations from antiparallel to parallel, leading to a large MR effect due to spin-dependent transmission. Gong et. Al. [96] showed theoretically that an out-of-plane electric field can potentially induce half-metallicity in 2H-VSe_2 bilayers, which could lead to ∼100% spin-polarized CPP current. Yang et. al. [99] and Zhou et. al. [94] modelled vdW magnetic tunnel junction devices with 1T-VSe_2 as the ferromagnetic layer. However, no experimental work has been reported so far in this area, motivating our work in this direction, described in Chapter 3 and Chapter 4 of this thesis.

2.9 Chirality-induced spin selectivity (CISS)*

Chirality-induced spin selectivity (CISS) is a phenomenon generally observed in chiral organic molecules and molecular assemblies [100, 101]. Chiral molecules possess an asymmetrical spatial arrangement of atoms, making them non-superimposable mirror images of each other. In the context of CISS, this property leads to spin unpolarized carriers, acquiring a chirality-dependent spin polarization after transmission through a chiral medium (Figure 2.4(a)) [100, 101]. In other words, left- and right-handed chiral media may preferentially transmit "spin up" and "spin down" electrons, respectively. Therefore, due to CISS effect, the chiral media may act as a magnet-free spin filter or injector/detector, thus avoiding the scaling challenges of magnetic materials discussed before, and offering a way to realize these spintronic operations at the molecular scale [101]. This effect has profound implications in condensed matter, device physics and spintronics, as well as in chiral electrocatalysis and enantiomer separation [100, 101].

Historically, CISS has been observed in photoemission experiments, in which spin-unpolarized electrons emitted from a Au substrate acquire significant spin polarization after passing through a chiral ds-DNA layer, as shown in Figure 2.4 (b) [10]. CISS has also been reported in device setups, in which a ds-DNA molecule was contacted by a Au particle and a ferromagnetic spin detector (Ni) [100]. Spin-unpolarized electrons passing through Au become spin-polarized after transmission through the ds-DNA molecule. Depending on Ni magnetization orientation (±M), two different current values (I(±M)) are obtained (Figure 2.4(e)), indicating a net spin polarization of the incoming electrons. CISS magnetoresistance (MR) can be defined as ((I(+M) - I(-M))) ⁄ ((I(+M) + I(-M))), which is often described as “spin polarization” or “spin selectivity” in the literature [100]. This quantity changes sign for the opposite chirality [100].

---

* Part of this section has been published in our review ACR paper [21].

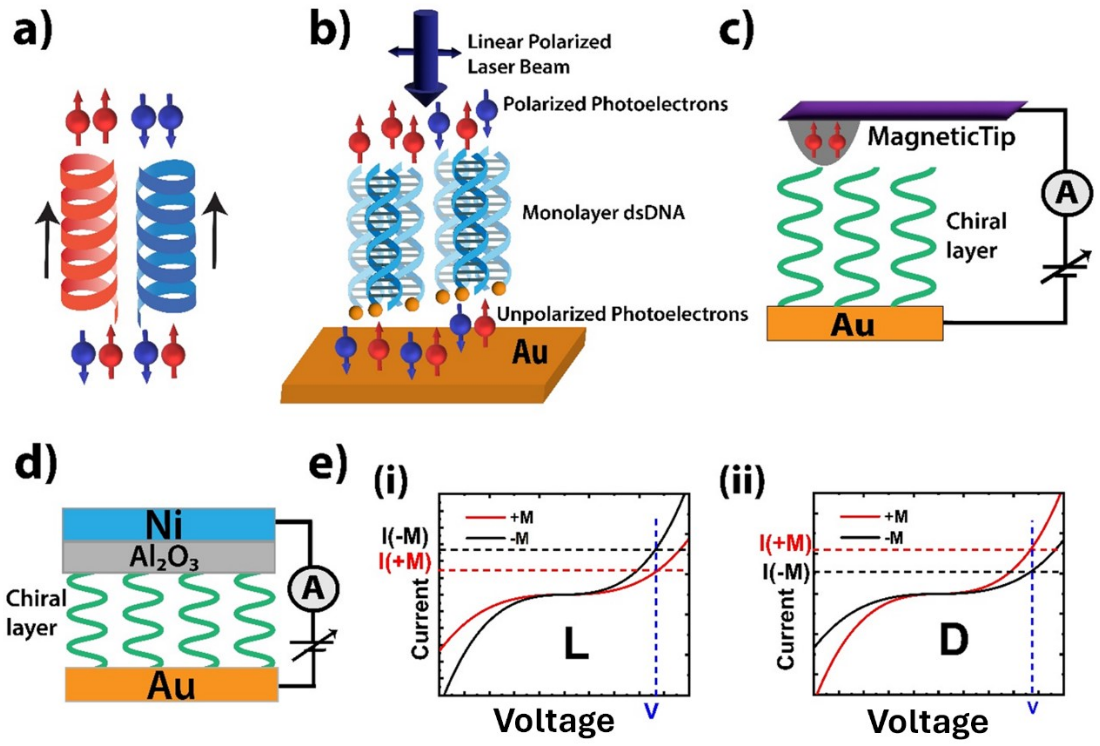

Figure 2.4: **(a)** Schematic description of the CISS effect. Transmission of spin-unpolarized electrons through a chiral medium result in a chirality-dependent spin polarization, with spins polarized parallel or antiparallel to the velocity (indicated by arrow). **(b)** Detection of the CISS effect in a photoemission setup (*adapted from [10]*). Spin unpolarized photoelectrons, emitted from the Au substrate by linear polarized light, acquire spin polarization after passing through a chiral dsDNA layer adsorbed on the surface. **(c)** CISS measurement geometry using Au film and a magnetic AFM tip, probing few chiral molecules. (**d**) CISS measurement geometry using a vertical sandwich structure, probing a large ensemble of chiral molecules. **(e)** Chirality-dependent current asymmetry ($\boldsymbol{I}_{\pm \boldsymbol{M}}$) observed in two-terminal CISS experiments.

Two device geometries are commonly studied [100]: (a) setups using a magnetic AFM tip (mCP-AFM) (Figure 2.4(c)), probing very few chiral molecules in a nanometer scale domain and (b) setups with a vertical sandwich structure (Figure 2.4(d)), probing a large ensemble of molecules. In the former case, device current is highly sensitive to the tip-molecule contact, and to address the spatial and temporal variations, such studies typically measure hundreds of current-voltage scans in each magnetic configuration and compare the average responses. These studies generally report a high degree of spin selectivity, although such configurations are not suitable as practical devices. In the second case, spin selectivity is generally much weaker, presumably due to sample inhomogeneity over a larger area, presence of spin-independent leakage paths via pinhole shorts, as well as poor control on the interface quality.

The simplicity of the two-terminal MR devices described above belies the underlying conceptual complexity. For example: (a) the two terminal MR is expected to be zero in the linear bias range according to Onsager's reciprocity, leading to significant controversy regarding the measured CISS signals [102]; (b) Spin polarization or spin selectivity, as defined above, represents CISS MR, and extraction of carrier spin polarization is not straightforward [103]; (c) While the CISS MR generally appears in a longitudinal geometry with current parallel to the magnetic field, in some systems a transverse CISS MR was observed [104]; (d) Temperature dependence of the MR responses vary significantly depending on the measurement setup (Figures 2.4(c), (d)). For example, the AFM geometry (Figure 2.4(c)) typically shows CISS response at room temperature [105] whereas the vertical sandwich geometry (Figure 2.4(d)) often shows low-temperature response [106, 107] and in some cases show room-temperature response [108].

Despite the above open questions, the two-terminal vertical CISS MR devices discussed above remain quite relevant due to their structural simplicity and resemblance with more established spintronic devices such as spin valves and giant- or tunnel-magnetoresistance devices [109]. However, due to the poor conductivity of common chiral organics (DNA, amino acids etc.), they are not ideal materials for spintronic devices. Also, limited work has been done on planar multiterminal CISS devices, presumably due to the high resistance of these chiral molecules, which make this geometry impractical. Nevertheless, such studies are essential not only for deeper understanding of the CISS effect, but they may also open new device research opportunities [102].

It is therefore clear that alternative chiral materials with improved material properties and electronic conductivity need to be investigated for CISS device applications, and composite chiral materials, which combine high electron mobility of the inorganic materials with the chirality of the organics, can play a crucial role in this regard. In the next section, we will discuss various chiral composites and chirality transfer mechanisms that are essential for the CISS effect. Next, we will discuss the CISS effect in these materials, address recent developments, and highlight our group's contributions in this field.

2.9.1 Chirality in composite materials

Most of the chiral composite materials developed for CISS use enantiopure organic compounds combined with, generally achiral, inorganic, metallic or carbon allotropes.

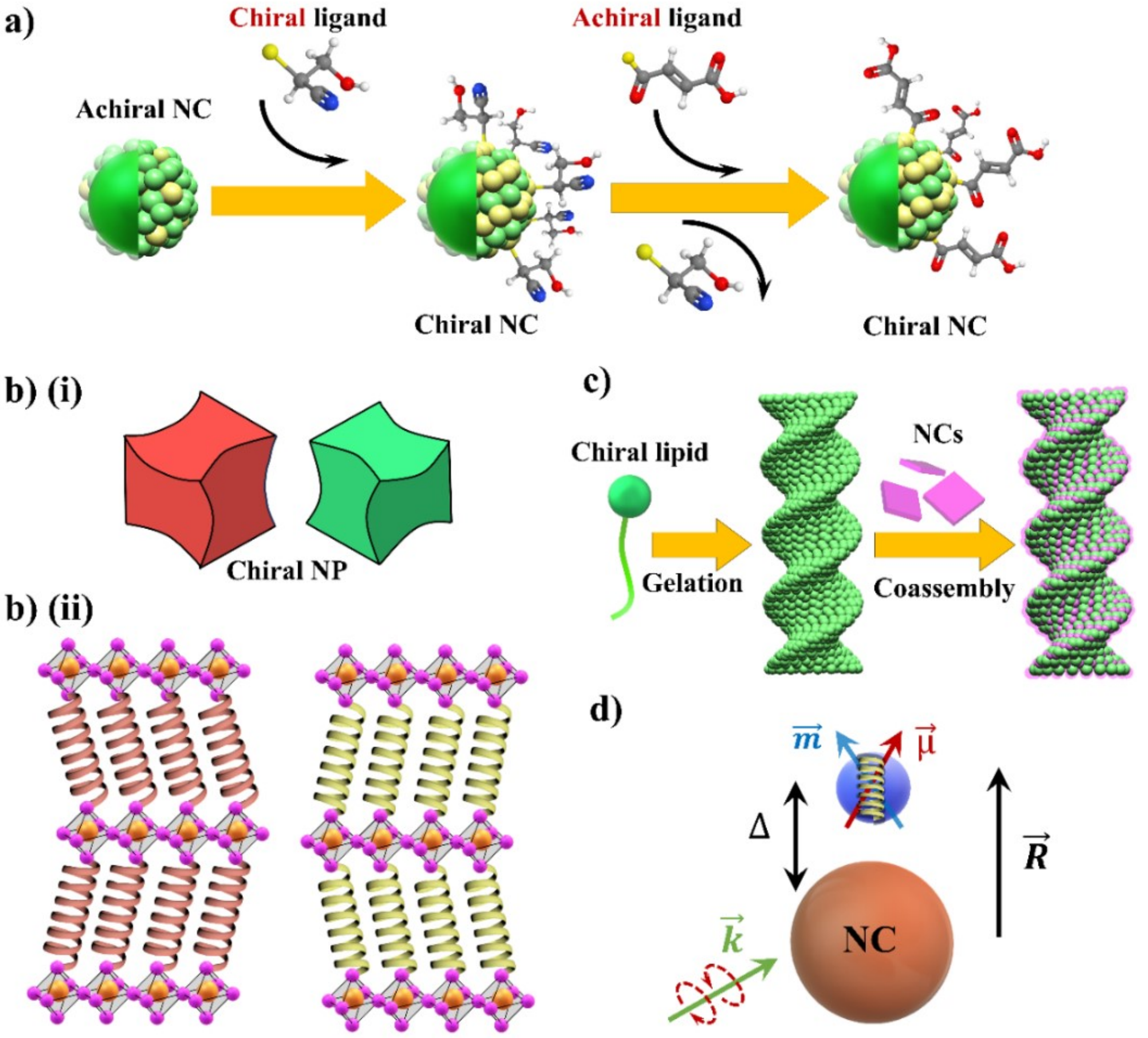

Figure 2.5: Various chiral composite materials and chirality transfer mechanisms. **(a)** Enantioselective surface distortion by chiral molecules (*adapted from [110] Copyright © 2009, American Chemical Society*). The surface of the achiral nanocrystal (NC) can be made chiral by attachment of chiral ligands on the surface. The chirality of the NC surface is indicated by the arrangement of the yellow spheres. In some cases, subsequent replacement of the chiral ligand by an achiral ligand preserves the surface chirality of the nanocrystal as shown in the schematic. This is the so-called "chiral memory effect". **(b) (i)** Schematic of chiral crystals (*adapted from [111] under a CC license*). The original straight edges of the nanoparticles are twisted in opposite directions, depending on the chirality of the molecule. **(b) (ii)** Schematic of 2D hybrid chiral perovskites, with chiral molecules inserted in the inorganic framework. Conceptually similar structures are obtained by intercalating chiral molecules in the interlayer regions of 2D van der Waals materials. **(c)** Schematic of inducing chirality in perovskite nanocrystals via co-assembly in chiral gels (*adapted from [112] with permission from Wiley VCH*). Chiral lipid could form a gel via chiral assembly. If perovskite NCs are added during this process, they can co-assemble and follow the chirality of the gel structure, which induces chirality in the NCs. **(d)** Schematic description of chiral molecule and achiral nanocrystal coupled via Coulombic interactions (*adapted from [113] Copyright © 2010, American Chemical Society*).

Chirality transfer occurs from the organics to the inorganics and this mechanism is critical, as it determines the CISS effect. Four principal chirality transfer mechanisms are discussed below.

1) **Enantioselective surface distortion by chiral molecules**: In this strategy, the surface of inorganic nanocrystals is covered by enantiopure organic ligands. These inorganic nanocrystals (NCs) could be metallic nanoparticles (NPs), such as Au, inorganic nanocrystals (NCs) such as CdX (X = S, Se and Te) and perovskites. This combination modifies the surface via a chemical bond between the chiral ligands and the metallic centers on the surface of the NCs, which causes a transfer of chirality to the crystal surface and related electronic states. This strategy was first reported using Au NPs and sulfur containing L-glutathione [114]. These chiral surface-functionalized Au NPs showed strong chiroptical responses proving that the electronic structure of the metal could be easily tuned by the capping molecules. Later, a similar strategy was explored with Cd based inorganic nanocrystals, prepared by microwave irradiation in the presence of organic chiral ligands such as, L/D-penicillamine and L/D-cysteine methyl ester [110, 115]. Results showed that NC cores were achiral, and the surface was chiral due to the attached chiral organic ligand. In contrast with the chiral Au NPs, the surface of the inorganic particle became permanently chiral, thus rendering these NCs intrinsically chiral even after removing the chiral ligand. This is known as chiral memory effect (Figure 2.5(a)).
2) **Formation of chiral crystals by chiral molecules**: Some inorganic crystals such as quartz, Se, Te, β-AgSe, α-HgS etc. have intrinsic chiral structures [116, 117]. NCs of these materials are expected to show stronger chiroptical properties than those obtained by surface modification since, in this case, the whole particle, and not only the surface, is arranged in a chiral structure. The main drawback is that in the absence of any chiral stimulus, racemic mixtures are obtained [118]. This approach achieves a higher hierarchical level of chirality with respect to the previous approach [111]. In this mechanism enantiopure NCs can be obtained by colloidal precipitation of NCs in the presence of a enantiopure additive during crystal nucleation and growth, inducing the preferred formation of one enantiomorph. For example in reference [111] incubation of achiral Au NPs seeds with L/D amino acids and peptides gave rise to intrinsically chiral particles (Figure 2.5(b) (i)), with their handedness being governed by the chirality of the organic additive. Induction of chirality in bulk Au and Ag via a doping effect was reported in reference [119]. Chiral organic-inorganic crystals have also been obtained by the combination of lead halides and a chiral primary amine (R/S-methylbenzylamine) [120]. These structures arranged in 1D chains and 2D layers in which

the organic molecules are inserted between the inorganic halides (Figure 2.5(b) (ii)) [120]. These 2D layered perovskites exhibit circular dichroism (CD) in which the sign is determined by the chirality of the amine [120].

3) **Supramolecular chirality by self-assembly:** Self-assembly of small molecules into higher order aggregates gives rise to a new type of chirality known as supramolecular chirality. Chirality is a property of the global system and not of the individual component, being sufficient in the absence of a symmetry plane or inversion center. Therefore, chiral supramolecular aggregates can be developed using achiral monomers. In this case, a symmetry breaking event must take place. Solid surfaces can be viewed as such kind of symmetry breaking inductors once 2D chirality is considered. Two different strategies have been mainly studied. In the first strategy, the nanoparticles are formed in an existing chiral network, which acts as a supramolecular template. In the second strategy, a co-assembly process is employed in such a way that the particle is incorporated in the chiral network at the same time this is formed by a process of self-assembly. In both cases, the nanoparticle suffers a chirality transfer process being surrounded and/or covered by a chiral supramolecular network. This strategy has been used to grow Au nanoparticles in helical supramolecular structures and to obtain gold nanorods embedded in chiral fibers [121]. By a similar process of co-assembly, perovskite NCs have been embedded in a chiral network formed by self-assembly (Figure 2.5(c)) [112]. As described in Chapter 5-6 and Appendix B, we have used the strategy of co-assembly to induce chirality in carbon nanotubes (CNTs) and graphene by promoting the self-assembly of enantiopure aromatic short peptides in the presence of these carbon-based materials.
4) **Electronic interactions between chiral and achiral materials:** Beyond surface modifications, chiral molecules can interact through space with NCs via complex dipole and multipole Coulomb interactions (Figure 2.5(d)) without requiring surface or crystal distortions and with the consequent appearing of new CD bands. It has been shown that the NCs induce a change in the electromagnetic field of the chiral molecule and, the chiral molecule also induces a chiral current inside the crystal [113]. The latter mechanism explains the CD signal at plasmon frequency. It is worth noting that this type of interaction can be exerted simultaneously with the previously mentioned ones [122].

2.9.2 CISS in composite materials

Some of the composite chiral materials discussed above exhibit CISS effect in *electronic transport experiments*. Reference [108] studied chiral cysteine capped CdSe quantum dots (~2 nm) using both mCP-AFM geometry as well as vertical thin film sandwich structure, discussed earlier in previous section. The former shows a stronger spin selective response than the latter, as discussed previously. The MR response is found to be opposite compared to self-assembled monolayers of cysteine, which correlates with the sign of the CD signal, indicating that electron conduction is intimately related to the chirality of the system. For larger (~6 nm) quantum dots, the CISS effect is negligible, which again correlates with the decreasing CD response with size. This is presumably because the chirality transfer effect is weakened with increasing quantum dot size. Finally, the CISS MR has been found to be almost independent of temperature. Although the issue of Onsager's reciprocity was not directly addressed in this work, the data seem to indicate the validity of this principle in the linear range.

Organic-inorganic chiral perovskites discussed above are promising candidates for spintronics because of (a) long spin relaxation times, (b) strong spin-orbit coupling (SOC), (c) tunable Rashba splitting and (d) chemically tunable optical, and electrical properties [123]. Lu et al. showed CISS effect in solution-processed polycrystalline 2D chiral organic-inorganic lead iodide perovskite films using mCP-AFM [107]. Spin selectivity, as defined in above section, was found to be ~ 86%. In contrast, in the sandwich geometry, this material showed < 1% MR, only at low temperature (~10 K). While the smaller MR in the sandwich geometry is consistent with the chiral CdSe study discussed above, the temperature dependence of the MR signal is different in these two chiral systems. As shown schematically in Figure 2.5(b) (ii), these chiral hybrid perovskites have a 2D layered structure, in which chiral organic molecules occupy the space between two neighboring inorganic layers and in a typical *vertical* transport setup, the charge carriers travel sequentially from one type of layer to the other. Chirality-dependent spin polarization is accrued during their transport through the chiral layers. The inorganic sublattice confers structural ordering in these samples and adds a second mechanism, multiple chiral tunneling steps, to this hybrid system. Therefore, a large CISS response in all these cases observed [123].

Besides chiral perovskites other organic-inorganic or organic-metallic composites have been developed for spintronics. Huizi-Rayo et al. reported the synthesis of a chiral 3D metal-organic framework (MOF), based on the lanthanide Dy(III) and the L-tartrate chiral ligand [124]. The spin polarization of this material proved to be ideal showing spin selectivity up to 100% at a bias voltage of 2V measured by mCP-AFM.

2D atomic crystals of transition metal dichalcogenides allow the introduction of chiral molecules between the atomic layers without disturbing its crystallinity. Qian et al. studied the CISS properties of 2D atomic crystals of TaS_2 and TiS_2 intercalated with *R*/*S*-methylbenzylamine [125]. Results showed a clear chirality-dependent out-of-plane current, with a spin polarization of more than 60% at 10 K. Reference [126] studied out-of-plane transport in multilayer MoS_2 intercalated with chiral methylbenzylamine molecules. MCP-AFM measurements showed ~75% spin polarization. Similar to the hybrid perovskites discussed above, due to out-of-plane electronic transport, the observed CISS effect arises purely due to the interlayer chiral molecules present in the transport path. While the 2D layers offer structural stability and robustness to the devices, which improves CISS response, their planar electronic and spintronic properties remain largely untapped.

Another strategy is the combination of carbon allotropes with chiral molecules to harvest CISS effect. In this method CNTs and graphene bind non-covalently with various organic molecules via π stacking and electrostatic interactions [127]. Synthesis of CNT-DNA hybrids, in which DNA strands helically wrap CNTs (Figure 2.6(a)), were reported in [128]. Theoretical calculations have shown that such composites can act as spin filters [129]. Electron transport occurs via the CNT channel, and the role of the DNA strands is to induce an inversion-asymmetric, helicoidal electric field on the charge carriers. This electric field produces a strong Rashba spin-orbit interaction in the channel and polarizes the electron spins. In 2015, our research group was the first to experimentally study spin filtering of ssDNA-wrapped single-wall (SW) CNT using $d(GT)_{15}$ strands [130]. A planar device in which ssDNA-wrapped tubes were contacted between Au and Ni (spin detector) electrodes is developed, as shown in Figure 2.6(b). MR measurements showed that this system could act as a spin filter with spin polarization up to ~74% at low temperatures (Figure 2.6(c)). Later, our group showed that higher spin polarizations (~80%) could be achieved by using ssDNA strands made only of thymine $(TT)_{15}$ [131], or, by using longer $d(GT)_{200}$ strands [132].

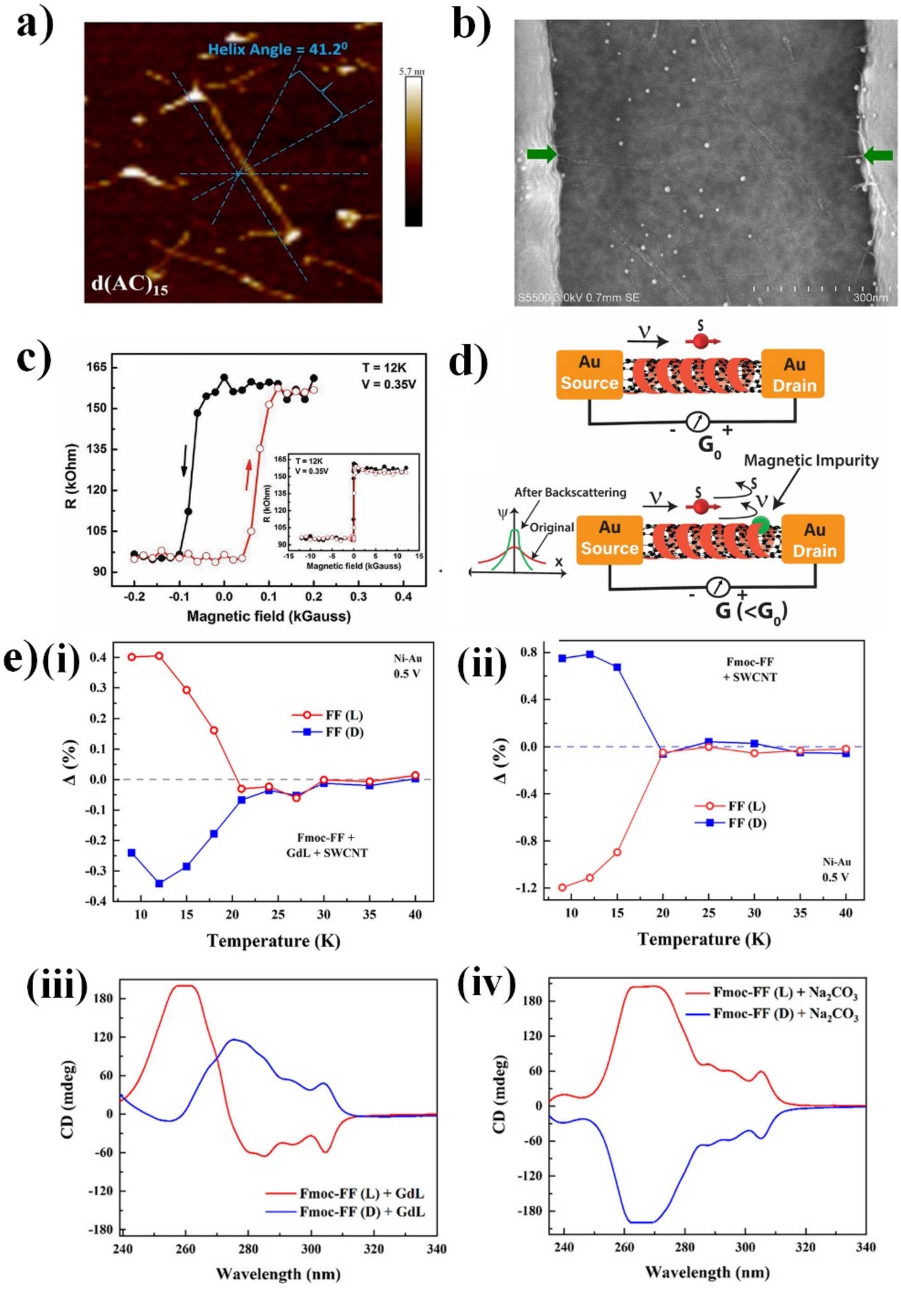

Figure 2.6: CISS effect in chiral organic-CNT/graphene composites. **(a)** Helical wrapping of CNTs by ssDNA (d(AC)15) strands. Periodic height modulation along the CNT axis indicates helical wrapping, and an estimation of the helix angle has been shown (Copyright © 2020, American Chemical Society). **(b)** Device geometry in which a DNA-wrapped CNT is contacted by Ni-Au electrodes. The green arrows indicate the contact points. **(c)** MR behavior of DNA-wrapped CNTs. Two distinct conductance states are observed for two opposite orientations of Ni (spin detector) magnetization, implying spin filtering. (Fig. 1.6b and c reprinted from [133] with permission from Wiley VCH). **(d)** Schematic description of the role of CISS on carrier localization. Backscattering (and hence carrier localization) is possible only when there is a magnetic impurity. **(e)** Role of chiral GDL on CISS. For Fmoc-FF, addition of GDL changes the supramolecular chirality, with a concomitant change in the sign of the CISS signal (Copyright © 2022, American Chemical Society).

These results offered a new way to engineer spin polarization by changing the chemical composition of the DNA, opening the door to explore other chiral compounds of varying chemical compositions. This was confirmed by studying spin polarization of SWCNTs functionalized with $d(AC)_{15}$ and $d(CC)_{15}$ sequences and comparing the results with those measured before, $d(GT)_{15}$ and $d(TT)_{15}$ [133]. The binding energy is higher for T/G than for A/C [133], which resulted in a lower CISS values for $d(AC)_{15}$ and $d(CC)_{15}$ wrapped SWCNT than the previously reported $d(GT)_{15}$ and $d(TT)_{15}$.

Effect of CISS on carrier localization was analyzed by our group in reference [134]. CISS-induced spins tend to increase the carrier localization length. This is because the CISS spin polarization is coupled with the carrier's momentum (either parallel or antiparallel, Figure 2.4(a)), and hence, in one-dimensional systems such as nanotubes, momentum flip must be accompanied by a simultaneous spin flip. Thus, backscattering is prohibited in the absence of spin-flip scattering events, which tends to increase the localization length (Figure 2.6(d)). This effect is manifested in the carrier transport properties in CNT-DNA systems [133, 134].

Later, we further extended this concept by developing chiral 2D SWCNT networks functionalized with aromatic short peptides known to interact with CNTs [135]. As discussed in the previous section, SWCNTs were embedded in supramolecular peptide fibers obtained by self-assembly. Like ssDNA, peptide functionalization of the CNT is also noncovalent and, therefore, the degree of interaction is susceptible to the chemical composition of the peptides. SWCNTs functionalized with L/D-Fmoc-FF (Fluorenylmethoxycarbonyl-diphenylalanine), L/D-Fmoc-AA (Fmoc-dialanine) and achiral Fmoc-GG (Fmoc-diglycine) showed different CISS behavior [135]. SWCNT functionalized with achiral Fmoc-GG did not give any detectable CISS signal, while functionalization with Fmoc-FF, which interacts strongly with CNT due to the presence of a major number of aromatic groups, showed the CISS effect. Quite remarkably, the CISS signal survived length scales longer than 1 μm, and the CISS values obtained from these random CNT networks are similar to the ordered chiral molecules under similar conditions [100].

Next, our group studied the influence of different chiral sources in the presence of CNT [104]. It is known that these types of aromatic short peptides can self-assemble by the application of different stimuli, addition of a chiral molecule glucono-δ-lactone (GDL) being one such stimulus [136]. The influence of GDL was studied with L/D-Fmoc-FF and Fmoc-GG functionalized

SWCNT (Figure 2.6(e)) [133]. Results showed that GDL only interfered with the process of self-assembly of short peptides, promoting the formation of chiral β-sheet secondary structure even in achiral Fmoc-GG peptides. The CISS effect originated from the supramolecular assembly of peptide fibers. Notably, CISS effect was observed in achiral molecules (Fmoc-GG) through the formation of chiral supramolecular fibers mediated by GDL.

2.9.3 Current research trends in CISS

Given the sheer variety of the chiral composites, CISS investigations on these systems are still at a nascent stage. For most of the CISS studies discussed above, the spin-dependent effect arises from the chiral molecules, which constitute the main carrier path, thereby leaving the true potential of these inorganic materials underutilized. These chiral organic molecules are insulators that carry very low current, and hence they are not suitable for practical device applications [97]. Therefore, there is a need to explore CISS effect in conductive media that have better electronic and spintronic properties. One main approach is to functionalize emerging electronic materials such as carbon nanotubes (CNTs) and various 2D materials (graphene, MoS_2 etc.) with chiral molecules. Our group is currently investigating this direction. As discussed above, we reported that chiral composites based on carbon allotropes can generate spin-polarized carriers in single-wall carbon nanotubes (SWCNTs). We have explored two types of chiral molecules: (a) helical shaped DNA [98] and (b) peptides [99], both showing the possibility of generating chirality-dependent spin signals. Investigating the potential transfer of the CISS phenomena from 1D to 2D materials is an uncharted avenue of research, which can potentially generate substantial spin polarization at room temperature, *due to their superior charge and spin transport properties*. The concept of CISS in 2D materials is therefore important for the next generation of ferromagnet-free spintronic devices. However, there are challenges in terms of feasibility, understanding, and reliable control of the phenomenon, which need to be addressed. One aspect of this work is to explore this avenue (Chapters 5, 6, and Appendix B).

2.10 Summary and overview

Spintronics devices, which use both spin and charge properties of electrons, are made of several magnetic materials, such as nickel, iron, cobalt, etc.; but shrinking the size of current spintronics devices with these magnetic materials is challenging. Two-dimensional (2D) van der Waals (vdW) magnetic materials can be useful in this context due to their flexibility to be integrated into different heterostructures on various substrates and their sensitivity to defect engineering. The recently discovered 2D magnetic materials could exhibit magnetoresistance (MR) effects. However, these effects are observed only at cryogenic temperatures [76, 137], which limits their practicality for real-world applications. Finding 2D magnets exhibiting large signals at room temperature is therefore needed in many spintronic and magnetic sensing applications. Vanadium diselenide (VSe_2) is a promising material in this regard since its monolayer can potentially act as room temperature ferromagnet.

VSe_2 multilayers have been predicted to exhibit large MR effects as described above, although experimental work in this area remains scarce, which motivates our work reported here (Chapters 3 and 4). Also, all of the above theoretical studies are mostly based on the semiconducting 2H phase of VSe_2, whereas experimentally, metallic 1T phase is the most common. CPP transport and CPP MR in 1T VSe_2 flakes have not been reported so far. The existence of CDW in VSe_2 can also have an impact on the CPP MR, which has not been investigated. Therefore, to investigate CPP magnetoresistance in 1T-VSe_2 ultrathin flakes, we established a reproducible nanofabrication method that enables us to perform transport measurements in the CPP geometry, which will be discussed in detail in Chapter 3. Next, in Chapter 4, we report electrical and magnetic behavior of ultrathin 1T-VSe_2 flakes in the CPP geometry at different temperatures.

As discussed above, CISS in 1D and 2D materials offers an alternative pathway towards ferromagnet-free spintronic devices due to their conductive nature and superior carrier mobility. Nevertheless, challenges persist in understanding the key factors of CISS involved in chiral composite materials, as well as the feasibility of transferring the CISS concept from 1D to 2D materials. As the basis of our chiral composite material, we choose carbon nanotubes (CNTs) and graphene to investigate the CISS effect across both 1D and 2D platforms. In this regard, the general consensus is that spin–orbit coupling is an essential element needed to observe the CISS effect, but there is currently a lack of experimental evidence to support this claim. To shed light on this key aspect of CISS in the 1D platform, in Chapter 5 we investigate the role of spin–orbit coupling on the chiral composite media by changing the diameter of the CNT functionalized by chiral molecules. Next, in Chapter 6, we utilize reduced graphene oxide (rGO), a well-known derivative of graphene, to explore the potential of harnessing the CISS effect in a 2D configuration. In Appendix B, as part of our ongoing work, via angle-resolved MR measurements, we demonstrate how the chirality-dependent CISS MR manifests in various configurations of magnetic and nonmagnetic terminal pairs.

Chapter 3: Magnetoresistance studies on VSe2 multilayers Fabrication and Characterization

Current-perpendicular-to-plane magnetoresistance (CPP MR) in layered heterojunctions is at the heart of modern magnetic field sensing and data storage technologies [138]. Van der Waals heterostructures and two-dimensional (2D) magnets opened a new playground for exploring this effect, although most 2D magnets exhibit large CPP MR only at very low temperatures due to their very low Curie temperatures [137]. As discussed in the previous chapter, vanadium diselenide (VSe_2) is a promising 2D material for room temperature magnetic applications since its monolayers can potentially act as room temperature ferromagnets [7].VSe_2 multilayers have been predicted to exhibit CPP MR effects [98], although experimental work in this area remains scarce. This motivates our work on CPP MR studies on VSe_2 multilayers. In this chapter we will discuss the fabrication and characterization steps, and the electrical transport and MR data will be discussed in Chapter 4.

Bulk VSe_2 single crystal samples, synthesized using Chemical Vapor Transport, were obtained from a commercial vendor, hq Graphene. To create the desired CPP based geometry, a thin (20-120nm) exfoliated layer of VSe_2 underwent various nano-fabrication steps. Below, we outline the nanofabrication process employed. Furthermore, we present a comprehensive explanation for the selection of the exfoliated VSe_2 flakes, based on the characterization process.

3.1 Device fabrication

To measure CPP MR, we propose a three-step fabrication method to sandwich the isolated 2D-TMD flakes between two metal layers. In addition, to eliminate the impact of contact resistance and interconnection lines on the MR measurements, a 4-point measurement technique has been opted and implemented. In this approach, the bottom contact is formed as an isolated metallic finger which is not connected to any metallic side pads. The metallic fingers are arranged at the center of the fabricated device and serve as the foundation of the CPP-MR architecture. The TMD flakes have been transferred on these metallic fingers via mechanical exfoliation using scotch tape.

Due to physical exfoliation, the VSe_2 flakes have different shapes and thicknesses, and they are randomly laid on the metallic fingers. The desired 2D flakes are the ones that are sitting properly on the bottom metallic fingers and showing no sign of oxidation. The flakes are characterized by their Raman spectral fingerprints, relative amount of elemental composition (EDX), layer thickness (AFM), surface roughness and topography (AFM), and their crystallinity (XRD), all of which have been discussed later in this chapter. Next, the top metallic contacts and the metallic interconnecting paths are designed and fabricated. The active region of the die, where the 2D-TMD sandwich structure is located, was covered by an insulating material to provide structural stability and isolation from the ambient. At this step, the fabricated device is ready for electrical and magnetic measurements. The schematic of the active region of substrate with flakes sandwiched between metallic fingers are depicted in Figure 3.1. In the next section, we explain in detail the fabrication steps and the characterization procedures.

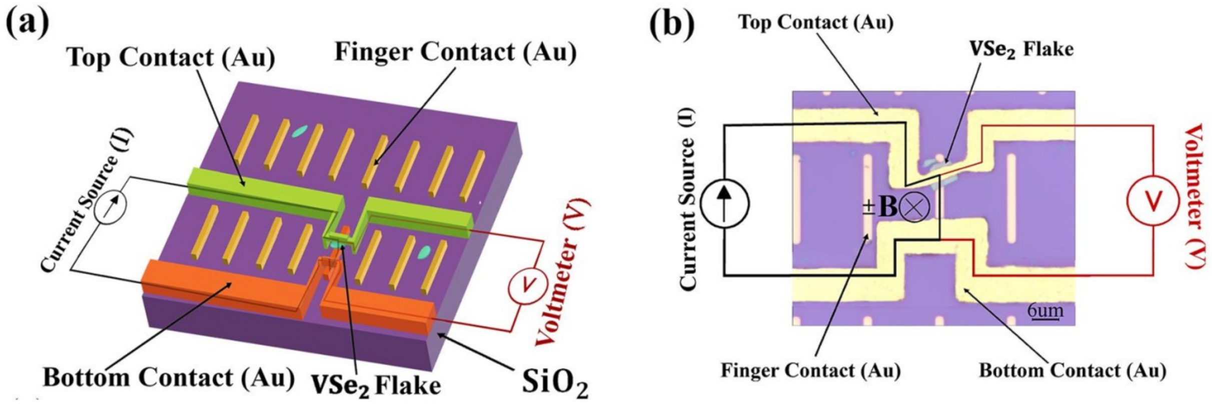

Figure 3.1: **(a)** Schematic representation and **(b)** optical microscopic image of the four-terminal CPP measurement setup.

3.1.1 First fabrication step (bottom contact)

In the 1st fabrication step, a Si substrate with 300nm thermally grown SiO_2 is cleaned by dipping in a piranha solution for 20min. After drying with nitrogen gas, the substrate is loaded in YES YES3TA HMDS Oven. In this way, the clean Si/SiO_2 substrate is exposed to HMDS that enhances surface adhesion. HMDS forms the bridge between organic photoresist molecules and substrate surface. Next, AZ5214E positive photoresist is spin-coated onto the substrate at a rotational speed of 5000 rpm for 45sec. This process resulted in the formation of a 1.25µm thick photoresist layer on the substrate. Afterward, the sample undergoes a prebake step at 100°C for 1 minute on a hotplate. Following this, the pattern of metallic fingers is transferred using a SUSS MA/BA6 mask aligner applying a dose of 100mJ/cm^2. To create metallic patterns with well-defined edges, the image reversal technique is used, followed by lift-off procedures. To reverse the tone of positive photoresists, two additional steps are necessary: an image reversal baking step and a flood exposure process. These steps make the initially exposed areas resistant to the developer, while allowing the unexposed areas to be developed. The substrate was subjected to a reversal bake at 100°C for 45sec on the hot plate. Subsequently, a flood exposure was applied using a dose of 300mJ/cm^2 by the mask aligner. Next, the specimen was developed in the MF-319 developer for 50sec. The chromium and gold layers were deposited with thickness of 5nm and 45nm, respectively, at a pressure of 7.5E-7torr by electron beam evaporation (KJL E-beam evaporation (Gomez)). To form gold bottom fingers and electrical pads, the lift-off procedure was performed using Remover PG.

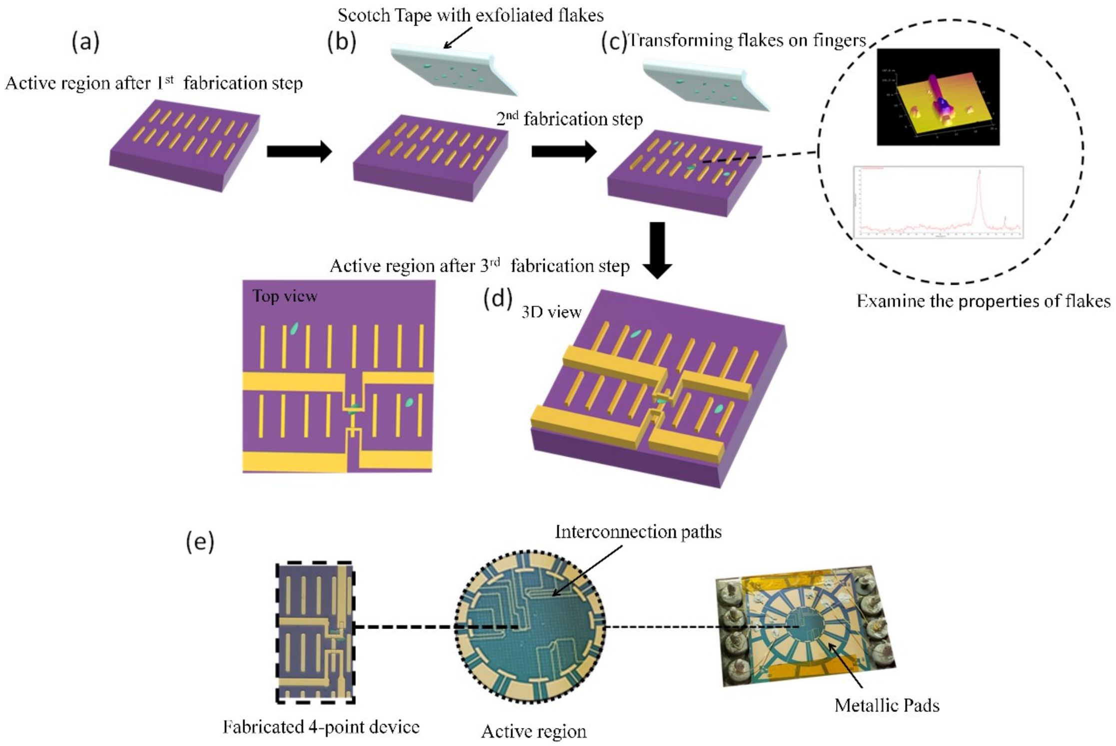

Figure 3.2: (a-d) Fabrication steps for VSe2 CPP MR devices. **(e)** Optical image of fabricated devices.

3.1.2 Second fabrication step (physical exfoliation and characterization)

In the 2nd step, VSe$_2$ flakes are obtained through mechanical exfoliation of the as-purchased bulk *single crystal* sample, using scotch tape. After exfoliation, these flakes are transferred onto the substrate, resulting in a random arrangement of the flakes on the substrate surface. Subsequently, the flakes that happen to land on the bottom metallic fingers are subjected to further characterization (described below). The primary objective of the characterization is to obtain oxide-free flakes with a thickness ideally below 100nm. In the next step, the pattern of top metallic contacts and interconnections is designed specifically for the selected flakes, considering their individual properties and positions on the substrate.

3.1.3 Third fabrication step (top contact)

As shown in Figure 3.2(c), following the characterization of the transferred flakes (as described below), oxide-free VSe_2 flakes with different thicknesses have been selected for the next metallization step. First, the substrate is soaked in acetone for 30 minutes and then rinsed with IPA (Isopropyl alcohol) and DI (Deionized) water to remove any glue residuals from the scotch tape. Then, the cleaned substrate is coated with PMMA-950-A8 using a rotational speed of 4000rpm for 45 seconds, resulting in a 580nm thick photoresist film. Next, the substrate is baked at 180°C for 4 minutes on a hotplate. Subsequently, the substrate is exposed to an electron beam using the EBL-Raith150 system with an electron high tension (EHT) of 10kV using an aperture of 30μm. This electron beam exposure is used to transfer the pattern of top contacts and interconnection lines onto the photoresist. The exposed specimen was developed in MIBK 3:1 for 40sec and IPA for 20sec. After monitoring the quality of pattern, the electron beam evaporation was used to deposit chromium and gold layers with thicknesses of 7nm and 240nm, respectively. Next, the lift-off process was carried out by immersing the sample in acetone for a duration of 12 hours. Finally, an insulating organic coating is applied by drop casting onto the active device area to protect the underlying VSe_2. The devices fabricated in this fashion have exhibited a high degree of yield and reproducibility. Any annealing step is avoided in order to minimize the formation of Se vacancies that can potentially introduce defect-induced MR responses [86].

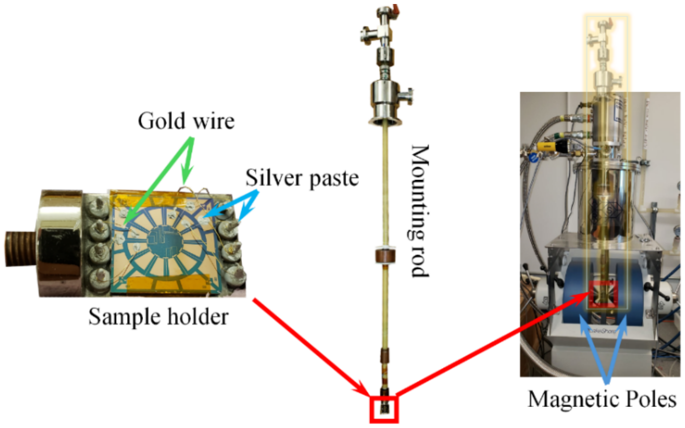

Figure 3.3: Device setup for measuring magnetoresistance at different temperatures.

After the fabrication of the devices, the samples are mounted on the sample holder. Electrical connections between the holder's pins and the 4 substrate pads are established using gold wire and silver paste, as shown in Figure 3.3. This setup allows for the connection of measurement devices, such as UMI, to the fabricated four-terminal devices. The holder is then placed inside the device for the measurement of its magnetic properties at different temperatures.

3.2 Characterization of VSe_2 flakes

In this section, a detailed explanation is provided for the criteria used to select the desired exfoliated flakes on the gold fingers. The focus is on identifying non-oxidized flakes with well-defined thicknesses, ideally below 100 nm. As discussed below, the obtained thickness range was 20–160nm.

3.2.1 Raman results

Raman spectroscopy is a powerful characterization tool that provides valuable insights into lattice vibrations, phonon modes, and electronic band structures of TMDs [139-141].The principle behind Raman spectroscopy is based on the inelastic scattering of light. When photons from the incident light interact with the sample's molecular vibrations, it causes a portion of the scattered light to either lose or gain energy compared to the incident light.

The energy shifts in the scattered light correspond to the vibrational energy modes of the molecules in the sample. The Raman spectrum represents the intensity of the scattered light as a function of the frequency shifts and contains peaks that are characteristic of the material. These peaks can therefore be used to identify the chemical composition and structural properties of the sample.

All Raman spectra in this work were collected at room temperature using Thermo DXR2 Raman Microscope System. Laser wavelength is set to 532nm. Maximum laser power is optimized to avoid inflicting damage to the thin flakes and is set to 3mW with 100 sampling iteration. With these optimized settings, no evidence of laser-induced heating has been observed in the measured flakes.

The room temperature Raman result (532nm laser) is shown in Figure 3.4. The characteristic peak of 1T-VSe_2 is observed at approximately 207cm^{-1} (A_{1g} mode), representing the out-of-plane vibration of two Se atoms around one V atom. The second peak, located at approximately 135cm^{-1}, corresponds to the in-plane vibration of the atoms within the crystal lattice (E_g mode).

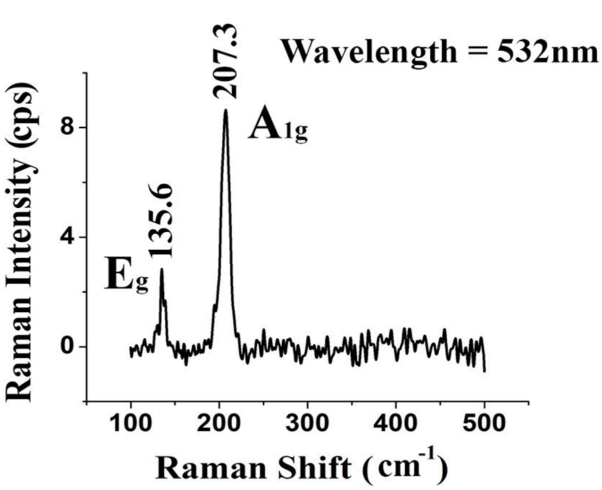

Figure 3.4: Typical Raman characteristics of the exfoliated VSe_2 flakes, indicating the signature peaks, and absence of any oxidation.

In contrast to the Raman results of other groups, where the A_{1g} peak is consistently observed while the E_g peak is barely detected due to high signal-to-noise ratio [72, 86, 87], our Raman measurements clearly exhibit both signature peaks (A_{1g} and E_g) of 1T-VSe_2.

In the Raman results, an oxidation peak may appear at 250–340cm^{-1} when the VSe_2 nanosheet is irradiated under high laser power during Raman data collection or when it is exposed to ambient conditions for an extended period, as depicted in Figure 3.5. In the Raman results of all selected flakes chosen for the 3rd fabrication step, no oxidation peak attributed to VO_x ($2 < x < 2.5$) has been detected.

3.2.2 EDX results

To determine the elemental composition of the VSe_2 flakes, Energy Dispersive X-Ray Analysis (EDX) was performed. In this method, when the sample is bombarded with the electron beam, it causes the emission of characteristic X-rays from the atoms within the sample. EDX utilizes an X-ray detector that records the energy of each X-ray, and the resulting data form an energy spectrum.

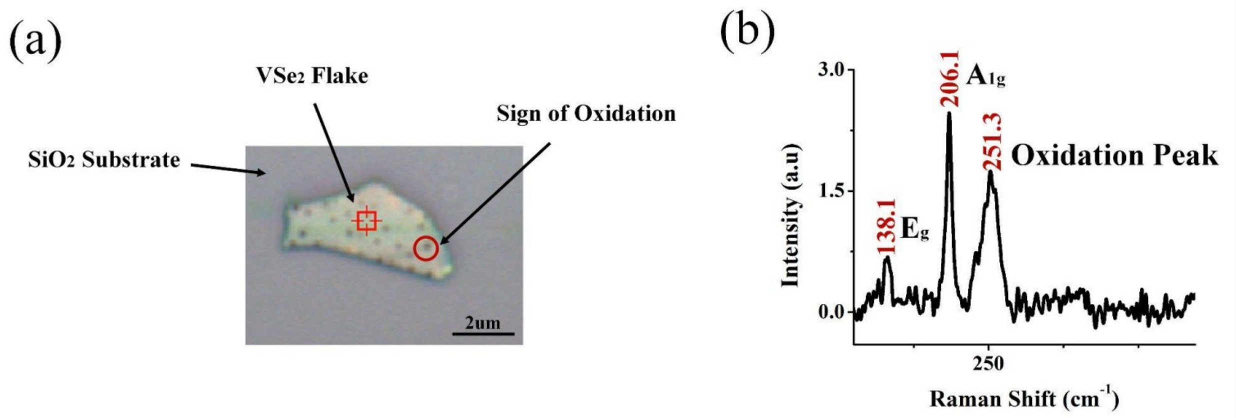

Figure 3.5: (a) Optical microscopic image of a typical VSe_2 flake after a week of exposure to the ambient conditions. Signs of oxidation can be seen. **(b)** Raman spectroscopy (532 nm laser) of an oxidized flake, showing the broad oxidation peak at ~251 cm^{-1} .

The EDX spectrum shows the intensity of X-rays as a function of their energies. The characteristic X-rays emitted by different elements in the sample have distinct energies, allowing EDX to identify the elements present in the sample. The EDX results, obtained using Zeiss Sigma FESEM are shown in Figure 3.6, confirming the absence of oxygen and the presence of both V and Se, with approximately 1:2 stoichiometric ratio in the VSe_2 flakes.

3.2.3 AFM results

The atomic force microscope (AFM) technique was used to characterize the thickness and roughness of the transferred VSe_2 flakes. In this technique, a sharp tip is scanned in a raster pattern over the surface, and a feedback loop is used to adjust the parameters required for imaging the surface. The cantilever vibrates or oscillates at a fixed frequency, and the amplitude of this oscillation is used to detect changes in the tip-sample interaction forces. These changes in forces are translated into height variations on the sample's surface, allowing the AFM to create a detailed topographic map of the sample.

The thickness of VSe_2 flakes has been measured after mechanical exfoliation. Flakes with thicknesses greater than 200nm or possessing a rough surface were excluded from the selection process. As shown in Figure 3.7 , the flakes with the desired thickness range (ideally below 100nm) and appropriate physical contact and roughness were chosen for further processing.

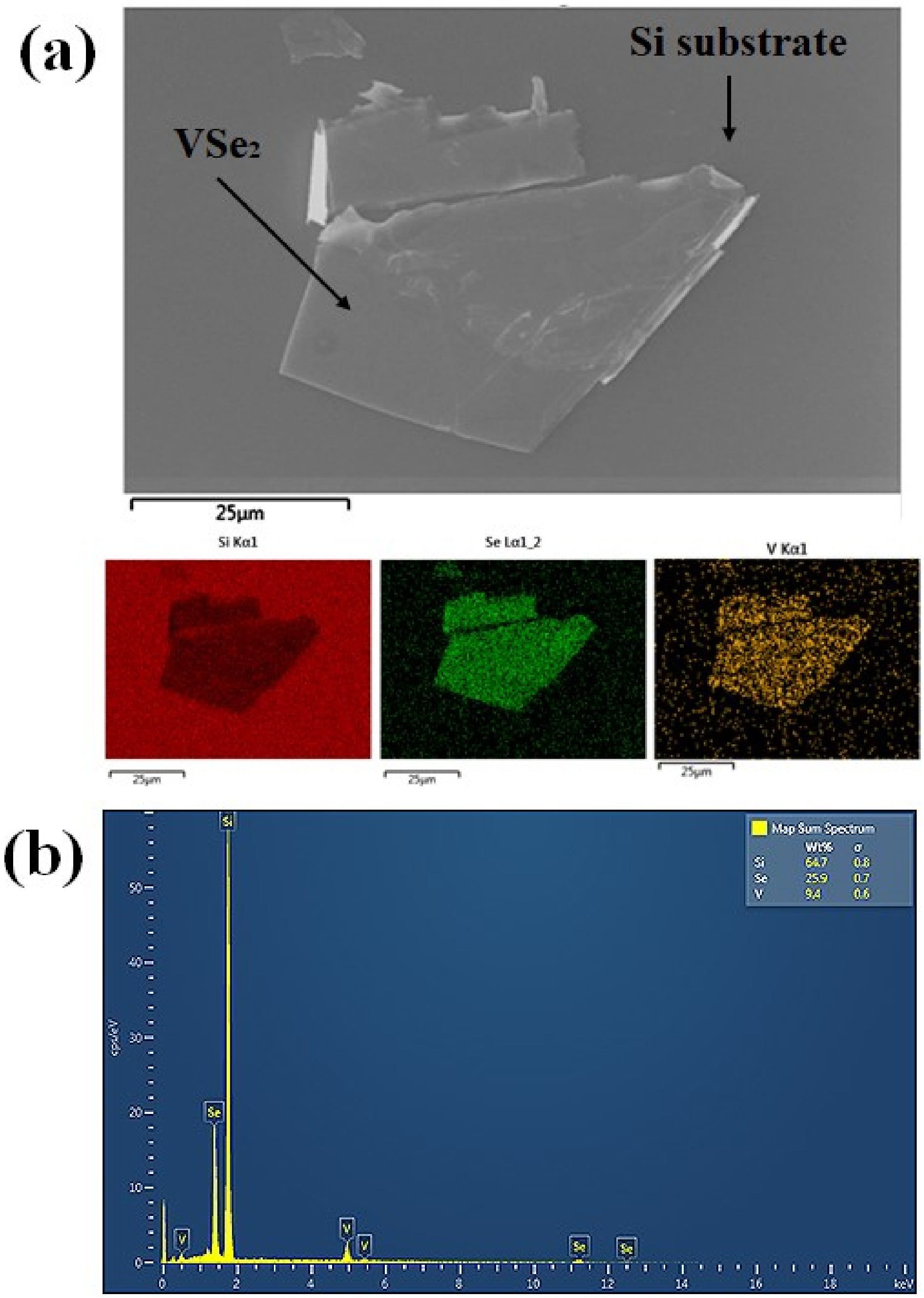

Figure 3.6: (a) SEM image of a VSe_2 flake on Si substrate, and elemental analysis. **(b)** EDX analysis of VSe_2 flakes on Si substrate.

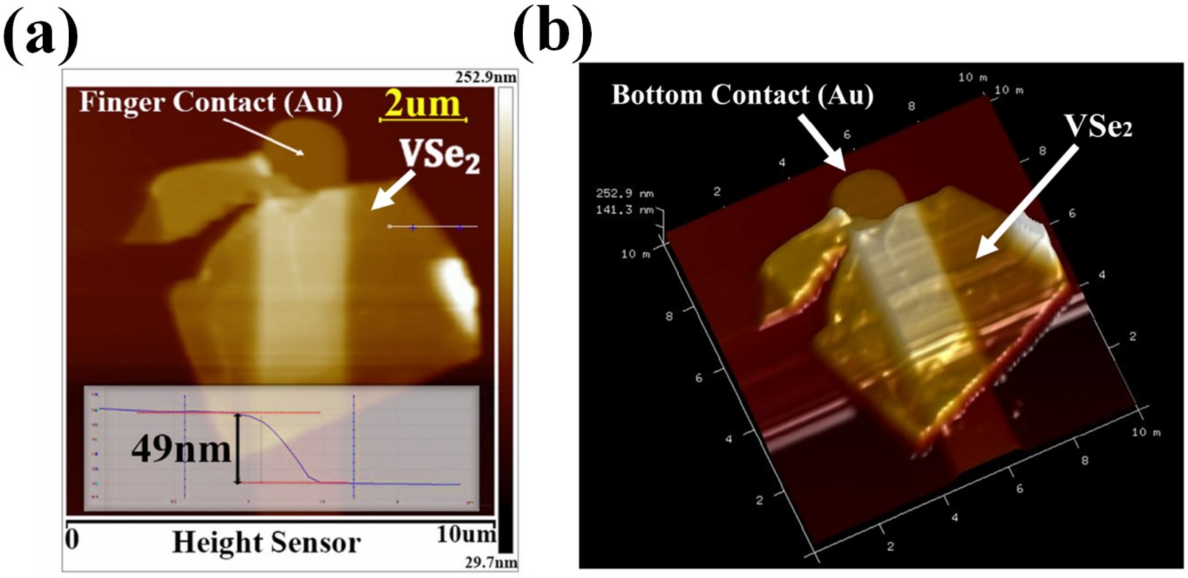

Figure 3.7: (a), (b) AFM results showing bottom Au finger in contact with an exfoliated VSe_2 flake on the top. The bottom inset in (a) shows the flake thickness as determined by the height scan along the horizontal line in the main image.

3.2.4 XRD results

X-ray diffraction analysis (XRD) is a non-destructive technique employed to determine the crystallographic structure of VSe_2. This method relies on elastic scattering, where the regular array of atoms generates waves that undergo destructive interference in most directions but add constructively in specific directions. By analyzing the angles and intensities of these scattered beams, a three-dimensional representation of the electron density within the crystal can be obtained. The XRD data from VSe_2 at room temperature were obtained using Rigaku XRD Ultima IV, and the result is presented in Figure 3.8. The XRD analysis reveals the highly crystalline nature of our samples, evident from the presence of sharp and strong peaks, including (001), (002), (003), and (004) reflections. The data closely matches both the specifications provided by the vendor, hq Graphene, and also with the results obtained by other research groups. In [6], Cao et. al. grew VSe_2 sample and used mechanical exfoliation to obtain thin layer of VSe_2, followed by XRD characterization. XRD data were also obtained by Liu et. al. [72] and Xue et. al. [87] for their CVD grown VSe_2 nanosheet. Our data matches closely with these references.

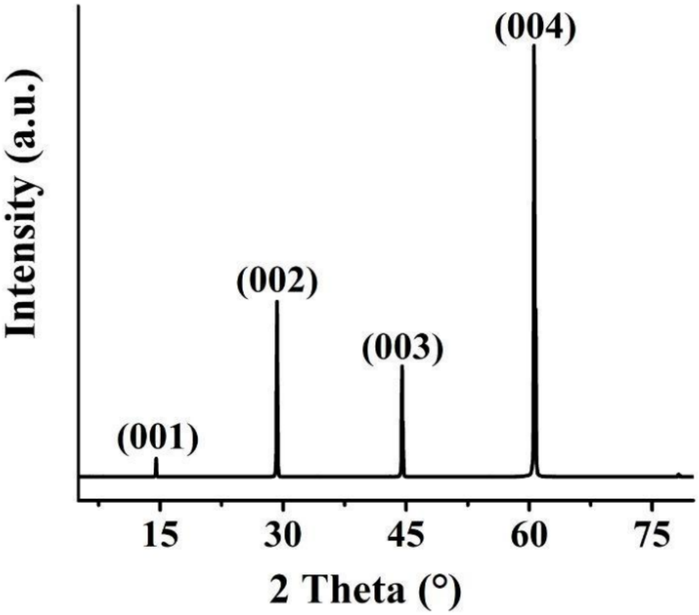

Figure 3.8: The XRD analysis of VSe_2.

3.3 Summary and conclusion

In this chapter we have discussed in detail the fabrication of four terminal CPP devices, with 1T VSe_2 flakes as the active layers. We have also characterized the flakes using various techniques. In the next chapter (Chapter 4), we will discuss electrical and magnetotransport experiments on these devices.

Chapter 4: Electrical and Magnetoresistance Measurements on Exfoliated VSe2 Flakes

4.1 Overview

In this chapter we report CPP MR results obtained from 1T-VSe_2 ultrathin flakes, revealing a large (~60%–70%), positive, linear, and non-saturating CPP MR, which persists close to room temperature (~250K), in a relatively small magnetic field range of ±12kG. The CPP MR has been found to increase with decreasing flake thickness. As discussed below, the CPP MR originates due to the intrinsic inhomogeneity in the CPP transport path, and exhibits unprecedented immunity against thermal fluctuations, leading to increasingly enhanced MR as temperature is increased, even significantly beyond the charge density wave transition temperature. The observed 'thermally-driven' MR features are remarkably robust and reproducible, and can offer a viable route for developing practical room temperature 2D based magnetic sensor technologies. Our results also suggest that harnessing similar effects in other 2D systems could result in large MR as well, thereby motivating further research on CPP transport in these systems, which has been relatively unexplored so far.

4.2 Results and discussions

Device schematic and an optical microscopic image of the CPP MR measurement setup are shown in Figure 4.1(a) and (b), respectively, and the current-in-plane (CIP) measurement setup (control experiments) is depicted in Figure 4.1(c).

Consistent with earlier studies on current-in-plane (CIP) geometry, in-plane charge conduction has been found to be metallic, with in-plane resistance decreasing with decreasing temperature, as shown in Figure 4.2(a) [6, 72, 85, 94, 142, 143]. Residual resistivity ratio, defined as R(250K)/R(9K), is ~4, consistent with previously published work on 1T VSe_2 samples with similar thicknesses [94, 142]. An upturned ‘kink’ is observed around 110K, which is the bulk CDW temperature, but the global trend remains metallic, consistent with literature [6, 85, 94, 142, 143]. The kink appears due to the onset of CDW, which opens up a partial bandgap and depletes density of states on parts of the Fermi surface [87, 144]. The partial gap opening has been found at the *M* point in the first Brillouin zone by angle resolved photoemission spectroscopy, while the Fermi surface at *Γ* point remains intact [87, 144, 145].

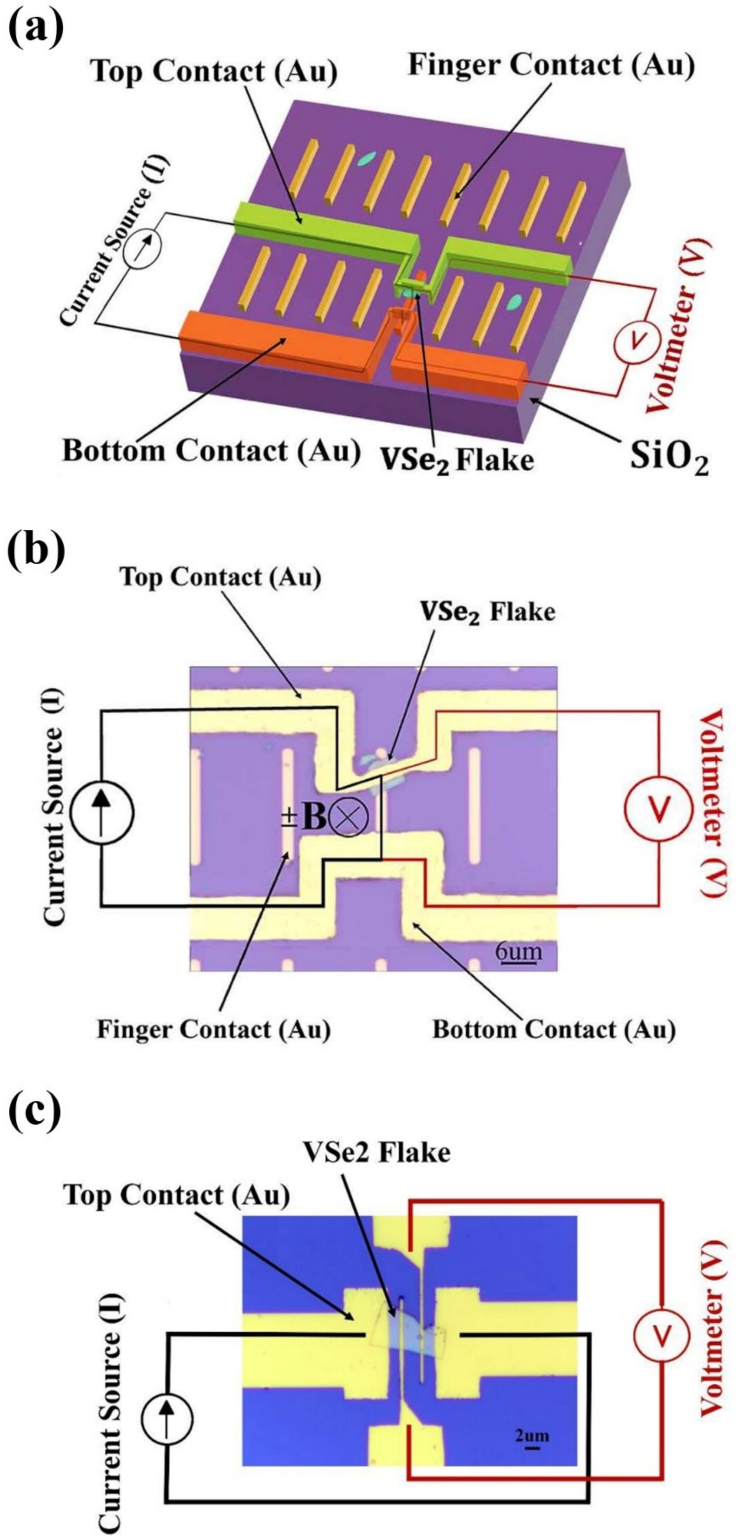

Figure 4.1: (a) Schematic representation and **(b)** optical microscopic image of the four-terminal CPP measurement setup. For MR studies, the magnetic field is always applied perpendicular to the sample plane. **(c)** Typical measurement setup for current-in-plane (CIP) studies.

The slope tends to decrease slightly around 200K as the temperature increases, which can be attributed to the narrowness of the *d* band [143]. In the lowest temperature limit (∼10K), the resistance appears to saturate, although no significant resistance upturn has been observed in Figure 4.2(a), which indicates absence of any defect-induced weak localization effect in this range [6, 72].

Out-of-plane (CPP) charge conduction, on the other hand, shows a non-trivial behavior. Similar to the CIP response, it shows an anomaly in the vicinity of the CDW temperature (∼110K), as indicated by the shaded region in Figure 4.2(a). However, unlike the CIP response, which exhibits a global metallic trend, the CPP response shows *a metallic trend only below the CDW transition range and a mixed metallic and semiconducting behavior above the CDW transition range*. As shown in Figure 4.2(a), in the ∼10–70K range (i.e. below the CDW transition window) the CPP resistance shows a metallic trend i.e. resistance increases as the temperature increases. However, above ∼125K (i.e. above the CDW transition window), we observe a mix of weak metallic and semiconducting response. Such *mixed metallic and semiconducting behaviors above the CDW range, accompanied with a metallic behavior below the CDW range* have been observed in multiple samples and hence these are confirmed to be the signature features of CPP transport. The CPP data shown in Figure 4.2(a) corresponds to a sample of thickness ∼24nm. The mixed metallic and semiconducting behavior that manifests above the CDW temperature is dependent on sample thickness. Due to weak interlayer coupling (as evidenced by band structure calculations as well as spectroscopic studies performed on bulk and monolayer) [85, 89], energy bands are weakly dispersive in the *out-of plane* $(\widehat{k_z})$ direction.

CPP current–voltage (I-V) characteristics have been measured at different temperatures and they are always linear, at least in the bias range of ±0.5µA, as shown in Figure 4.2(a) *inset*. Applied bias was kept in this range to avoid sample damage in the CPP measurement geometry. Existence of mixed metallic and semiconducting behaviors in CPP transport above the CDW transition range requires a closer look.

Out-of-plane conduction can occur via phonon-assisted momentum randomization in this direction, which will result in metallic behavior. In addition, out-of-plane transport can also happen via phonon-assisted tunneling or hopping through the states in the interlayer region, which will result in a semiconducting trend.

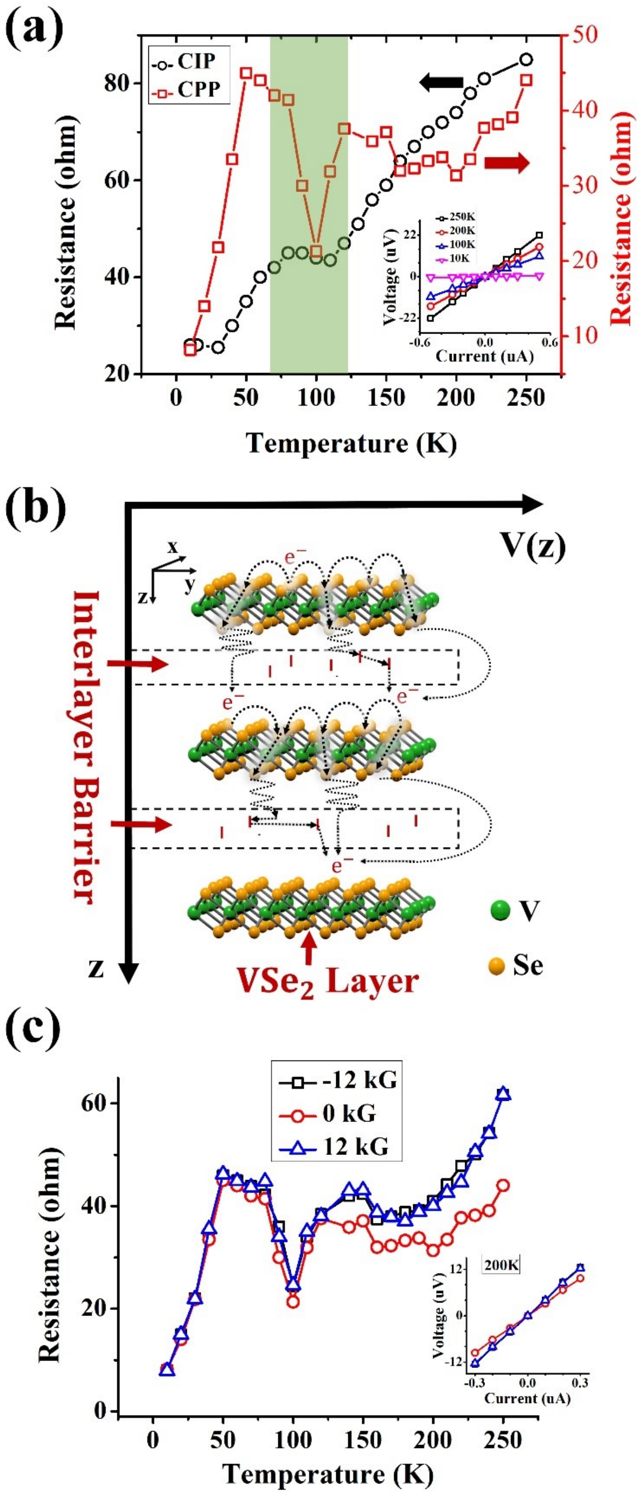

Figure 4.2: (a) Comparison of CPP and CIP transport. The CDW transition window is shown by the shaded region. CPP I–V characteristics have been shown in the inset, with linear behavior over the measured bias range. **(b)** Schematic description of the electron paths and transport mechanisms during CPP transport. **(c)** CPP resistance (R) as a function of temperature (T) both in presence and in absence of an out-of-plane magnetic field of ±12kG. A clear positive MR has been observed above 110K. The inset shows switching of the CPP I–V due to the magnetic field. Sample thickness ~24nm.

As shown schematically in Figure 4.2(b), due to weak interlayer coupling, *interlayer regions* can be viewed as *potential barriers* or, *'low mobility regions'* sandwiched between each pair of neighboring conductive VSe_2 layers. We note that existence of any strained VSe_2 layer in the stack can also cause band gap opening in that layer in the high temperature range, and contribute to the potential barrier [146]. Finally, CPP transport may also have an in-plane (or, intralayer i.e. $\widehat{k_x} - \widehat{k_y}$) component, which will mimic the same metallic temperature dependence as the CIP resistance. The overall CPP transport behavior in a given temperature range will be dictated by whichever mechanism is the strongest, and this could explain the mixed metallic and semiconducting behavior observed in our data. For CIP measurements, on the other hand, the interlayer phonon-activated transfer mechanism is virtually absent, resulting in a global metallic trend.

For the sample in Figure 4.2(a), which has a nominal thickness of ∼24nm, the slope of CPP *R vs T* is metallic in the ∼160–250K temperature range, and hence momentum randomizing phonon scattering appears to be the dominant process in this range. As the temperature is reduced below ∼160K, this mechanism is suppressed, as evidenced by significantly reduced slope of R vs T. Interlayer transport occurs via tunneling with a weak contribution from thermal hopping in this range. We note that in this temperature range, the system approaches its CDW phase with partial gaps gradually opening in the vicinity of the Fermi level. Due to the CPP nature of the transport, which is very sensitive to the details of the states near the Fermi level of *each* layer, such gap openings have a profound impact on the measured resistance.

Thus, the increasing trend of CPP resistance from 150K to 110K could be attributed to the gradually diminishing density of states at the Fermi level as the sample is cooled, and thermally activated transport. The sharp drop in resistance around 100 K could be due to the appearance of interlayer states while the material undergoes transition from its normal state (>110K) to incommensurate I-CDW state (~80–110K). Below 80 K, the material is in commensurate CDW state, with an enlarged unit cell of 4a × 4a × 3c[147, 148]. The enlarged unit cell may suppress interlayer tunneling as well as any thermally activated transport compared to the normal state, which could explain metallic behavior below this temperature. Figure 4.2(c) shows temperature evolution of CPP resistance (~24nm sample thickness) under zero magnetic field and an out-of-plane magnetic field (B) of ±12kG. A clear and strong positive MR is observed above the CDW temperature of ∼110K, and the MR signal increases with temperature.

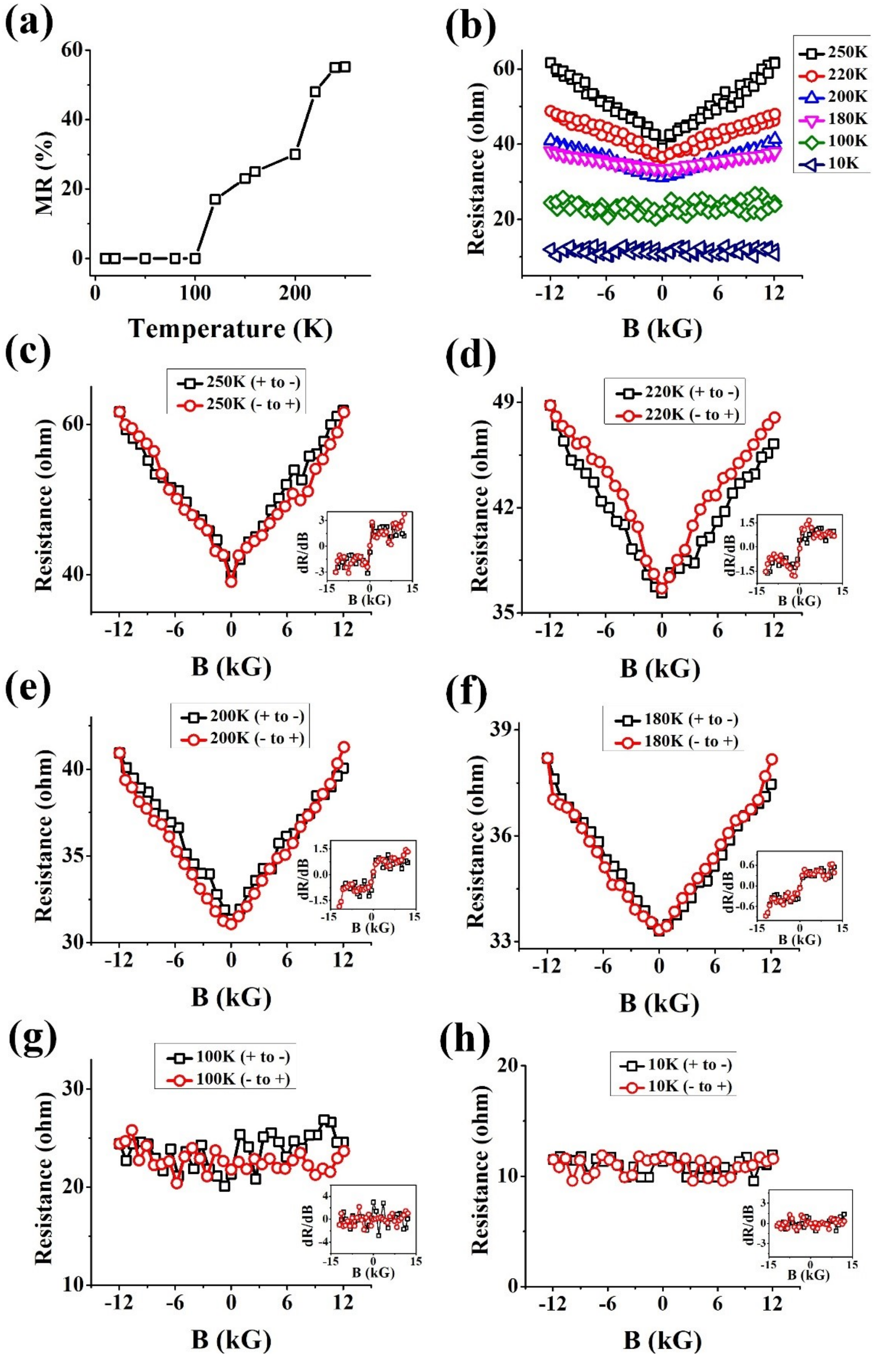

Figure 4.3: (a) Evolution of CPP MR (±12kG field range, ~24nm thickness) with temperature. CPP MR is largest at ~250K, and decreases with cooling, and vanishes at ~110K. (**b)–(h)** CPP resistance as a function of an out-of-plane magnetic field B at various temperatures. The *insets* in **(c)–(h)** show the linear dependence of resistance on the magnetic field.

Relatively parallel slopes of the curves in Figure 4.2(c) indicate that the transport mechanism is fundamentally the same both in presence and in absence of the applied magnetic field, thereby ruling out the possibility of any field induced metal–insulator transition. The inset in Figure 4.2(c) shows the switching of the CPP I–V characteristics due to the applied magnetic field. The MR vs. temperature trend observed in Figure 4.2(c) is plotted in Figure 4.3(a), which shows that the CPP MR effect is enhanced with increasing temperature. In these plots, MR is defined as [R(±12 kG)–R(0)]/R(0) × 100%], where R is CPP resistance and ±12 kG is the out-of-plane magnetic field.

To further explore the MR behavior of this sample, we measured CPP resistance (R) as a function of the out-of-plane magnetic field (B) at several temperatures. Figure 4.3(b)–(h) show the MR responses, *which gradually diminish as the temperature is reduced*. The MR value is maximum (~60%, over ±12kG) at the highest measured temperature of 250K. The MR disappears at ~110K, which coincides with the bulk CDW temperature. As shown in the insets of Figure 4.3(c)–(h), the slope of the MR response (dR/dB) resembles a *step function* relative to B in the measured field range of ±12kG. This implies that the MR response is primarily *linear* relative to B, with a very narrow region of quadratic dependence in the neighborhood of zero magnetic field, where the step transition takes place (additional analysis described below). All MR measurements have been performed at 0.1μA current bias. Figure 4.4(a) shows data from a sample with thickness ~20nm, where the observed CPP MR is ~70% over ±12kG, at 250K.

R studies on VSe_2 have been reported in the past, but all of them employed CIP geometry. For example, [6] reported weak (~2%) positive CIP MR over an out-of-plane magnetic field range of ±10T (or, ±100kG), *at temperatures lower than ~60K. At even lower temperatures (~2K)*, a negative MR may emerge due to weak localization [6]. Liu et al [72] found a positive CIP MR of about 50% over an out-of-plane magnetic field range of ±15T (or, ±150kG) *at ~1.9K*, which is significantly below the CDW temperature. This MR effect gradually disappears as the temperature rises to CDW temperature (110 K) and a very weak positive MR (~0.3% over ±150kG) emerges above CDW temperature. This was explained using a classical linear model by invoking CDW induced mobility fluctuations. Similar results have been reported in [87], where ~35% positive MR was observed *at ~2K*, over a field range of ±15T (or, ±150kG).

It is therefore clear from Figure 4.2 and Figure 4.3 that the CPP transport and MR results are fundamentally different from the CIP results reported so far in the literature, both in terms of temperature range as well as magnetic field range where they manifest.

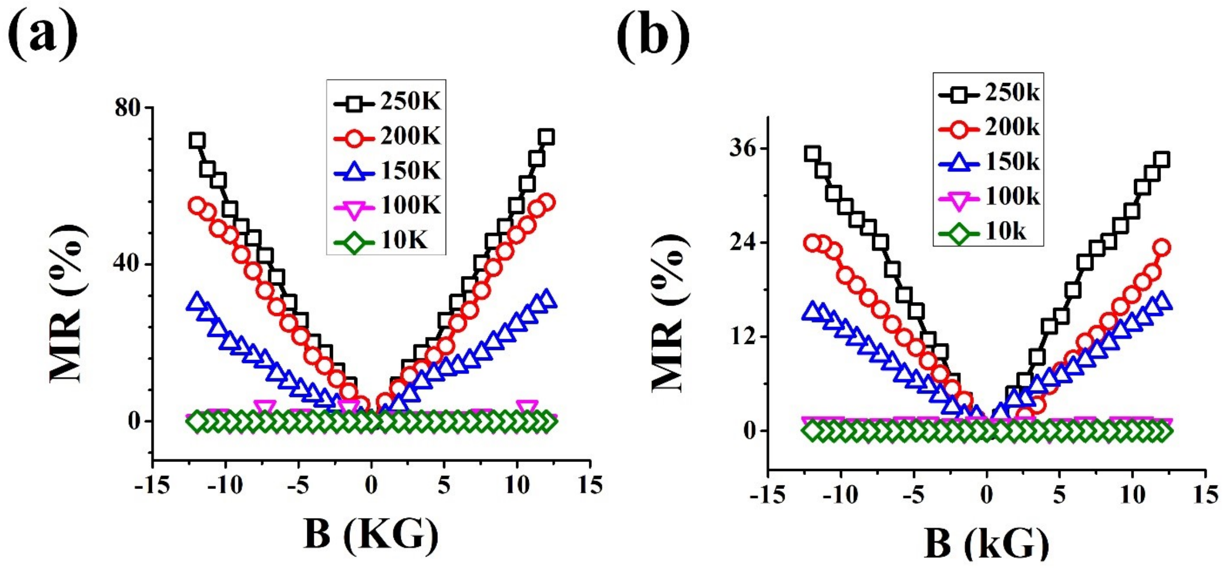

Figure 4.4: CPP MR for VSe_2 samples with thicknesses **(a)** 20nm and **(b)** 45nm. Magnitude of CPP MR increases with increasing temperature. At a given temperature, thinner samples show larger CPP MR.

To explore the origin of the observed low field positive *linear* MR, we can rule out the classical MR. In this case, a *quadratic* positive MR can arise when the magnetic field exerts a Lorentz force on the moving charge carriers, causing their trajectories to bend, which in turn increases the resistance. In our case, charge transport is primarily normal to the plane, parallel to the direction of the applied magnetic field. Hence any Lorentz force effect should be negligible.

Even the in-plane component of CPP transport (Figure 4.2) is not expected to result in any positive MR in the measured low field range of ±12kG. This is because the CIP MR data, where the entire transport is in-plane and perpendicular to the magnetic field, did not show any positive MR under our experimental conditions (±12kG, 250K), as shown in Figure 4.5(a). Also, the classical MR effect weakens with increased phonon scattering at higher temperatures, contrary to what we observe.

We also rule out any spurious MR contributions from the Au contact lines or any pinhole shorts through the VSe_2 flakes. As shown in Figure 4.1(a) and (b), four-point measurement techniques have been used to minimize the resistance from the contacts. The flake surfaces are highly uniform, with no evidence of pinholes. Control experiments without the VSe_2 layer show purely metallic temperature dependence of resistance and no MR effect at all, as shown in Figure 4.5(b-d).

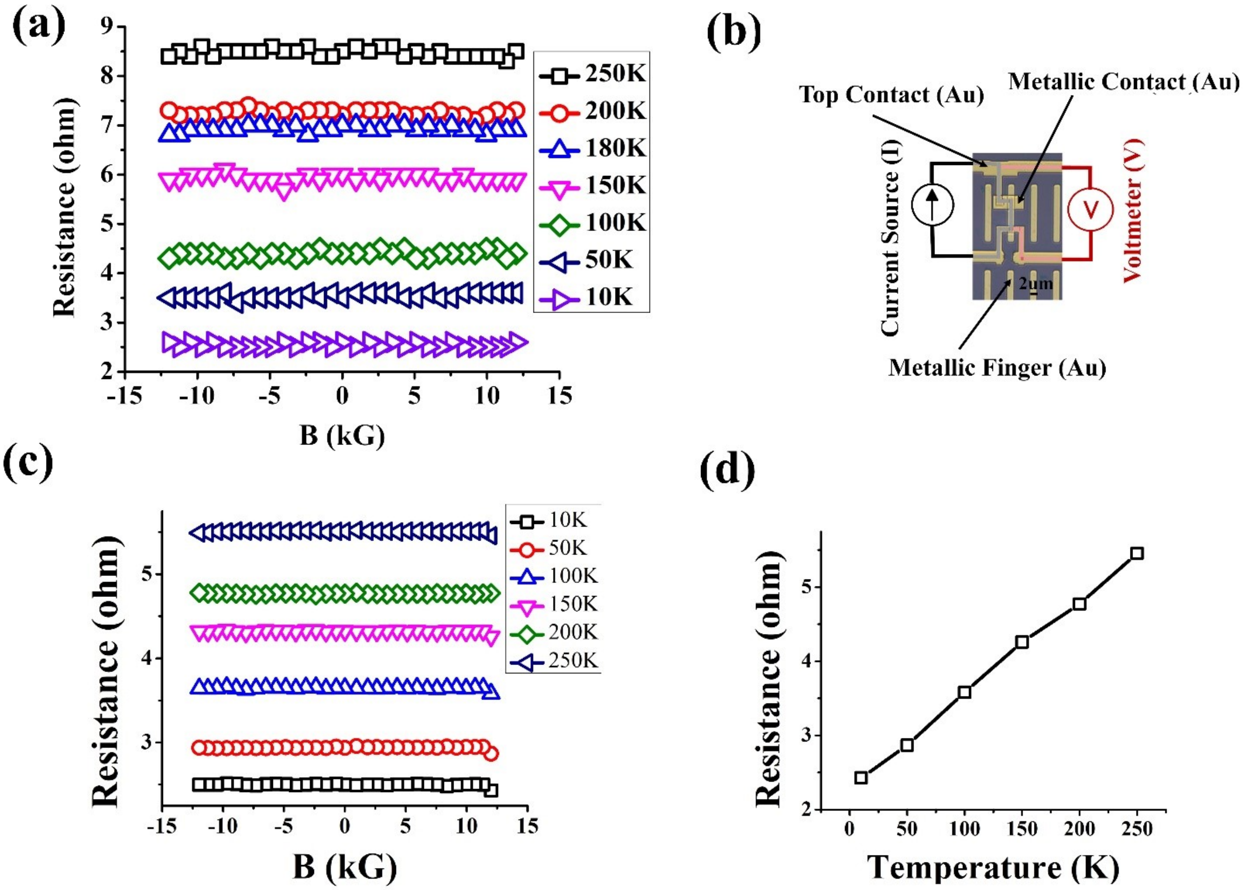

Figure 4.5: (a) CIP MR of VSe_2 flakes in ± 12kG field range (magnetic field applied normal to the plane), showing no detectable MR effect. This confirms that the CPP MR observed before does not solely originate from any in-plane component in the current path. CPP MR measurements without any VSe_2 flakes: **(b)** Four-point measurement setup, **(c)** Absence of any MR effect and **(d)** Metallic temperature dependence of resistance. Absence of any MR in (c) confirms the absence of any spurious MR effects from the Au interconnect lines.

Linear MR can arise due to quantum effects when each Landau level is distinct, as described by the condition $\hbar\omega_c \gg k_B T$, where the first term represents typical Landau level splitting (ω_c being cyclotron frequency), and the second term represents thermal broadening [149, 150]. In the extreme quantum limit, where the magnetic field is so strong that only the lowest Landau level is occupied, a linear positive MR can be observed [149, 150]. In our case, since the MR effect is observed in a relatively low magnetic field range of ±12kG and high temperature of ~250K, the above condition of extreme quantum limit is not satisfied. Even qualitatively, in our case MR increases with temperature (T) for a given magnetic field (Figure 4.2(c)), which contradicts the above model, and hence this mechanism can be ruled out.

The observed MR effect does not appear to be spin mediated. Due to the high temperature, low field conditions of our experiments we can rule out positive MR originating from Zeeman splitting of the Landau levels [151]. Even though some studies have indicated that mono- and few-layer 1T VSe_2 can be ferromagnetic, it is actually paramagnetic in its bulk form ($\gtrsim$10nm), which corresponds to the present case [7, 78, 85, 86, 89, 93]. Spectroscopic studies did not find any evidence of spin-splitting at the Fermi level [6, 89-92]. Any spin dependent MR effect (such as those observed in the case of CrI_3) is negative, and exhibits a stepwise response to the magnetic field due to gradual switching of magnetization of each layer [137, 152-155]. None of these features have been observed in the present case.

The unique feature of the observed CPP MR is its unusual dependence on temperature, which contradicts all the mechanisms described above. Such a dependence on temperature hints at the fact that thermal disorder actually enhances the MR, and a classical explanation rather than a quantum one appears to be more likely. As discussed in the context of Figure 4.2, CPP transport is intrinsically inhomogeneous due to the existence of low mobility interlayer regions (or potential barriers) in between the highly conductive VSe_2 layers. In such a situation it is possible to envisage the existence of distorted current paths misaligned with the out-of-plane driving electric field [77, 156, 157]. The magnetic field can then further deflect the charge carriers in the distorted paths, thereby increasing the resistance of the sample as a linear function of the magnetic field [77, 156, 157]. In this mechanism, the MR behavior is dictated by the *spatial mobility fluctuation* $\Delta\mu$, instead of the mobility μ itself. This is the basis of the classical linear MR model [77, 156, 157], and the temperature dependence observed in our study strongly suggests that *thermally aided mobility fluctuations* is the underlying mechanism. At higher temperatures increased phonon scattering randomizes carrier momentum, resulting in decreased mobility. On the other hand, a higher rate of phonon-assisted tunneling and hopping events through the interlayer states will try to enhance CPP mobility. These opposing mechanisms can enhance spatial mobility fluctuation at higher temperature, resulting in stronger MR. We also note that interlayer transport occurs between the Fermi levels of the neighboring layers. In the normal state, bands with different curvatures (and hence different effective masses and mobilities) cross the Fermi level, which can contribute to mobility fluctuation during CPP transport [37]. Below the CDW temperature, partial gaps open at the Fermi level for some of the bands, and those bands therefore stop contributing to the CPP current. This results in less inhomogeneity in the effective masses of the carriers and their mobilities. Also, below the CDW temperature, due to the above-mentioned partial gap openings, the metallic VSe_2 layers become comparatively more insulating in nature. Combined with the insulating nature of the interlayer barriers, they result in a more homogeneous system in terms of conductivity. Thus, partial gap openings below CDW temperature tend to reduce mobility fluctuations. Also, at lower temperatures, mobility fluctuations due to phonons are reduced. As a result, the MR tends to decrease with temperature, and eventually vanish below CDW temperature.

In case of CIP studies discussed above [72, 87], the linear MR that was observed below the CDW temperature, was attributed to mobility fluctuations caused by CDW formation. In the present case, for CPP transport, the origin of mobility fluctuation is fundamentally different, and results in a much larger effect for significantly smaller magnetic field values and close to room temperature. It is important to note that despite the sample dependent nature of mobility fluctuations, the occurrence of positive CPP MR and its magnitude is highly reproducible (Figure 4.2 and Figure 4.3).

To further investigate the linear nature of the observed MR and its connection with the classical linear model [77, 156, 157], in Figure 4.6(a) we plot MR as a function of B^2. *In the low field range*, MR vs B^2 is *linear* (zoomed in image shown in the inset), indicating a quadratic dependence of MR on B. However, *at higher field range*, MR vs B^2 becomes *sub-linear*, indicating the crossover of the MR vs. B response from quadratic to linear. The *inset* also shows that the slope of the linear segment in the low field range decreases with decreasing temperature. Defining the crossover magnetic field B_c to be the field value where the MR turns linear from quadratic, it becomes clear that B_c increases with decreasing temperature.

Figure 4.6(b) shows dR/dB as a function of the magnetic field. As discussed before, the response is primarily two-valued, indicating linearity of MR vs B. In the vicinity of zero magnetic field, dR/dB is linear, indicating quadratic dependence of MR on B. The crossover field B_c is the field value where the 'knee' of the dR/dB curve occurs, as shown in the inset of Figure 4.6(b). Clearly, the B_c values calculated in Figure 4.6(a) and (b) match closely, and it increases with decreasing temperature. Figure 4.6(c) shows the dependence of MR (over ±12 kG) as a function of the crossover field B_c, as the temperature is varied. As discussed earlier, larger MR occurs at higher temperatures, which also corresponds to smaller B_c values. As temperature is reduced, MR decreases but B_c increases.

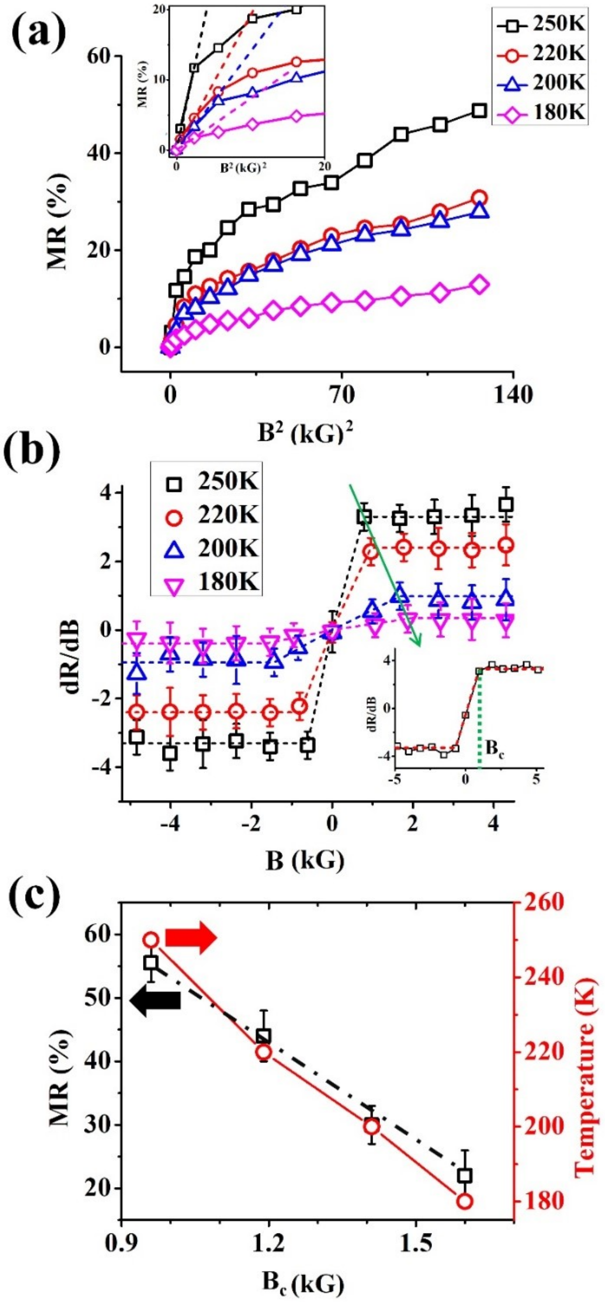

Figure 4.6: Analysis of the MR response shown in Figure 4.3 **(a)** MR vs B^2, showing linear fit at low field range (inset) and sub-linear behavior at high field range. **(b)** dR/dB vs B and calculation of the crossover field B_c (green dashed line in the inset). The green arrow in the main image shows that B_c increases with decreasing temperature. **(c)** Inverse dependence of MR on B_c. As temperature increases, B_c decreases.

According to the theory of classical linear MR [77, 156, 157], in the limit $\Delta\mu/\langle\mu\rangle<1$ (where $\langle\mu\rangle$ represents average mobility and $\Delta\mu$ is the width of the mobility disorder), MR $\propto \langle\mu\rangle$, in the large field limit $B_c \propto (\mu)^{-1}$. In the opposite limit, i.e. when $\Delta\mu/\langle\mu\rangle >1$, MR $\propto \Delta\mu$ and $B_c \propto (\Delta\mu)^{-1}$. Thus, in both cases, *MR is inversely related to B_c*, which is clearly matching with Figure 4.6(c), indicating that the classical linear MR mechanism is indeed operative in the present case.

Figure 4.7(a) shows the dependence of CPP MR on sample thickness. The MR effect becomes *weaker* as the thickness increases. This is in stark contrast with the CIP studies [72, 87], where CIP MR increases with increasing thickness. In the case of CIP, this was explained based on the hypothesis that formation of the CDW state is favored in thicker samples due to enhanced 3D interlayer coupling, which in turn increases CIP MR [72, 87]. Dependence of CDW with thickness, however, remains controversial [72, 87, 90, 94, 142, 158, 159].

In the case of CPP MR, lower thickness with the same bias means larger out-of-plane electric field on the VSe_2 layers. On one hand, larger electric fields can cause more momentum scattering and try to reduce mobility. On the other hand, larger electric fields can also bend inter-site potential barriers and facilitate inter-site tunneling or hopping, thereby enhancing mobility. As a result, carriers can experience enhanced spatial mobility fluctuations in thinner samples, resulting in stronger CPP MR, as shown in Figure 4.7(a). Figure 4.7(b) shows CPP MR as a function of temperature for different thicknesses. In all cases CPP MR decreases with decreasing temperature and vanishes at ~110K (CDW temperature), confirming that the MR response originates from the bulk of the samples, instead of the interfaces. As shown in Figure 4.7(c), the CPP MR remains a linear function of the magnetic field at all thicknesses.

Further analysis of the linearity of MR is shown in Figure 4.8 (a) and (b), which shows the existence of a crossover field B_c, above which the MR becomes linear from quadratic. The calculated B_c values have an inverse dependence on the corresponding MR (Figure 4.8 (c)), which confirms the applicability of the thermally aided mobility fluctuation model discussed above.

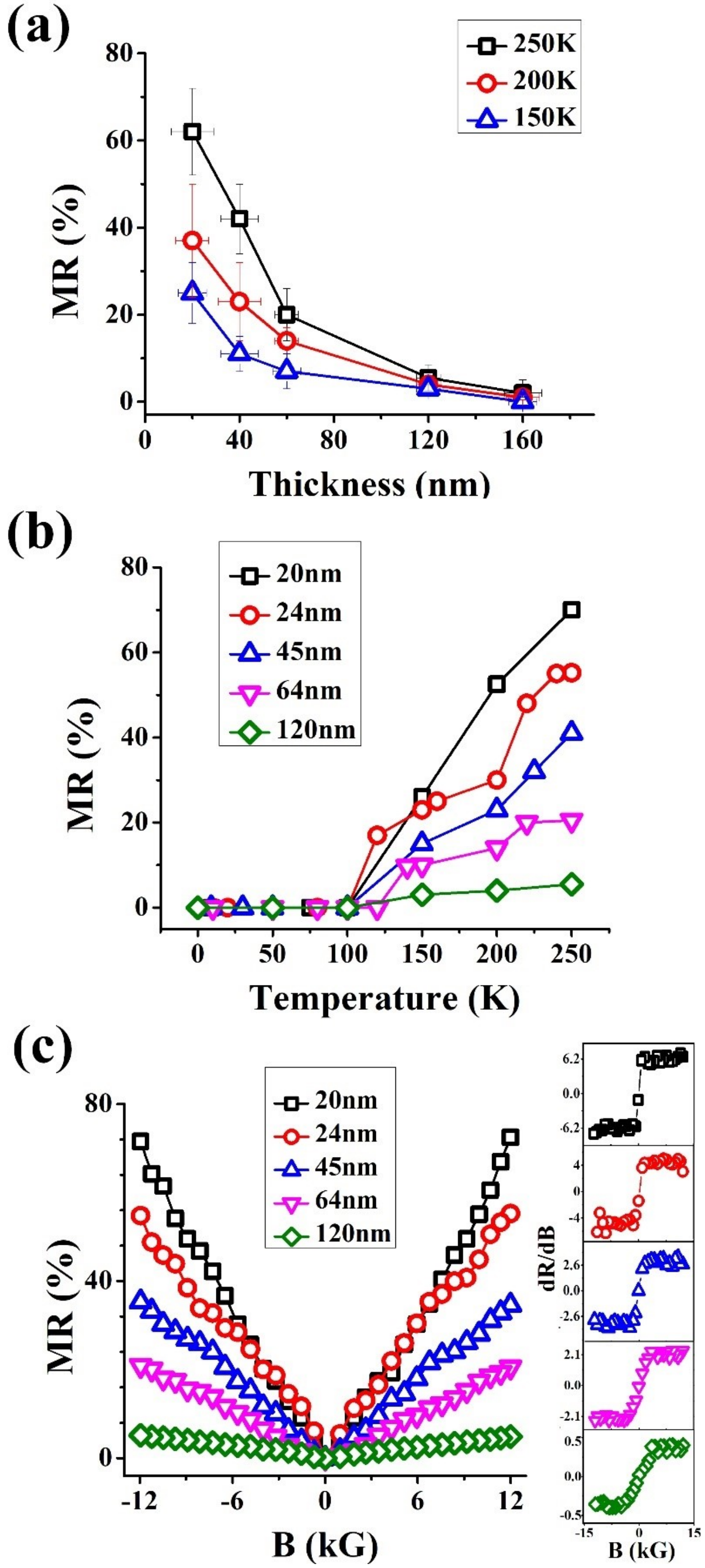

Figure 4.7: (a) CPP MR as a function of VSe_2 flake thickness at various temperatures. **(b)** CPP MR as a function of temperature for various thicknesses. **(c)** Linear magnetic field dependence of CPP MR for different sample thicknesses, measured at 250K. Here MR (B) = [R(B)–R(0)]/R(0) × 100%.

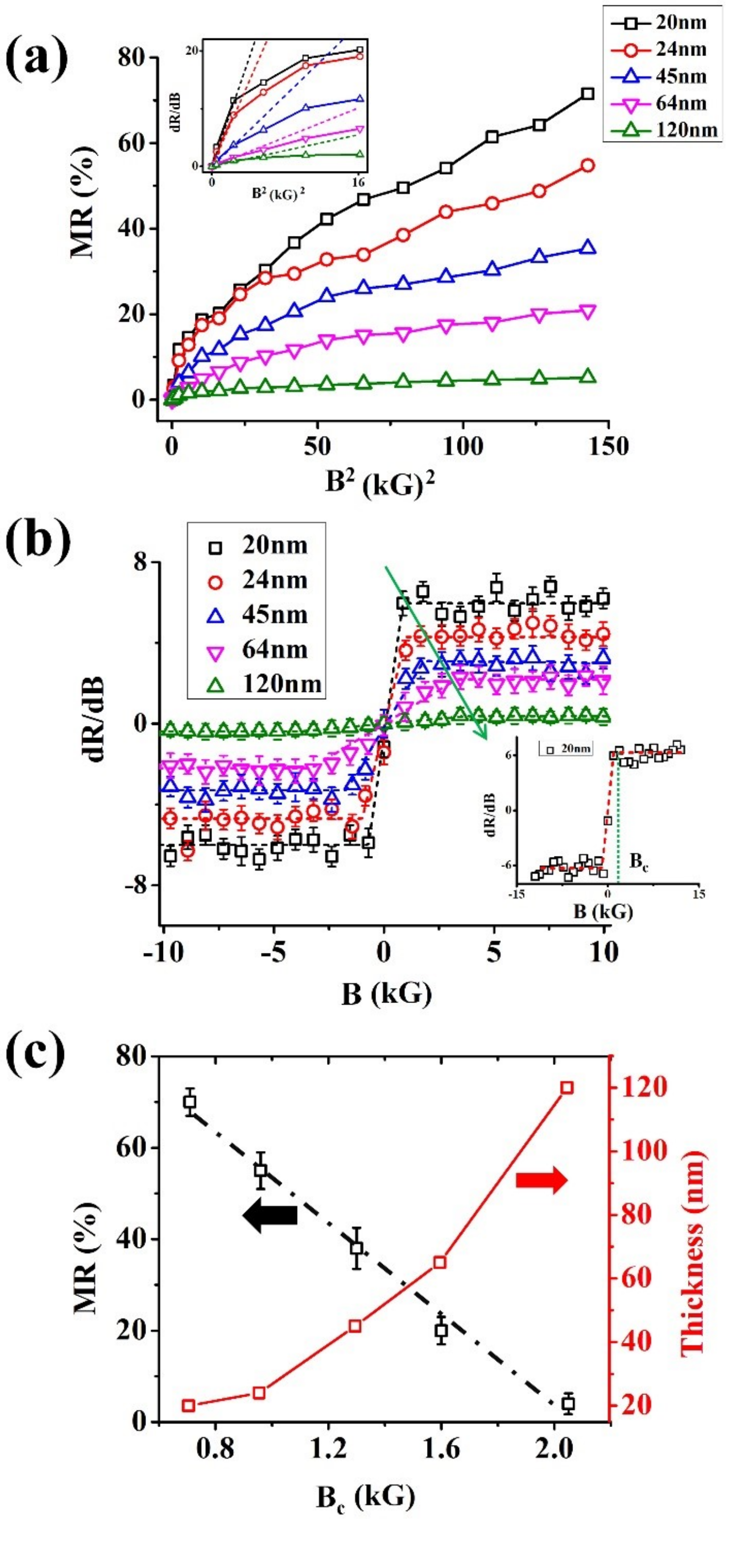

Figure 4.8: Analysis of the MR response shown in Figure 4.7. **(a)** MR vs B^2, showing linear fit at low field range (inset) and sub-linear behavior at high field range. **(b)** dR/dB vs. B and calculation of the crossover field B_c (green dashed line in the inset). The green arrow in the main image shows that B_c increases with increasing thickness. **(c)** Inverse dependence of MR on B_c. As thickness increases, B_c increases.

4.3 Summary and conclusion

In this chapter, we have presented CPP MR results from ultrathin flakes of 1T-VSe_2. Large, linear MR effect is observed close to room temperature (significantly beyond the CDW temperature), and in the low field range, which makes it a robust material platform for 2D based magnetic sensors. Unlike conventional MR effects, thermal fluctuation has been found to *enhance* the observed MR. The MR effect originates due to mobility inhomogeneity in the carrier transport path. In the case of VSe_2, in-plane conduction is metallic. Due to large interlayer distance, out-of-plane conduction is semiconducting. As a result, the net CPP transport is *inhomogeneous* and contributes to the MR effect. Other 2D materials and vdW heterostructures, which offer such dissimilar transport properties along in-plane and out-of-plane directions can in principle exhibit such high MR response as well. As a result, it may be possible to harness this naturally occurring property and observe similar MR responses in a broad family of 2D materials. In addition, it may also be possible to tune mobility fluctuations by judicious intercalation of vdW materials, thereby further enhancing room temperature MR effect. Since this effect does not rely on magnetic properties of the layers, unlike other 2D magnetic materials it is not limited by the Curie temperature. In Appendix A we outline possible future works based on VSe2.

Chapter 5: Chirality-induced Spin Selectivity in Functionalized Carbon Nanotube Networks: The Role of Spin-orbit Coupling

5.1 Introduction

As discussed before, another aspect of this thesis is exploration of chirality-induced spin selectivity (CISS) effect [8] in the context of 1D and 2D materials. The CISS phenomenon has recently attracted significant global attention, due to its potential implications in various fields such as spintronics, optoelectronics, enantioseparation, and spin-selective electrochemical and biological processes[100, 101]. The key observation underpinning the CISS effect is that chiral structures of organic molecules, whose mirror images are non-superimposable, exhibit a preference for transmitting a particular spin orientation (up or down) [100, 101]. This phenomenon can potentially be exploited to realize efficient non-magnetic, molecular-scale spin filters. These filters are critical not only for the miniaturization of spintronic devices but also because they may enable novel device designs to control spins for various quantum technologies. [100, 160]. For example, if 2D TMD materials, such as graphene or 1T-VSe_2, could be combined with chiral organic molecules, or if the 2D layers can be stacked on top of each other where the top layer is slightly rotated clockwise or anticlockwise relative to the bottom layer, new phenomena and new physics can potentially emerge. Therefore, a comprehensive investigation of the CISS effect using these hybrid platforms is necessary, which serves as the motivation for our CISS work. In this chapter we present our CISS results obtained from chiral 1D systems. In the next chapter we will present CISS results obtained from chiral 2D systems.

CNTs functionalized using chiral molecules typically show the CISS effect as discussed earlier in Chapter 2. However, the theoretical understanding of CISS in this hybrid platform continues to remain an open problem [100]. Three necessary ingredients for the observation of CISS have been identified, such as (a) spin-orbit coupling, (b) structural inversion asymmetry (introduced by medium chirality) and (c) time reversal asymmetry (typically introduced by magnetic field in magnetotransport experiments). Recently, Liu, Yizhou, et. al. [161], suggested that the spin-orbit coupling of the metal electrode is more important than that of the chiral media. In this model, one can ignore the spin- orbit coupling of the chiral medium, and treat it as a polarizer of carrier orbital angular momentum. The spin-orbit coupling in the electrodes converts the orbital polarization to spin polarization, thereby resulting in CISS effect. This mechanism gives rise to an electromagnetochiral (EMCh) response, with resistance of the form $R(B,I) = R_0 – R^{\chi} B.I$, where R_0 is ordinary resistance, R^{χ} is the chirality dependent resistance, B is the magnetic field, and I represents current [162]. Recently, it has been suggested that such EMCh effect could give rise to the CISS effect by modulating the tunnel barrier between the contacts in CISS experiments [163].

To examine these issues, we have recently studied the CISS effect in chiral functionalized planar CNT networks using a transverse configuration in which the applied magnetic field is perpendicular to the current paths [164]. The tell-tale signs of the CISS effect have still been observed, indicating non-zero spin components transverse to the current direction [164]. It is important to note that in this transverse configuration, the EMCh contribution is zero (since $B \cdot I = 0$); hence, the observed response can be considered a pure CISS signal, devoid of any other spurious chiral effects. The next question is: *does the spin–orbit coupling of the CNTs contribute to this pure CISS signal?* Although graphene, the parent material of CNTs, has very weak spin–orbit coupling due to the low atomic number of elemental carbon, CNTs, on the other hand, show strong spin–orbit coupling due to orbital mixing induced by curvature [165-167]. For example, intrinsic spin–orbit effects in graphene are expected to appear at an energy scale of ∼1 μeV, whereas in the case of SWCNTs (single wall CNTs), they are ∼100 μeV–1 meV [166-168]. Curvature induced spin–orbit coupling in CNTs typically has the following form: $a \sim \gamma a \Delta_A^{SOC}/R$, where γ is a parameter that can range between 0.01 and 1, a is the nearest neighbor carbon–carbon distance, Δ_A^{SOC} is the atomic spin–orbit interaction of carbon, and R is the nanotube radius [129]. Thus, CNT radius is an experimental handle that allows tuning of the spin–orbit interaction and could affect the CISS signal. Double wall (DW) and multi wall (MW) tubes typically have larger diameters; therefore, they could be used for this investigation. Therefore, we examine the role of nanotube spin-orbit coupling on the observed pure CISS signal by systematically varying nanotube diameter. We find that the magnitude of the CISS signal scales proportionately with the spin-orbit coupling strength of the nanotubes. We also find that nanotube diameter dictates the supramolecular chirality of the medium, which in turn determines the sign of the CISS signal.

5.2 Results and discussions

To test the above hypothesis, we studied planar CNT networks functionalized with Fmoc-diphenylalanine (or, Fmoc-FF) + glucono-δ-lactone (GdL). The molecular structures of these chiral moieties are shown in Figure 5.1 (a). We considered single wall (SW), double wall (DW) and multi wall (MW) tubes, with multi wall tubes having higher than two shells. A typical cross-sectional image of these tubes is schematically shown in Figure 5.2(a), with SW-, DW- and MWCNTs having *average* diameters of ~0.82 nm, ~0.9 nm, and ~9.5 nm respectively, as specified by the vendor.

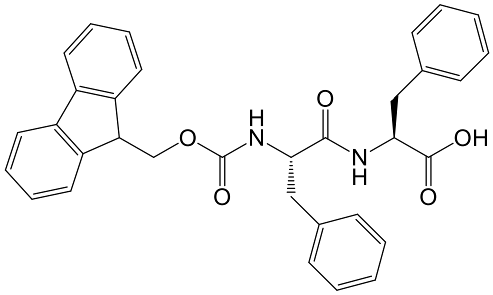

Fmoc-FF (L)

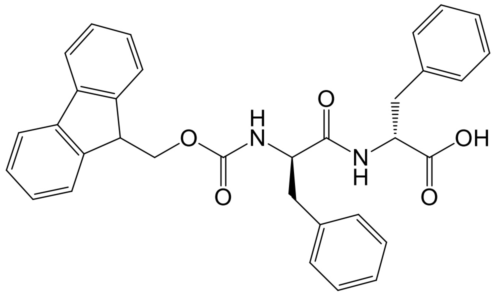

Fmoc-FF (D)

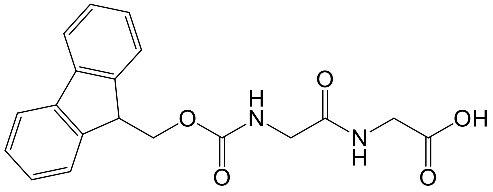

Fmoc-GG

Figure 5.1: Molecular structures of Fmoc-FF (L), Fmoc-FF (D) and Fmoc-GG.

Diameters of SW- and DW-CNTs have been confirmed independently by us from the Raman radial breathing mode (RBM) of the *raw* tubes. Using RBM frequency ω_{RBM}, we used the following formula to estimate the diameter d_t of the raw CNTs, [100]: $\omega_{\mathrm{RBM}} = A/d_t + B$ where A and B have values of ~234 nm.cm^{-1}, and ~10 cm^{-1} for SWCNTs. For DWCNTs, parameter B is zero. Using $\omega_{\mathrm{RBM}} \sim 260–330$ cm^{-1} for SWCNTs from Figure 5.2(b), we obtain SWCNT diameter $d_t \sim 0.73 – 0.92$ nm, resulting in an average SWCNT diameter of ~ 0.82 nm, which also matches closely with vendor specification. Using $\omega_{\mathrm{RBM}} \sim 260$ cm^{-1} for DWCNTs from Figure 5.2(d), we obtain DWCNT diameter $d_t \sim 0.9$ nm. However, presence of larger diameter DW tubes is possible, which are not detected in the RBM scan above.

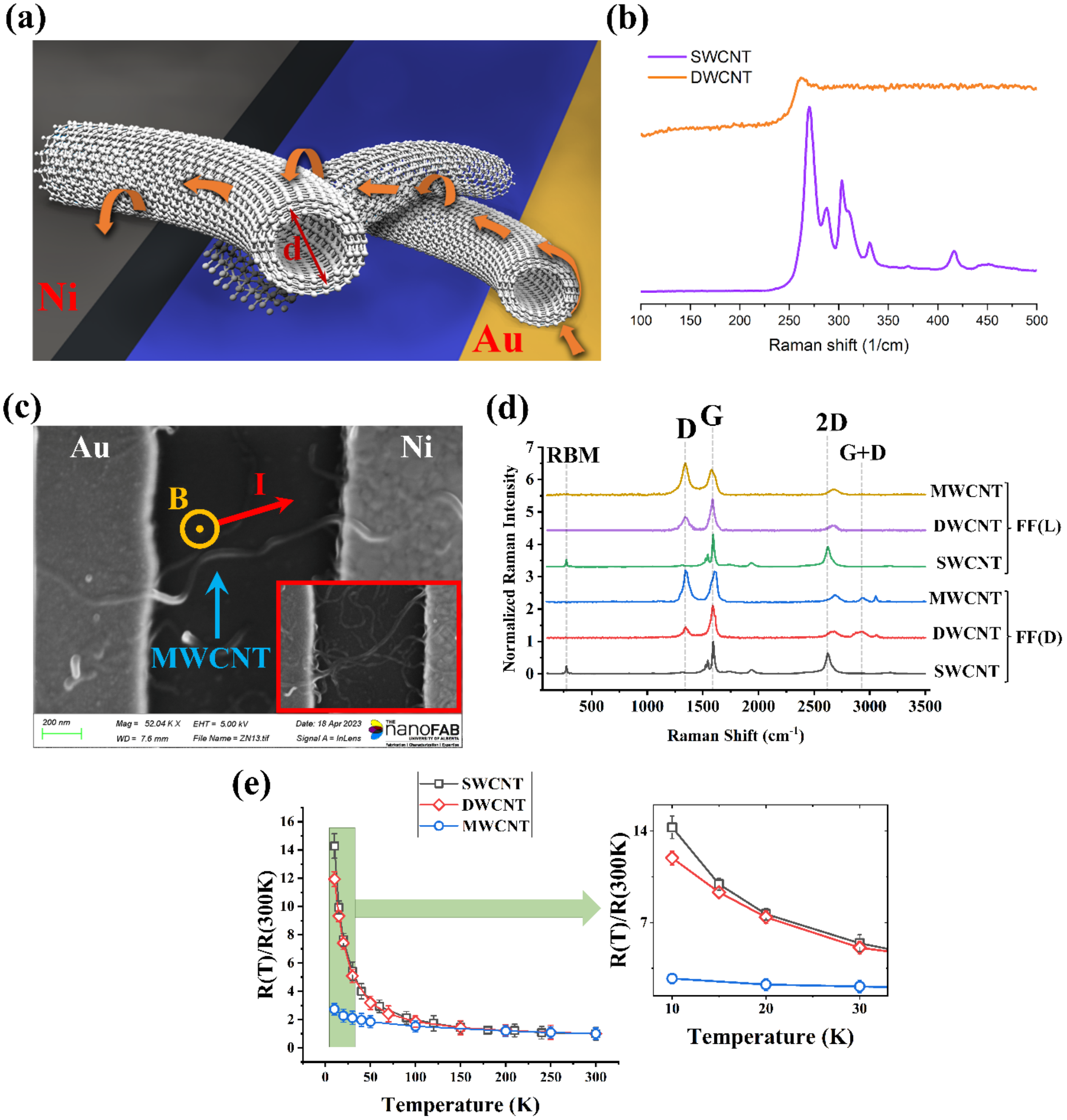

Figure 5.2: (a) Schematic diagram of Fmoc-FF, GdL, and MWCNT, showing the *average* tube diameter. **(b)** Raman RBM mode of raw SWCNTs and raw DWCNTs, taken at 532 nm laser. Raw MWCNTs did not show any detectable RBM signal. **(c)** Scanning Electron Microscopic (SEM) image of the device. *Main image* shows a single MWCNT, contacted by an Au-Ni electrode pair. *Inset* shows a network of MWCNTs. Magnetic field B is perpendicular to the average direction of current (I) flow, which lies in the sample plane. **(d)** Raman characterization of the functionalized tubes, taken at 532 nm, showing the signature peaks. **(e)** Typical temperature-dependent resistance of the functionalized tubes.

The diameter of MWCNTs can also be estimated from a Scanning Electron Microscopic (SEM) image as shown in Figure 5.2(c), although it's important to note that these tubes are attached with molecules, so they tend to exhibit larger diameters.

Synthesis of functionalized CNT networks has been reported before [104, 135, 164], and is performed by our collaborator's group (led by Dr. Luis Álvarez de Cienfuegos, Universidad de Granada) in Spain. In this method, a CNT suspension is created in a basic aqueous solution of Fmoc-FF via sonication. To prepare the basic aqueous peptide solution, Fmoc-L-FF and Fmoc-D-FF peptides were weighed separately into vials and deionized water was added to obtain a final concentration of 10 mM. The suspension sonicated for 1 hour. Then, a NaOH solution (0.5 M) was added dropwise until a clear solution (pH=10.7) was obtained. To prepare composite solution of peptides with carbon nanotubes, 0.7 mg of each CNT were weighed separately into a vial tube. The carbon nanotubes were suspended in 1 mL of the basic aqueous peptide solution. The suspension was sonicated for 2.5 h in a cold ultrasonic bath and then centrifuged for 5 min at 10.000 rpm. After collecting the supernatant, GdL is added, which lowers the pH, resulting in the collapse of the peptide molecules and formation of a three-dimensional peptide hydrogel network, encapsulating the CNTs. The network formation takes place via π-π interaction and hydrogen bonding between the peptide molecules as well as between the peptide molecules and CNT sidewalls [169]. Since the FF side chain is chiral, its interaction with the CNTs is expected to induce chirality dependent effects in magnetotransport measurements.

Device fabrication and CISS studies using these samples have been performed by our group. For the fabrication of the device, a slice of the gel is placed between Ni-Au contact pairs fabricated on SiO_2/Si. The Ni contact is protected by a photoresist layer to prevent oxidation, which is only removed immediately before placing the gel. The Au and Ni contacts are made significantly large in dimension to minimize the contact resistance contributions in the two-terminal CISS measurements. Finally, the sample is annealed, which results in a xerogel structure contacted by Ni-Au. The device made in this procedure remains electrically stable for at least several weeks. An SEM image of the final device structure is shown in Figure 5.2(c).

Figure 5.2(d) shows the Raman spectra of the *functionalized* CNTs. The *G* band appears in all samples, typically at ~1580–1600 cm^{-1}, and is due to the longitudinal vibrations of the carbon atoms in the graphitic lattice. A weak shoulder peak is also observed in the *G* band, which is due to the tangential vibrations of the carbon atoms. The presence of a strong *G* peak in all cases indicates that the underlying graphitic lattice is mostly unaffected even after functionalization.

All samples show a defect (*D*) peak around ~1350 cm^{-1}, which typically manifests after the sonication step due to the broken ends of the tubes. Thus, MWCNTs naturally have a stronger *D* band, which is consistent with past studies [170, 171]. The *G′* (or, 2*D*) band is observed around ~2680 cm^{-1}. In some cases small peaks are observed at ~2930 cm^{-1}, which is attributed to the *G*+*D* peak [171].

Low energy radial breathing modes (RBM) are absent in *functionalized* DW- and MWCNTs. This is due to the fact that the RBM frequency depends inversely on tube diameter and the large diameter of these tubes makes the detection of RBM difficult. Also, the attached molecules may cause suppression of radial vibration. However, RBM peaks are present in *functionalized* SWCNTs in the range of 260–280 cm^{-1}.

Figure 5.2(e) shows temperature-dependent resistance (R vs. T) of functionalized SW-, DW- and MWCNT samples in the range 10K–300K. In all cases we observe negative temperature coefficient of resistance *i.e.* the resistance decreases with increasing temperature ($\mathrm{d}R/\mathrm{d}T < 0$), which is consistent with earlier work on CNT networks [172-176]. Such behavior is generally explained by a “heterogeneous transport” model [177]. In a CNT network like ours, there exist potential barriers due to tube defects and inter-tube crossings, which will localize charge carriers in the nanotube segments. Carrier transport occurs via transport inside each nanotube segment coupled with phonon-assisted tunneling or hopping from one segment to another [schematically shown in Figure 5.2(a).

Narrower tubes (SW and DW) have larger band gaps compared to the MW tubes, resulting in a more semiconducting type of behavior inside the tube segments. Thus, the overall resistance of the SW- and DW- tubes is more sensitive to temperature compared to the MW tubes, as shown in Figure 5.2(e). Multiple samples (∼10) of each tube type have been tested, and each sample has been scanned multiple times. The error bars from these measurements are shown in Fig. 4.2(d), which shows that the R(T)/R(300 K) response is remarkably consistent. It is to be noted that, in our case, the nanotube walls are attached with chiral molecules; hence, the carriers in the nanotubes will experience a chiral potential and spin–orbit interaction of the nanotube.

For the magnetoresistance (MR) measurements we choose a *transverse* configuration, in which the magnetic field, and hence Ni magnetization is *perpendicular* to the sample plane and hence *perpendicular* to any in-plane current path (Figure 5.2(c)). Most studies in CISS employ a longitudinal configuration, in which the magnetic field is collinear with the current, and a spin component collinear to the current is detected [100]. However, signals from such geometry may have a contribution from the EMCh effect due to the non-zero $B.I$ term as discussed above. The transverse geometry chosen here tunes out any such contributions.

Earlier work from our group has shown that even in this transverse configuration a clear CISS signal can be observed, which indicates the presence of a spin component transverse to the direction of the current [164]. Such transverse CISS signals can be viewed as a *pure* CISS signal, devoid of any artifacts arising from the EMCh effect.

The MR effect in CNT networks, consisting of both SW- and MWCNTs, has been reported by multiple groups [172-175, 178-181]. In all cases, negative MR is observed in a transverse geometry *i.e.* resistance R decreases with increasing magnetic field (B) strength, at low temperatures and low magnetic fields. The negative MR is often attributed to quantum interference induced localization effects, and is *symmetric* relative to the magnetic field, i.e. $R\,(+B) = R\,(-B)$. In our experiments, the CNT network is functionalized with chiral molecules, and they are contacted with one magnetic (Ni) and one non-magnetic (Au) electrode. As shown in Figures 5.3(a), (c), (e), we also observe a low temperature, low field negative MR for SW-, DW- and MWCNTs respectively.

The key difference is that the MR is no longer symmetric relative to B, i.e. $R\,(+B) \neq R\,(-B)$, and this *asymmetry* (or, the "tilting") of the MR curves is dependent on the chirality of the functionalized CNT network, as shown clearly in the *insets* of Figures 5.3(a), (c), (e). As shown in our earlier work, if achiral molecules are used, the MR response regains its symmetry [135]. According to the standard CISS picture, chiral medium polarizes electron spin, which experiences different transmission probabilities through the Ni electrode depending on its magnetization, resulting in an asymmetric $R(B)$ response.

To isolate the asymmetric component due to the CISS effect, we plot the asymmetric and symmetric components of the MR response in Figures 5.3(b), (d), (f), computed as $R^{Sym/Asym} = [R(B) \pm R(-B)]/2$. It is clear that the asymmetric component is chirality dependent. The *magnitudes* of the symmetric and the asymmetric components are computed as $\delta^{Sym} = R^{Sym}(0) - R^{Sym}(\pm 10kG)$ and $\delta^{Asym} = |R^{Asym}(+10kG) - R^{Asym}(-10kG)|$, and the normalized signal is computed as $\delta^{Asym}/\delta^{Sym}$ x 100%.

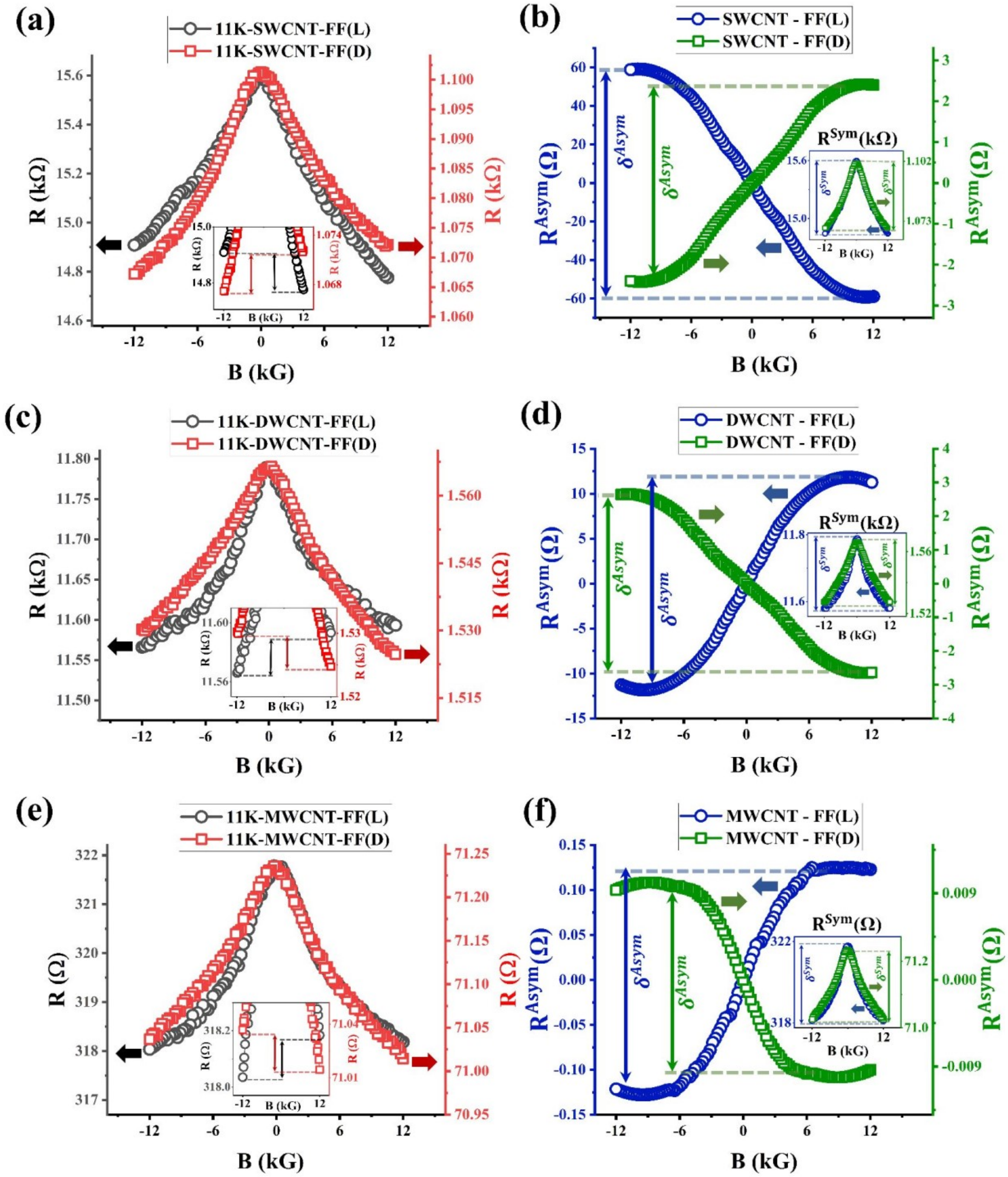

Figure 5.3: (a), (c), and **(e)** Chirality-dependent MR effects in SWCNT, DWCNT and MWCNT networks respectively. **(b), (d),** and **(f)** Asymmetric (*main image*) and symmetric (*inset*) components of the MR responses. Resistance values are measured at 0.5 V.

Figure 5.4(a) shows the $\delta^{Asym}/\delta^{Sym}$ ratio for SW-, DW- and MWCNTs. Clearly the CISS-induced asymmetry of the MR signals decreases with increasing number of walls (or, *average* tube diameter). Multiple (~10) samples have been tested for each type of CNT, and the trend in Figure 5.4(a) is always observed – i.e. MWCNT signals are always weaker than that of SWCNTs, while DWCNTs typically show an intermediate signal strength. In literature, the CISS signal is often computed as $\delta^{CISS} = [R(-10kG) - R(+10kG)]/min[R(\pm 10kG)]x\ 100\%$, [100], and $|\delta^{CISS}|$ is plotted in Figure 5.4(b). Clearly, $|\delta^{CISS}|$ for MWCNTs is weaker by an *order of magnitude* compared to that of SWCNTs and DWCNTs.

MWCNTs consist of multiple coaxial graphene cylinders of different diameters. In most experiments, including ours, the MWCNTs are contacted by bulk metallic pads, which form electrical contact only with the outermost shell, and hence current is injected in the outermost graphene cylinder. Combined with the weak coupling between the shells, which prohibits inter-shell electron hopping at low temperatures, earlier experiments have reported that current flows primarily through the outermost shell [182, 183]. The presence of defects in the CNT walls can however cause inter-shell hopping. To account for this effect, mean diameter of the DW- and MWCNTs should be considered, which are estimated to be ~ 0.9 nm and ~ 9.5 nm respectively, as discussed before. Clearly, there exists an order of magnitude difference in the diameters between SW-/DWCNTs (~ 0.82 nm and ~ 0.9 nm respectively) and MWCNTs (~ 9.5 nm), which should result in an order of magnitude reduction of the spin-orbit coupling strength of MWCNTs compared to SW-/DWCNTs. This is expected to result in a concomitant order of magnitude reduction in the CISS signal for MWCNTs, which we indeed observe in Figure 5.4(b).

Comparing $|\delta^{CISS}|$ of SWCNTs and DWCNTs, they differ by a factor of ~2.2, whereas their diameters differ by a factor of ~ 1.1, which are relatively close values and within the same order of magnitude. Therefore, the systematic reduction of the CISS signal with nanotube radius, as observed in Figure 5.4(b), can be attributed to the gradual reduction of the CNT spin-orbit coupling with increasing radius. Figure 5.4(c) shows the $\delta^{Asym}/\delta^{Sym}$ ratio for SW-, DW- and MWCNTs at different temperatures. A monotonic decreasing trend is observed, which has been observed before in CNT-based systems, [104, 135, 164], presumably due to increased spin relaxation in CNTs at higher temperatures [184]. At all temperatures SWCNT signal is the strongest, MWCNT is the weakest and DWCNT has an intermediate value. This is consistent from sample-to-sample, as indicated by the error bars. We also note that the CISS signal manifests in the 10–30 K range, which corresponds to an energy scale of 0.86–2.58 meV. This matches the ∼1meV spin–orbit energy scale of CNTs discussed above.

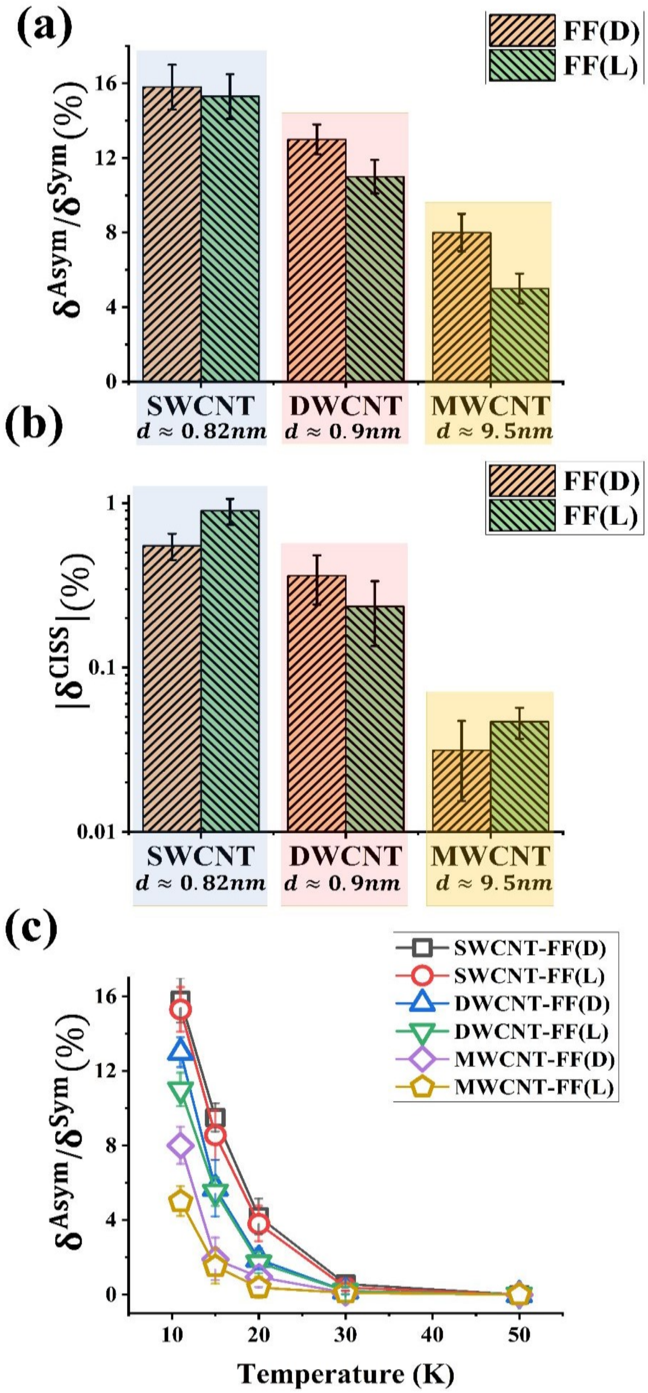

Figure 5.4: (a) CISS-induced asymmetry of the MR curves as a function of tube diameter. **(b)** CISS signal as a function of tube diameter. **(c)** MR asymmetry as a function of temperature for SW-, DW- and MWCNTs.

In CNTs, bandgap depends inversely on diameter, and the larger-diameter multiwall tubes tend to be metallic. This explains why the MWCNT resistance is much smaller than the SW/DW- CNT resistance values, as shown in Figure 5.3. This metallic behavior of MWCNTs is also shown in Figure 5.2(e), where it shows much weaker temperature dependence compared to SW/DW-CNTs. The trends reported above are based on normalized quantities such as $\delta^{Asym}/\delta^{Sym}$ and δ^{CISS}, and not on specific resistance values. Furthermore, we have shown data from multiple samples (~10), and each sample has been tested multiple times. The error bars are indicated in our data. Our conclusions are based on the overall statistical trend and not on any specific device. Thus, we believe that device-to-device variation has already been factored into our conclusions.

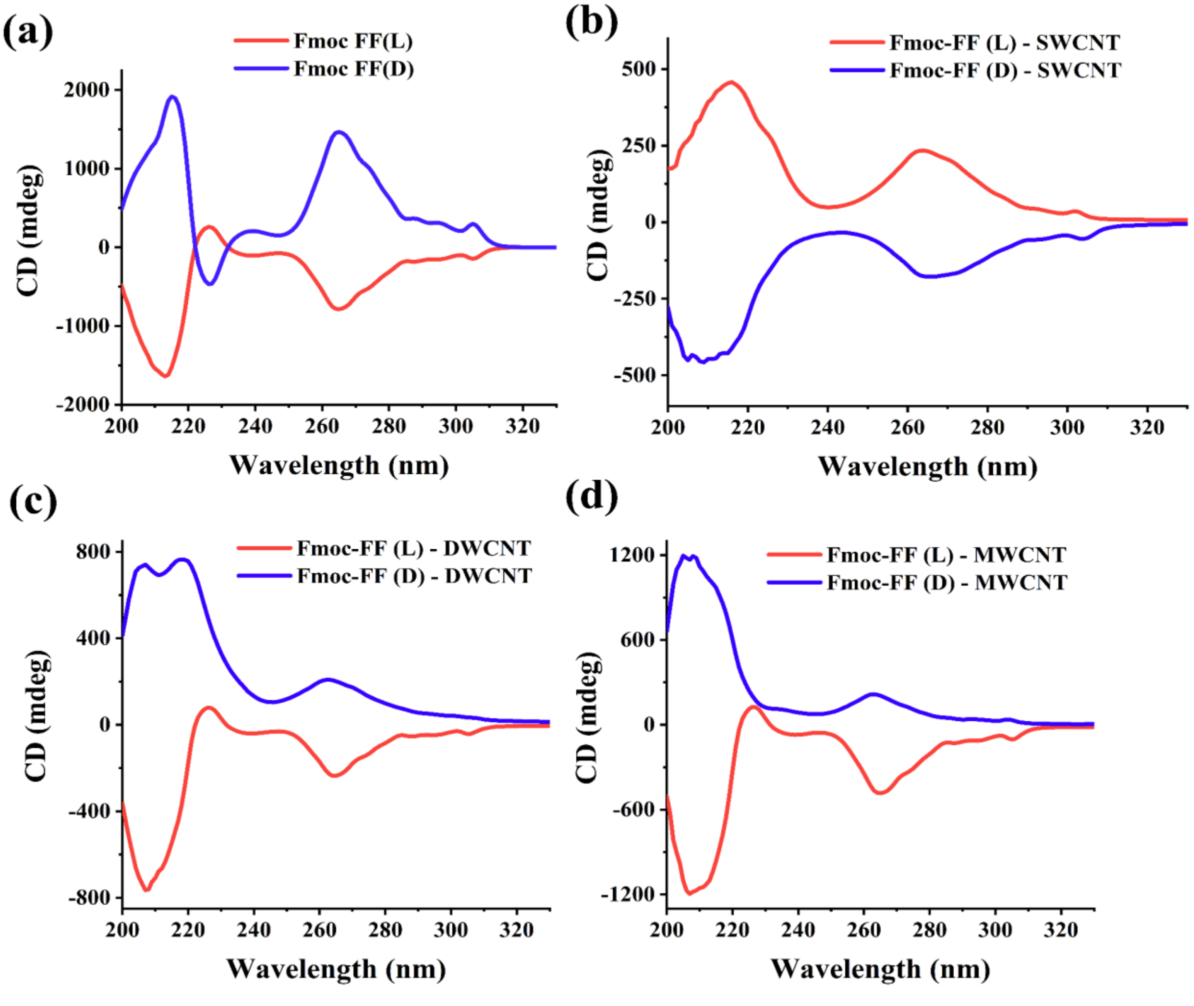

Figure 5.5: (a) CD spectra of the Fmoc-FF peptide solutions. **(b)** CD spectra of Fmoc-FF–SWCNT suspensions. **(c)** CD spectra of Fmoc-FF–DWCNT suspensions and **(d)** CD spectra of Fmoc-FF–MWCNT suspensions. In all measurements the peptide concentration was 5 mM and CNT concentration was 0.35%. Red color corresponds to the Fmoc-FF (L) derivative and blue color corresponds to the Fmoc-FF (D) derivative. CD spectra have been normalized for comparative purposes.

A curious feature of the MR responses is that the SWCNT samples exhibit *opposite* chirality dependent behavior compared to the DW and MW samples, as seen from Figures 5.2(b), (d), (f). To understand this, we investigate the circular dichroism (CD) response of the *diluted* CNT samples (Figure 5.5; for CD spectra Figure 5.6; for HT spectra), which suggests that an inversion of the supramolecular chirality of the peptide fibers is taking place mediated by the type of nanotube. This effect is well-known in literature, as supramolecular interactions are non-covalent and can be affected by several internal and external stimuli such as chiral or achiral molecules, different additives, and changes in the pH of the media, solvent composition or by the application of heat, light or sonication [185-187]. Recently, it has been shown that supramolecular chirality can be inverted by the size of Au NPs (nanoparticles) through the interaction of the organic molecules with the different curvatures of the NPs [188]. Presumably, a similar effect is occurring here, as different CNT samples have a different radius and hence different curvature.

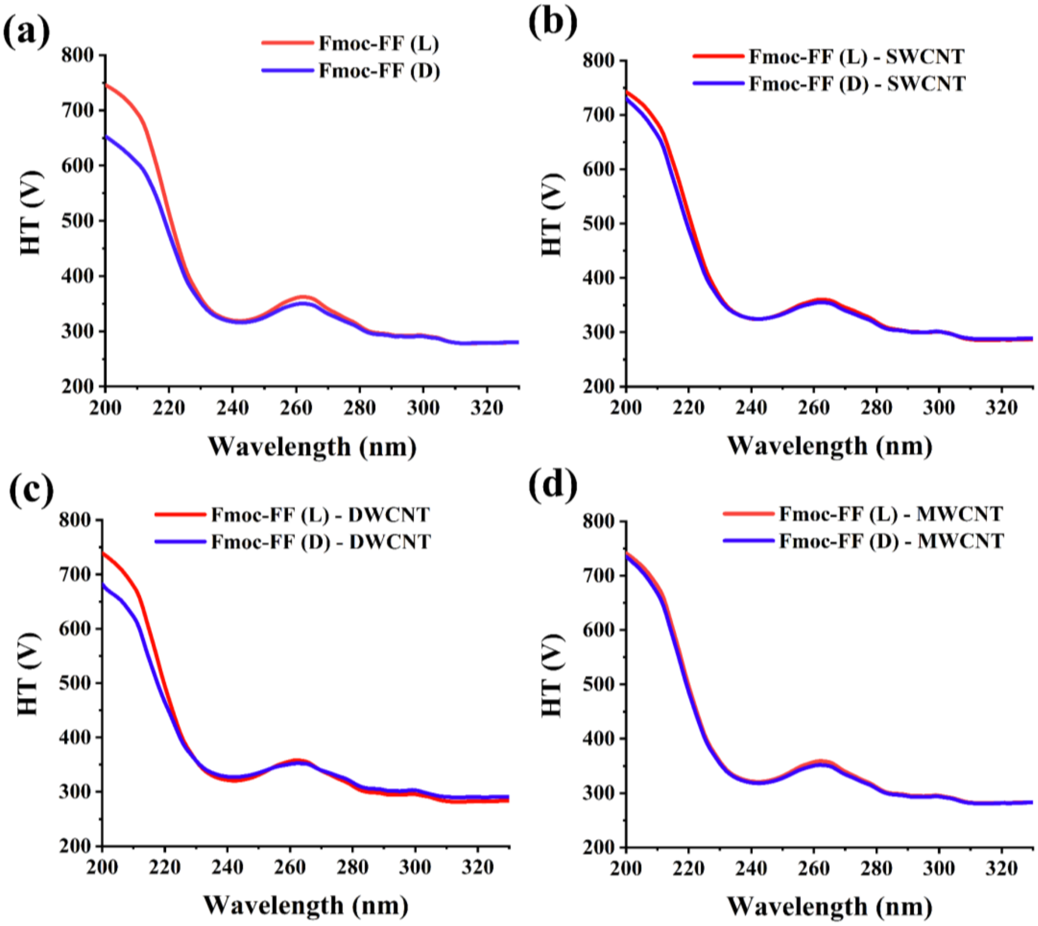

Figure 5.6: HT spectra of **(a)** Fmoc-FF solutions (5 mM) and **(b)–(d)** Fmoc-FF (5 mM) + CNT (0.35%) solutions.

Figure 5.5(a) shows the usual supramolecular arrangement of these type of peptides corresponding to a β-sheet and characterized by the presence of two peaks: one at ~270 nm (π - π* transition of the fluorenyl groups) and the other more intense peak at ~220 nm (π - π* transition of the amino acids) [189]. The CD spectra of the Fmoc-FF (L) derivative (red color) showed negative values while the D derivative (blue color) showed positive values. Figure 5.5(b) shows the CD spectra of the peptide solutions (Fmoc-FF) at the same concentration but now interacting with a suspension of SWCNT (0.35%). In this case, the interaction with the SW tubes produced an inversion of the supramolecular chirality of the peptides, now showing positive values for the L derivative (red color) and negative values for the D derivative (blue color). Nevertheless, this inversion in the chirality was not observed for the other two samples containing DW- and MWCNT (Figures 5.5(c) and (d)). In these cases, the sign of the curves was the same as the initial Fmoc-FF peptide solutions of Figure 5.5(a). As such, the opposite CISS values of SWCNT samples with respect to DW- and MWCNTs (as observed in Figure 5.3) can be explained based on the opposite supramolecular chirality of the peptide-CNT samples.

5.3 Summary and conclusion

To summarize, the physical origin of CISS is often debated, in particular the role of spin-orbit interaction of the chiral medium, and the effect of other EMCh effects on CISS. In this study, we nullified the EMCh effect using a transverse geometry, but still observed the characteristic CISS signals. The strength of this *pure* CISS signal scales proportionately with the spin-orbit strength of the medium. Thus, CISS cannot be explained solely based on EMCh and spin-orbit coupling of the medium indeed plays a critical role. Spin-orbit coupling is generally considered to be a “double-edged sword" in spintronics, because on one hand it allows external electric field control of the spin orientations, but on the other hand, it can also cause spin dephasing. It appears that in CISS systems, spin signal actually increases with the spin-orbit coupling strength, which is different from conventional materials. The CISS signal is dictated by the supramolecular chirality of the medium, consistent with previous studies. Considering the inverse relationship between CNT diameter and the spin-orbit coupling strength, the CNTs can be viewed as graphene in the large diameter limit. Therefore, one should expect vanishing CISS effect in chiral functionalized graphene as well. We investigate this hypothesis in the next chapter and explore CISS effect in 2D system.

Chapter 6: Chirality-induced Spin Selectivity in Supramolecular Chirally Functionalized Graphene

6.1 Introduction

As discussed in the previous chapter, the CISS effect diminishes in CNTs, in the large diameter limit. Therefore, in the case of graphene, which is essentially a CNT with infinitely large diameter, the CISS effect is expected to vanish. This is because the spin-orbit coupling is much weaker in graphene compared to CNTs, due to the absence of the curvature effect. Despite the promising interest in chiral graphene hybrid materials for diverse applications such as catalysis and sensing, their CISS properties have not been investigated yet, which motivates our research in this area. Graphene, in its pristine form, is a particularly interesting 2D material because of its unique band structure, high carrier mobility and its ability to show various quantum transport phenomena even at room temperature [190, 191]. From the viewpoint of spintronics, room-temperature spin transport and micron scale spin relaxation length in pristine graphene layers have been reported [192, 193]. Such features originate due to weak intrinsic spin-orbit interaction of graphene and weak hyperfine interaction of electron spin with carbon nuclei, which suppress the spin relaxation mechanisms. On the other hand, it has been reported that various chiral organic molecules can impart chirality to various graphene derivatives such as graphene oxide (GO) and reduced (or, deoxygenated) graphene oxide (rGO) via covalent as well as non-covalent interactions including hydrophobic effect, π–π stacking, electrostatic effect etc. [194-201]. In most cases, chirality of the resultant hybrid materials originates from the chirality of the attached moiety. These have been classified in various categories such as “configurational chirality” (originating from small chiral molecules), “conformational chirality” (due to helical polymers) or “hierarchical chirality” (due to chiral liquid crystal structures) [197].

Reference [202] reported synthesis of chiral graphene quantum dots via functionalization with chiral cysteine molecules. The molecules attach with the edges of the graphene flakes and induce “structural chirality” in the form of helical buckling of the flakes. Several application areas of chiral graphene have been explored by the above studies, which include chiral catalysis [198], chiral separation and recognition [196, 199, 200], enantioselective sensing [195, 201] etc. Use of GO and rGO in these studies is motivated by the fact that they are amenable to chiral functionalization via chemical means, and chiral graphene can be generated in large quantities via solution processing, which are difficult to achieve using pristine graphene. While electrical conductivity of rGO is significantly lower than that of pristine graphene, it is still much more conductive than pure organics and commonly finds applications in field-effect transistors [203], chemical sensors [204] and conductive electrodes in various devices [205].

At the present stage, very little, if any, is known about the CISS properties of these chiral graphene materials. *A priori*, CISS effect is expected to be weak due to the weak spin-orbit interaction of graphene, even though rGO systems are structurally distinct from pristine graphene layers, due to the presence of defects in the form of carbon vacancies and adatoms such as hydrogen and oxygen. In any case, if the CISS effect exists in chiral rGO systems, it could potentially be used as a detection mechanism for the above chiral separation, recognition and sensing applications.

In this chapter we report the CISS effect in a thin graphene film, which consists of rGO flakes non-covalently functionalized with chiral supramolecular fibers made by the self-assembly of Fmoc-FF (L/D). Graphene is covered by the hydrophobic peptide fibers in which the aromatic rings of Fmoc-FF molecules bind efficiently with the planar surface of graphene via π-π interaction. Control experiments are performed with Fmoc-GG (Fmoc-diglycine) molecules, which are achiral. As described below, the chiral molecules self-assemble in helical supramolecular structures along with the attached graphene and induce the CISS effect in two-terminal magnetotransport measurements. The role of graphene flake thickness has been investigated by using single-layer graphene (SLG) and multi-layer graphene (MLG) flakes (both in rGO form).

6.2 Results and discussions

Synthesis of chiral functionalized graphene and its CD characterization has been performed by our collaborator's group (led by Dr. Luis Álvarez de Cienfuegos, Universidad de Granada) in Spain. Device fabrication, microscopic characterizations and electronic and magnetic measurements have been performed in our group.

Figure 6.1(a) shows the circular dichroism (CD) spectrum of the chiral (Fmoc-FF L/D) solutions. Figures 6.1(b), (c) show the CD spectra of the SLG and MLG solutions respectively, functionalized with Fmoc FF L/D molecules. Figure 6.1(d) shows the CD spectrum of the SLG and MLG solutions functionalized with achiral (Fmoc-GG) control molecules. Corresponding HT spectra are shown in Figure 6.2.

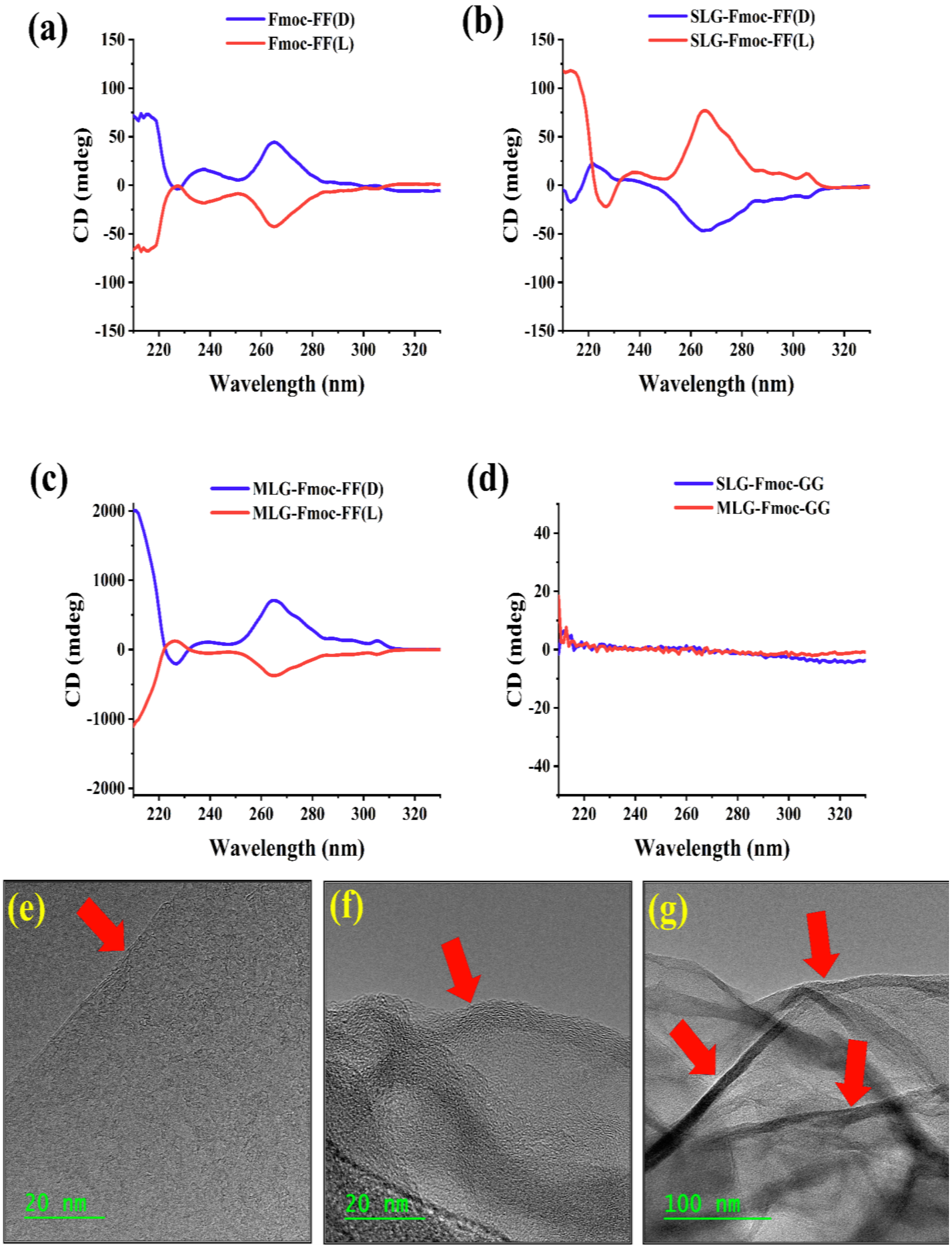

Figure 6.1: (a)-(d) CD characterizations of the Fmoc-FF and functionalized SLG and MLG solutions. **(e)** TEM image of a pristine (unfunctionalized) graphene flake. Arrow shows the straight edge of the flake. **(f), (g)** TEM images of functionalized flakes. The arrows show the curved flakes.

CD spectra of Fmoc-FF supramolecular fibers showed mirror images for both enantiomers indicating that the chirality of the supramolecular aggregates is dictated by the intrinsic chirality of the peptide. These aggregates show two characteristic Cotton bands, one around 220 nm which corresponds to n–π* transition of the amino acids and another band around 260–270 nm which corresponds to the π–π* transition of the fluorenyl groups and previously justified as superhelical arrangements of these peptides [189, 206, 207]. This band determines the supramolecular arrangement of these peptides and therefore is the one related to the CISS effect [104].

The self-assembly of Fmoc-FF in water is mainly mediated by hydrophobic interactions between peptides. This process can be triggered by different stimuli, and once the self-assembly is promoted, the formation of fibers is highly favored [208]. As such, when solid particles are present in the media, they are engulfed by the peptide fibers in formation, including them in the supramolecular peptide structure and giving rise to hybrid materials [104, 135, 208-211]. This process favors a strong interaction between the peptide fibers and the solid material that ends up with its surface completely functionalized with the peptides. Moreover, if the solid material is flexible, it can suffer morphological alterations in its structure, the peptide fibers acting as a template [212, 213].

In this process, the supramolecular arrangement of the peptides can also be altered by the interaction of the peptides with the solid particles, resulting, in some cases, an inversion of the supramolecular chirality, as observed by changes in the sign of the Cotton bands in CD spectra. We have previously observed this effect when the self-assembly of Fmoc-FF in the presence of SWCNT (single-walled carbon nanotubes) is triggered by Na_2CO_3 or GdL [104] or in the presence of CNTs of different diameters, as discussed in the previous chapter [209]. In this case, we observed the same effect when passing from the peptide's solutions (Figure 6.1(a)) to the peptides containing SLG (Figure 6.1(b)).

These samples show an inversion of the supramolecular chirality of the peptides; π - π* transition of the fluorenyl groups has positive values for SLG-Fmoc-FF (L) and negative ones for SLG-Fmoc-FF (D). Quite remarkably, this inversion of the supramolecular chirality is not observed when MLG is used (Figure 6.1(c)). In this case, the sign of the CD for the hybrid MLG-Fmoc-FF aggregates are preserved with respect to the Fmoc-FF solutions. Finally, graphene flakes functionalized with achiral Fmoc-GG show no CD as expected, (Figure 6.1(d)).

TEM images of the SLG flakes are shown in Figures 6.1(e)–(g). Figure 6.1(e) shows a reference pristine graphene flake, without any functionalization. It is important to note that the pristine flake appears flat, with sharp, straight edges. In contrast, the functionalized (using Fmoc-FF(D)) flake shown in Figure 6.1(f) appears curved, resembling a partially rolled structure. Figure 6.1(g) shows the partially rolled functionalized graphene flakes on a larger scale. As commented above, this graphene distortion is exerted by the peptide self-assembly process.

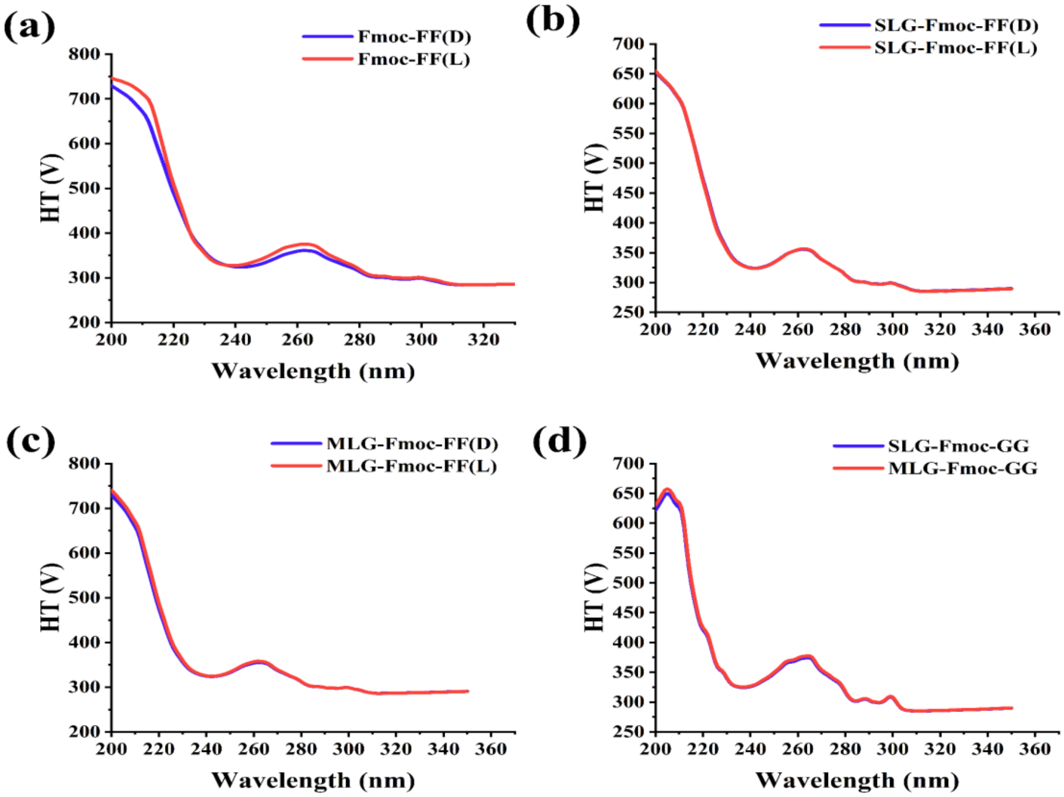

Figure 6.2: (a)-(d) HT spectra of the Fmoc-FF and functionalized SLG and MLG solutions.

Raman spectra of raw and functionalized graphene flakes, measured in ambient air with an excitation wavelength of 532 nm are shown in Figure 6.3 (a). At lower wavenumbers (< 2000 cm^{-1}), the well-known *D* (~1350 cm^{-1}), *G* (~1580 cm^{-1}), and *D′* (~1610 cm^{-1}) peaks are present [214]. While the strongest peak in unfunctionalized (raw) SLG and MLG is the *G* peak, the *D′* peak appears as the dominant peak in the functionalized graphene samples. The appearance of the strong *D′* peak after functionalization indicates the presence of defects and structural disorder. It should be noted that the *D′* peak is relatively weak and can be challenging to distinguish from background noise in the raw samples, however, the presence of strong D' peak in conjunction with the D and G peaks after functionalization indicates lattice distortion.

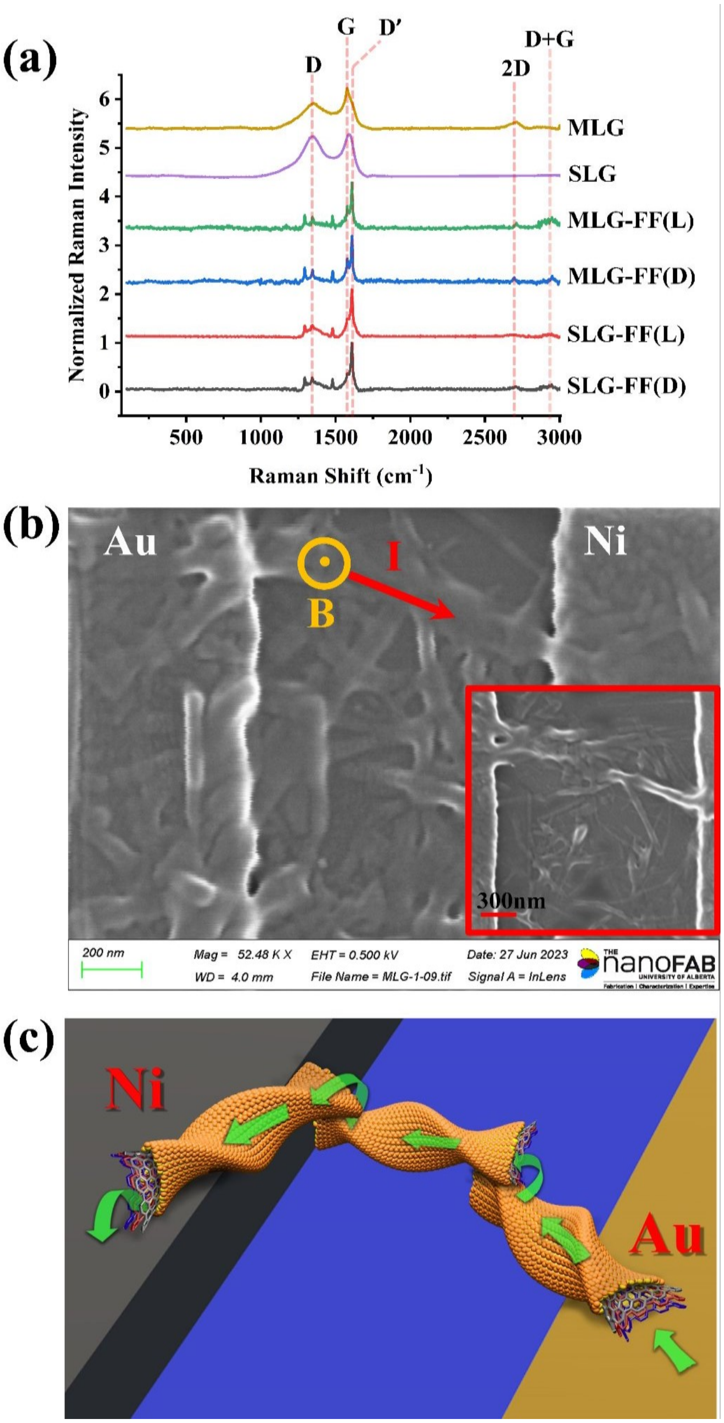

Figure 6.3: **(a)** Raman characterization (532 nm), showing the relevant peaks before and after functionalization. **(b)** FESEM image of a two-terminal device in which a chiral-functionalized graphene layer is contacted by Au, Ni electrodes. Applied magnetic field is out-of-plane. **(c)** Schematic of a typical current path through the chiral graphene flakes, which has both in-plane (primary) and out-of-plane (secondary) components.

As commented above, this can arise from the self-assembly of the peptide molecules, which inflicts strain on the attached SLG and MLG layers, as indicated by the twisted and rolled layers of graphene as seen in Figures 6.1(f), (g).

In the functionalized samples we observe additional peaks at ~1479 cm^{-1}, which is associated with the functionalization-induced structural changes and the vibrational modes of the functional groups [215], and also at ~1294 cm^{-1}, which is related to the oxygen-containing functional groups and carboxyl (-COOH) groups [216]. In addition, we observe weak Raman active bands such as 2D (~2710 cm^{-1}) and D+G (~2950 cm^{-1}) at higher wavenumbers. The presence of defects and disorders broadens and weakens the 2D peak significantly, which is a characteristic of rGO [217].

A two-terminal planar CISS device is fabricated by placing a slice of the gel described above in between Au–Ni contacts. The device is vacuum annealed to improve the electrical contacts as well as to improve the connectivity between the individual chiral flakes [218]. A FESEM image of the final device is shown in Figure 6.3(b). The "rolled-up" graphene structures discussed before are also visible in this image. The contact dimensions are chosen such that the intrinsic resistance of the chiral graphene layer dominates. As evident from the above fabrication process, the graphene film is not homogeneous, but it is composed of multiple graphene flakes, each of which is chiral.

It is important to note that the device is planar and current is injected via the flakes that are in contact with the metallic electrodes at the bottom. However, since the flake size is smaller than the contact gap, carriers need to transfer to the other overlapping flakes to complete the current path. Thus, along with the primarily planar component of charge flow, a small vertical "out-of-plane" component is present as well. This is shown schematically in Figure 6.3(c).

Figures 6.4(a), (b) show the temperature-dependent current-voltage (*I-V*) characteristics of the SLG+Fmoc-FF samples with both chiralities, measured at zero magnetic field. The *I-V* plots as well as the temperature-dependence of resistance of the Fmoc-GG+SLG/MLG samples have been shown in Figure 6.5(a), (b).

The *I-V* characteristics have been found to be nonlinear relative to bias and semiconducting in terms of temperature dependence. Similar behavior has been reported in the literature for monolayer [219-221] as well as multilayer rGO [222]. In rGO, regions of highly conductive graphene islands with delocalized states are separated from each other via disordered regions or "barriers" with localized states, and conduction is limited by the temperature activated hopping mechanism through the localized states [219, 220, 222].

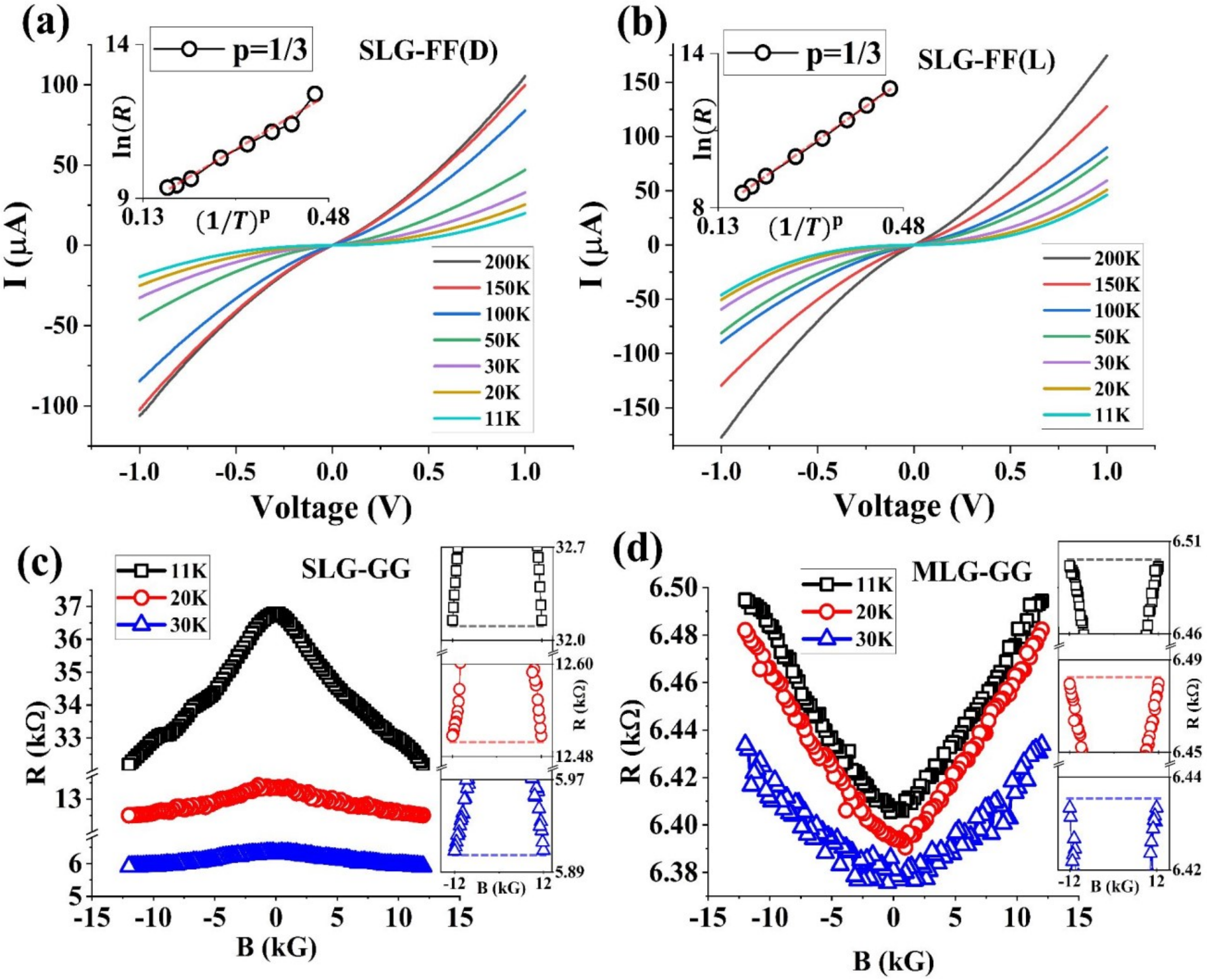

Figure 6.4: (a), (b) Main image – Current-voltage (I-V) characterization of Fmoc-FF L/D functionalized SLG samples. Insets – Fitting with the VRH model. **(c), (d)** Main image – MR characterization of SLG and MLG samples respectively, functionalized with achiral Fmoc-GG molecules. The insets show the symmetry of the MR response. Resistance values are measured at 0.5V.

As bias voltage is increased, electrons acquire sufficient energy and percolate through the flakes via multiple branches (field-assisted tunneling), which gives rise to the non-linear bias-dependence. It is to be noted that in the present case the graphene flakes are functionalized with chiral molecules, which is expected to induce CISS during transport.

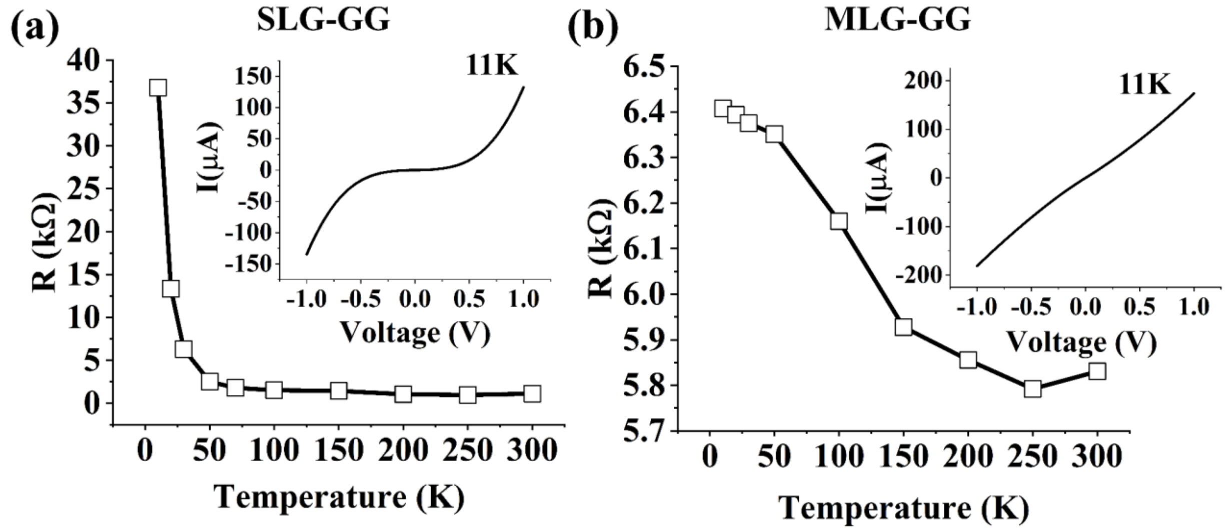

Figure 6.5: (a), (b) Temperature-dependent resistance (measured at 0.5V) and typical I-V characteristics of Fmoc-GG functionalized SLG and MLG samples.

The temperature-dependent *I-V* response in rGO or randomly distributed graphene islands is typically explained in terms of the variable-range hopping (VRH) model [218-222], in which resistance R scales with temperature T as follows: $R \propto exp\,[(T_0/T)^p]$, where T_0 is a parameter known as “characteristic temperature”, and p is a fractional exponent equal to 1/(d+1), where d is the dimensionality of the system. Figures 6.4(a), (b) *insets* show logarithmic resistance (computed at 0.5V) vs. $1/T^{1/3}$. A linear dependence is found, which is consistent with the 2D structures of the rGO flakes.

The temperature dependence of resistance is weaker in MLG samples compared with the SLG samples (Figure 6.5). In the case of MLG, only the surface layer is functionalized, whereas the inner layers are not, and the transport occurs via both inner layers and the surface layers. The unfunctionalized inner layers offer fewer barriers and hence weaker temperature dependence of resistivity for the MLG samples.

Figure 6.4(c) shows the magnetoresistance (MR) of Fmoc-GG functionalized SLG flakes, contacted between Ni-Au electrodes, with magnetic field in the *out-of-plane* direction. It is to be noted that the MR curve is *symmetric*, with R(+12kG) = R(–12kG), as shown in the *insets*. A negative MR, defined as $R(0) – R(\pm 12\text{ kG}) / R(\pm 12\text{ kG})$, of ~ 15% is observed at 11K for the Fmoc-GG+SLG samples, which gradually weakens with increasing temperature. As described above, the system is not a weakly-disordered metallic system, and hence the standard weak-localization theory cannot be used to explain this negative MR. However, even in VRH regime, such negative MR has been reported to appear, due to magnetic field driven carrier delocalization [223].

In general, MLG samples show lower resistance values compared with their SLG counterparts. We believe that the availability of multiple inner current paths via the inner layers of MLG causes lower resistance. The inner layers are not functionalized as discussed above, and hence, they offer fewer barriers, which lowers the overall resistance of the MLG samples.

Figures 6.6(a), (b) show the MR responses of chiral functionalized (using Fmoc-FF L/D) SLG and MLG samples respectively. The background negative (positive) MR is present for SLG (MLG) samples. The new feature is an *asymmetry* in the MR response, which depends on the chirality, as clarified in the *insets*. For example, in the case of SLG samples (Figure 6.6(a)), R(+12 kG) $\gtrless$ *R* (– 12 kG) for L and D chirality respectively. For MLG samples, as shown in Figure 6.6(b), this dependence is *reversed*, for example, *R*(+12 kG) $\lessgtr$ *R* (– 12 kG) for L and D chirality respectively.

Such chirality-dependent MR asymmetry can be explained by invoking the standard CISS phenomenology [100]. The electrons traveling through chiral (L/D) functionalized graphene flakes acquire a chirality-dependent spin polarization (up/down), which is either transmitted or blocked depending on the magnetization of the Ni spin detector, resulting in a chirality dependent asymmetry in MR. Opposite chiralities induce opposite spin polarizations, and hence the MR asymmetry is reversed for L and D chiralities. It is to be noted that in our experiments we have kept the magnetic field perpendicular to the sample plane, and hence perpendicular to the planar current paths. This ensures that the results are minimally influenced by any electromagnetochiral effect [224].

Observation of a CISS signal in such transverse configuration also confirms the existence of transverse spin components perpendicular to the current path. This has been reported before in functionalized carbon nanotubes [164], and is true for functionalized graphene as well. For ideal helical systems, the net transverse spin component is expected to be zero [225]. However, in reality, the direction of spin depends on various factors such as electron energy or the details of the chiral medium and its coupling with the electrodes [225]. These can result in nonzero transverse spin polarizations.

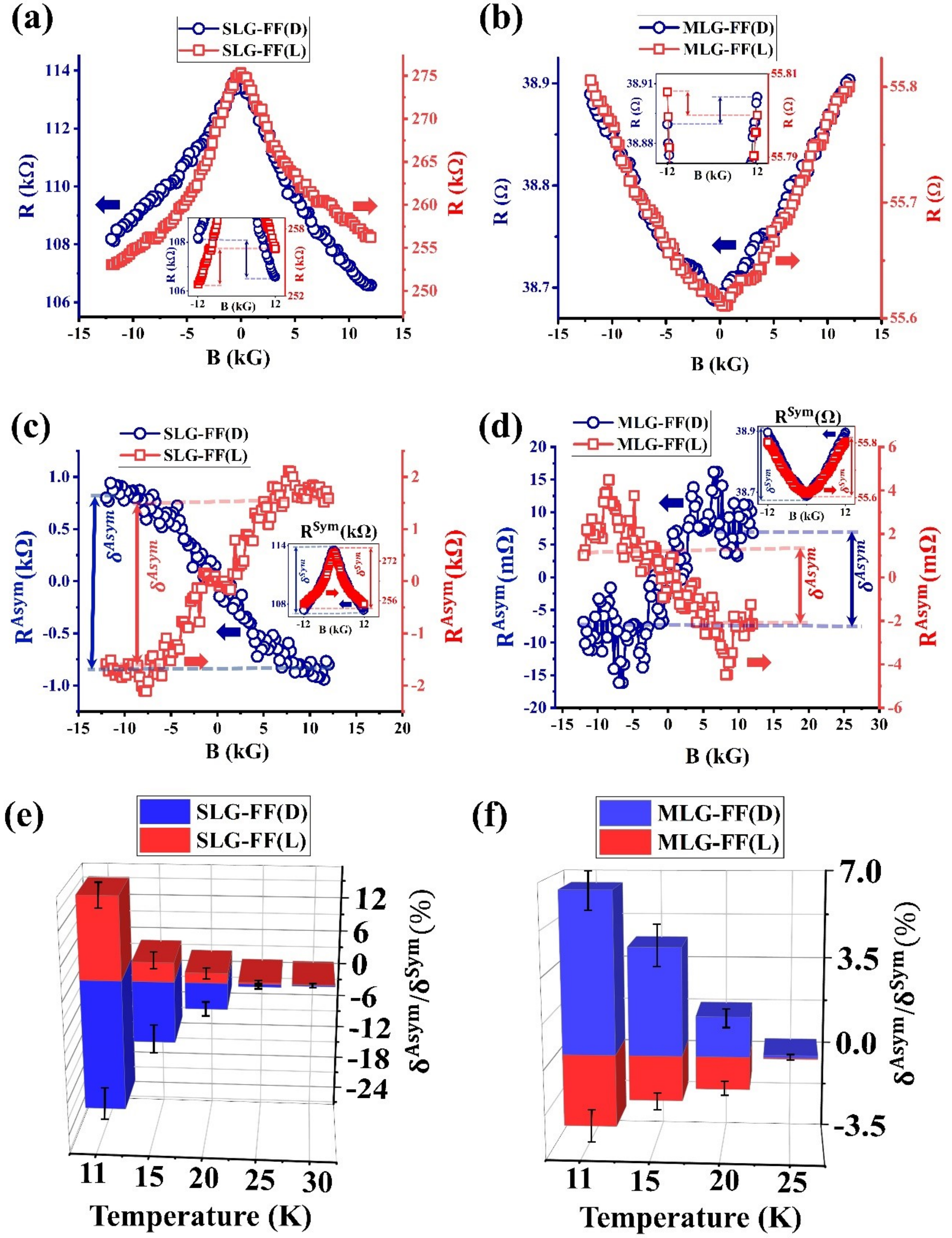

Figure 6.6: **(a)**, **(b)** *Main images* – MR responses of Fmoc-FF L/D functionalized SLG and MLG samples respectively. The *inserts* show the *asymmetry* of the MR response. Resistance values are measured at 0.5V. **(c)**, **(d)** Odd (*main image*) and even (*insets*) components of the MR response. **(e)**, **(f)** CISS signal as a function of temperature for both types of samples.

The opposite MR asymmetries of the SLG and MLG samples correlate with their respective chiralities, as discussed earlier in Figures 6.1(b), (c). The symmetric MR response from the Fmoc-GG functionalized samples shown in Figure 6.4(c), (d) also correlates with the null CD result in Figure 6.1(d). This is a clear indication that the supramolecular chirality associated with the peptide fibers is efficiently transferred to the conductive material [135, 209]. Even though the details about the mechanism of chiral induction are not fully known, it is worth noting that simple CD measurements of supramolecular aggregates gave predictable information about the asymmetry in the MR responses. Consequently, achiral fibers with null CD resulted in no spin selection. Although a correlation between the CISS effect and the sign and magnitude of the CD of the conductive material has been suggested in earlier reports [224-227], the present result shows that the CD signal of the chiral inductor could also infer the CISS response of the composite material.

Since the role of the chiral molecules is to introduce an asymmetry in the MR response, we isolate this contribution by computing the odd component of the MR function, defined as $R^{Asym}(B) = [R(B) - R(-B)]/2$, shown in Figures 6.6(c), (d). Likewise, the CISS-*independent* background symmetric MR is quantified by the even component of the MR function: $R^{Sym}(B) = [R(B) + R(-B)]/2$, as plotted in the *insets* of Figures 6.6(c), (d). The *magnitude* of this CISS-independent symmetric component is defined as $\delta^{Sym} = |R^{Sym}(0\ kG) - R^{Sym}(\pm 12\ kG)|$. Similarly, the strength of the CISS-dependent asymmetric component is computed as $\delta^{Asym} = R^{Asym}(+12\ kG) - R^{Asym}(-12\ kG)$, and the CISS signal is represented as $\delta^{Asym}/\delta^{Sym} \times 100\%$. Figures 6.6(e) and (f) summarize the $\delta^{Asym}/\delta^{Sym}$ responses for SLG and MLG samples respectively, showing their temperature dependence. The CISS signal has been found to decrease with increasing temperature. While this is in contrast with the molecular systems, such temperature-dependence is often observed in solid-state CISS devices [228]. We also observe that the $\delta^{Asym}/\delta^{Sym}$ values of the MLG samples are generally lower than that of the SLG samples under the same conditions. This is expected, because, as discussed above, transport in MLG occurs via multiple inner layers, and these layers are less affected by the chiral molecules, which are attached to the surface layers.

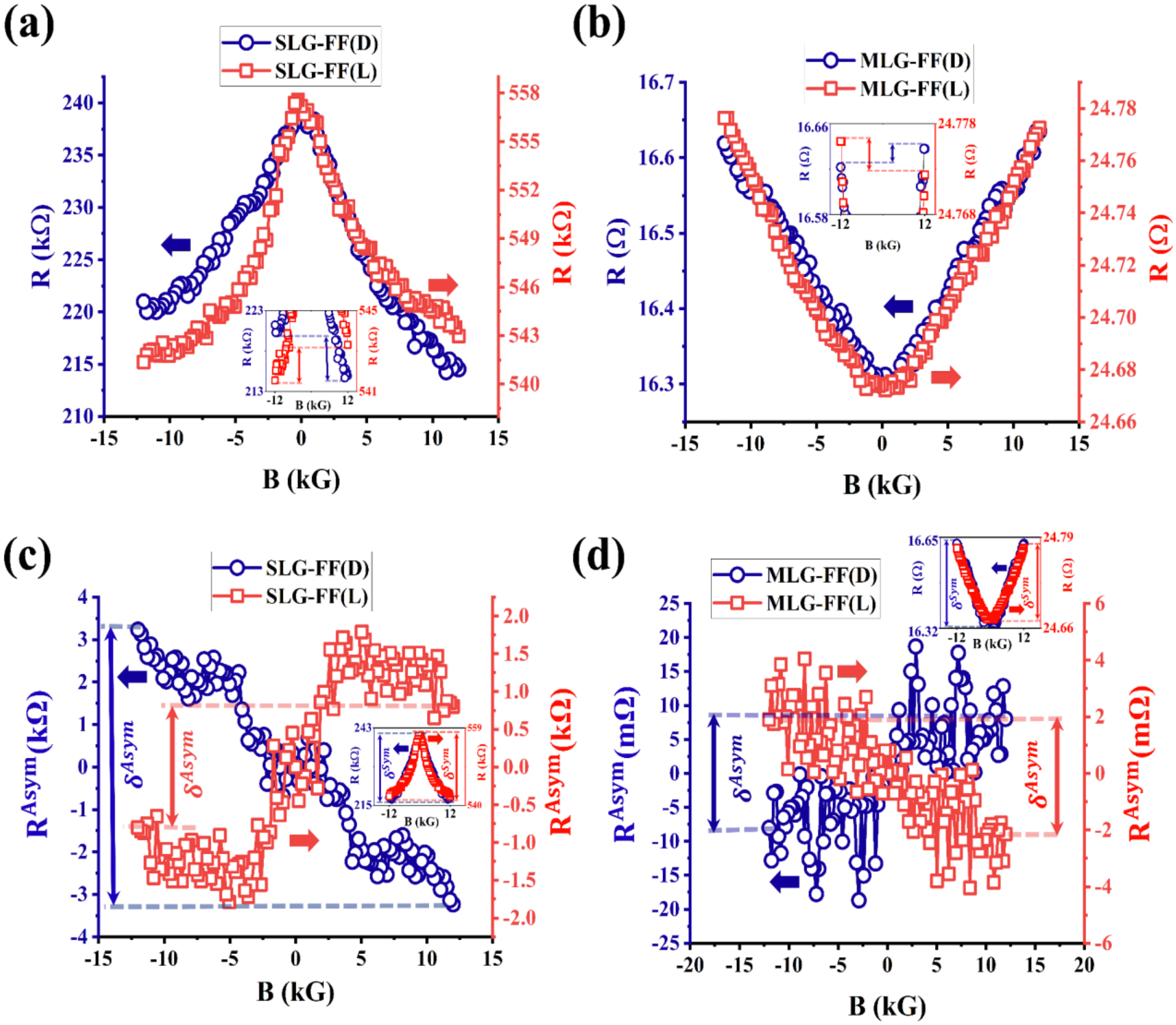

Figure 6.7: MR data from a different set of samples. **(a)**, **(b)** Main images – MR responses of Fmoc-FF L/D functionalized SLG and MLG samples respectively. The *insets* show the asymmetry of the MR responses. Resistance values are measured at 0.5V. **(c)**, **(d)** Odd (main image) and even (insets) components of the MR response. The computed CISS signal ($\boldsymbol{\delta^{Asym}}/\boldsymbol{\delta^{Sym}}$) values are as follows: SLG FF D: - 24.9%; SLG FF L: 10%; MLG FF D: 5.1%; MLG FF L: - 3.7%.

We measured four different SLG samples and nine different MLG samples. For the SLG samples, since the signal was stronger, we typically measured each device two or three times at a given temperature and bias. For the MLG samples, since the signal was weaker, we typically measured each device five or six times. The signals are reproducible, and the error bars shown in Figure 6.6(e), (f) are derived from all of the above scans, i.e., including different devices as well as multiple scans on the same device. In Figure 6.7, we have added data obtained from a different set of samples, showing the reproducibility and variability of these results.

A self-consistent theoretical model of the CISS effect currently does not exist, and it is a subject of significant research activity [101]. It is generally thought that spin-orbit interaction, along with spatial inversion asymmetry (due to the chiral structure) and time inversion asymmetry (due to the external magnetic field) are the necessary components for observation of this phenomenon [101]. Spin-orbit interaction of pristine graphene is weak, due to the low atomic number of carbon [166], and hence the observation of CISS effect discussed above is somewhat surprising. However, in the present case, there are several factors that may mitigate this effect:

(a) First, it has been reported by theoretical calculations that curved graphene layers have an additional spin-orbit term that arises due to mixing of σ and π bands due to local curvature[166]. Such curvature-induced spin-orbit interaction is estimated to be an order-of-magnitude stronger than the intrinsic spin-orbit coupling [166]. In our case, on the molecular level, the chiral entities form a helical supramolecular structure. It's important to note that the chiral molecules are strongly attached to the graphene layers via π-π interactions. Hence, when these molecules self-assemble to form superhelical structures, so do the graphene layers attached to them (so-called "conformational chirality"), which makes the graphene layers curved and this can enhance the spin-orbit coupling. The TEM images in Figure 6.1(f), (g) and the FESEM image in Figure 6.3(b) indicate that the graphene layers are indeed curved. We also note that due to the relatively higher structural rigidity of MLG samples compared to SLG, such effect is expected to be weaker in MLG, which is consistent with the observation of weaker CISS signals from MLG samples.

(b) Second, and perhaps more importantly, the system under consideration is rGO, instead of pristine graphene. Due to the synthesis mechanism of rGO, there exist impurity atoms (such as hydrogen) on the graphene lattice [193, 229, 230]. Such impurities can cause local lattice distortion via sp^3 hybridization, which can significantly enhance the local spin−orbit interaction [231, 232]. According to some studies, such enhanced spin−orbit interactions can approach values comparable to those in zinc- blende semiconductors [231]. Such spin−orbit enhancements are presumably responsible for the CISS signal in rGO, even though it is not expected in pristine, impurity-free graphene. We note that such adatom-induced enhancement of the spin−orbit interaction is responsible for small spin relaxation times in graphene [233]. Apart from the above factors that enhance the spin−orbit coupling in rGO, we note that there are several sources of magnetic defects, as well. The hydrogen adatoms discussed above can give rise to local magnetic moments [234].

Carbon vacancies, which typically arise during GO synthesis and its thermal exfoliation reduction, are well-known magnetic defects [193, 229, 230]. Such local magnetic interactions can also contribute to the observed CISS effect.

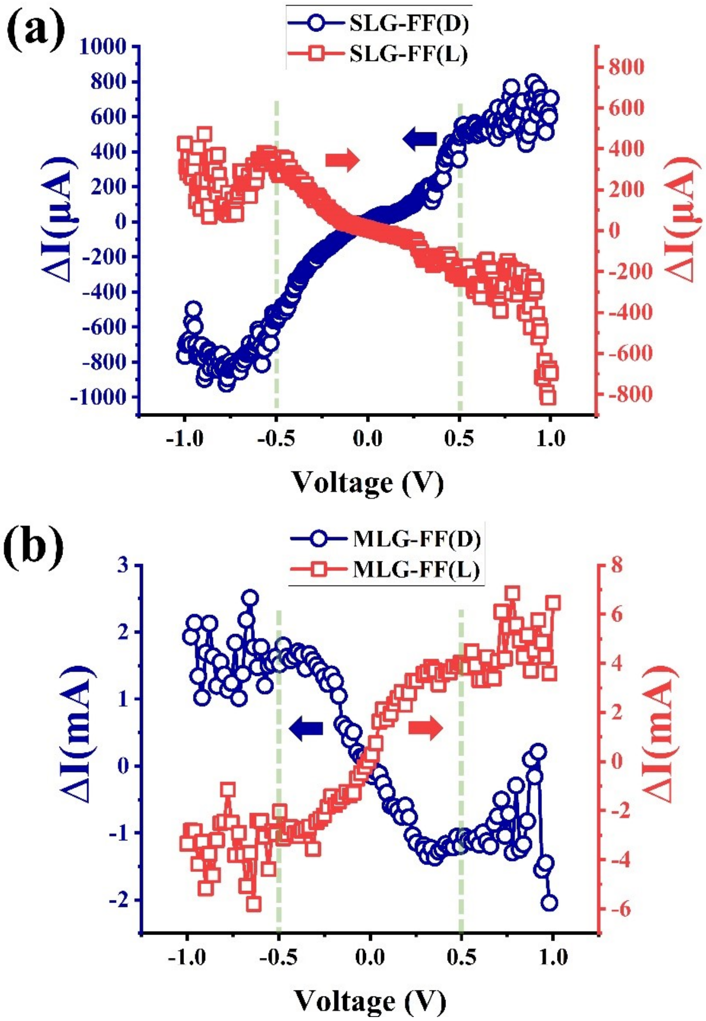

Figure 6.8: (a), **(b)** Bias dependence of Δ*I*, computed as *I*(+12 kG) – *I*(–12 kG), for SLG/MLG+Fmoc-FF (L/D) respectively. The current difference approaches zero as the bias is reduced (approaching "linear range"), consistent with Onsager's reciprocity principle.

Figure 6.8 shows the differential current signal Δ*I*, computed as *I*(+12 kG) – *I*(–12 kG) as a function of applied voltage bias. In a two-terminal measurement geometry with only one magnetic contact, as shown in Figures 6.3(b) and (c), Δ*I* is expected to be zero according to Onsager's reciprocity principle, at least in the *linear* region [102]. As seen from Figure 6.8, Δ*I* approaches zero as voltage bias approaches zero i.e. as the device enters the linear region of operation. The current differential Δ*I* due to the CISS effect increases with bias, and manifests in the *non-linear* region of transport in the present measurement geometry. This result is consistent with that observed recently in CNT based CISS devices [164]. The CISS signal saturates around ~0.5V, and hence the MR curves discussed in Figures 6.4, 6.6, and 6.7 have been acquired at this optimum bias value.

6.3 Summary and conclusion

Graphene is a promising 2D material for emerging electronic and spintronic devices, however, its compatibility with the CISS effect was never explored before. In fact, weak spin-orbit interaction of graphene makes occurrence of CISS unlikely in this material. Nevertheless, in this work, we have demonstrated that the CISS effect manifests in rGO flakes functionalized by chiral dipeptide molecules. The chiral molecules organize in supramolecular structures, resulting in a "conformational chirality" of the attached graphene flakes. This introduces a curvature in the graphene flakes, as shown by the microscopic images discussed in this paper. Such curvatures as well as other symmetry-breaking factors discussed in this paper presumably contribute to the CISS signal. The simple and straightforward methodology described in this chapter can be used to induce chirality and CISS properties in a multitude of easily accessible advanced 2D conductive materials, vastly expanding device design opportunities and associated applications. The observed CISS signal correlates with the supramolecular chirality of the medium, emphasizing the importance of "global chirality" as opposed to "local chirality" in CISS phenomenon [104, 209, 235].

In the next chapter, as part of our ongoing work, we enhance our comprehension of the CISS phenomenon described above through angle-resolved MR measurements. We demonstrate how the chirality-dependent two-terminal CISS MR manifests at various measurement angles for various combinations of magnetic and non-magnetic electrodes.

Chapter 7: Thesis Summary

As the result of the first Project, we present current-perpendicular-to-plane (CPP) magnetoresistance (MR) results from ultrathin flakes of 1T-VSe_2. A significant positive, linear, and non-saturating MR effect, approximately 60%–70%, is observed near room temperature (~250K) within a magnetic field range of ±12kG. This robust MR effect, which occurs significantly beyond the charge density wave (CDW) temperature, indicates 1T-VSe_2 as a promising material for 2D-based magnetic sensors.

Unlike conventional MR effects, thermal fluctuations enhance the observed MR in 1T-VSe_2. This MR effect is attributed to mobility inhomogeneity in the carrier transport path. In 1T-VSe_2, in-plane conduction is metallic, while out-of-plane conduction exhibits mixed metallic and semiconducting behavior due to the inhomogeneous structure of 1T-VSe_2, which is more pronounced in the CPP geometry. Consequently, the net CPP transport is inhomogeneous, contributing to the MR effect. The high mobility regions consist of VSe_2 layers, while the low mobility regions, which act as barriers, consist of weak interlayer coupling. Subsequently, this mechanism leads to an increase in MR with rising temperature and decreasing flake thickness.

Other 2D materials and van der Waals (vdW) heterostructures with inhomogeneous structures and dissimilar transport properties along in-plane and out-of-plane directions may also exhibit high MR responses in CPP geometry. It may be possible to harness this naturally occurring property to observe similar MR responses across a broad family of 2D materials. Furthermore, mobility fluctuations could be tuned by intercalating vdW materials or even organic molecules. This would potentially enhance the inhomogeneous structure of the hybrid material, leading to higher MR at room temperature. Unlike other 2D magnetic materials, this effect is not limited by the Curie temperature, as it does not rely on the magnetic properties of the layers.

In the second project, we investigated chirality-induced spin selectivity (CISS) in chiral hybrid composites within 1D and 2D systems, using carbon nanotubes (CNTs) and graphene. The CISS effect offers a way to generate spin-polarized currents at the nanoscale using chiral hybrid nanostructures without the need for magnetic materials.

We unveiled the role of spin-orbit coupling (SOC) in the CISS effect. The physical origin of CISS is often debated, particularly regarding the contribution of SOC in the chiral medium and the impact of other electromagnetic chiral (EMCh) effects. In this study, we eliminated the EMCh effect using a transverse geometry but still observed characteristic CISS signals. The strength of this pure CISS signal scales proportionately with the spin-orbit strength of the medium, indicating that SOC plays a critical role in CISS, independent of EMCh.

In this hybrid system, transport occurs via CNTs, and the carriers experience the CNT spin-orbit interaction. The attached molecules have insulating nature and negligible spin-orbit interaction due to their low atomic numbers. Consequently, they do not contribute significantly to the SOC. However, the inversion-asymmetric electrostatic helical potential induced by the molecules can enhance the native SOC of the CNTs via the Rashba effect. The role of the chiral molecules is to create an inversion-asymmetric helicoidal electric field on the charge carriers. This electric field generates a strong Rashba SOC in the channel, splitting the energy bands and polarizing the electron spins. Our study demonstrates that the strength of SOC in the main channel is crucial for the CISS effect. The supramolecular chirality of the medium significantly influences spin polarization, thereby enhancing our understanding of spintronic phenomena in hybrid systems.

In the second project, we also explored the potential transfer of the CISS effect from one-dimensional (1D) to two-dimensional (2D) systems using graphene. While graphene exhibits promising properties for emerging electronic and spintronic devices, its compatibility with the CISS effect has not been previously investigated due to its weak spin-orbit interaction. Nonetheless, our study demonstrates the manifestation of the CISS effect in reduced graphene oxide (rGO) flakes functionalized with chiral dipeptide molecules. These molecules organize into supramolecular structures, inducing "conformational chirality" in the attached graphene flakes. Microscopic imaging confirms the presence of curvature in the graphene flakes, which, along with other symmetry-breaking factors discussed in this thesis, likely contribute to the observed CISS signal. To further investigate the CISS effect in the 2D system, we are conducting angle and contact-dependent measurements as part of the future work presented in the appendix. The methodology outlined in this thesis offers a simple and effective approach to induce chirality and CISS properties in various readily available 2D conductive materials, thereby expanding the possibilities for device design and applications. The observed CISS signal is closely linked to the supramolecular chirality of the medium, underscoring the significance of "global chirality" in the CISS phenomenon compared to "local chirality”.

Overall, in this thesis, we shed light on the magnetotransport properties of 1T-VSe_2, the CISS mechanism in 1D nanotubes, and the feasibility of transferring CISS from 1D to a 2D system. We demonstrate the potential of 2D TMD materials as an alternative platform for miniaturized magnetic sensors. We have also highlighted possible directions for further research based on these results presented in the appendix.

Appendix A: Future Works on 2D VSe_2

As part of our ongoing research, we are currently designing additional experiments to gain a deeper understanding of the intrinsic transport inhomogeneity in 2D VSe_2 and related compounds. Specifically, our investigations are centered around two main topics: (a) Angle and bias dependence of magnetoresistance for 1T-VSe_2 flakes and (b) structural phase transition of VSe_2 and its oxide, as well as investigation of their transport properties.

In addition, we are further investigating the CISS effect within the realm of 2D materials. In particular, we are investigating the mechanism and origins of CISS MR in 2D chiral hybrid materials via angle-resolved MR measurements. We demonstrate how the chirality-dependent CISS MR manifests even for *non-magnetic* electrodes in two-terminal system. These results highlight the importance of non-magnetic-chiral media interface for a proper interpretation of the CISS MR, which remains elusive.

A1: Angle and bias dependence of magnetoresistance for 1T-VSe_2 flakes

The investigation into the impact of applied electric fields, achieved by varying the applied bias on the CPP geometry of 1T-VSe_2, may provide valuable insights into the mechanism of mobility inhomogeneity discussed in Chapter 4. By manipulating the electric field strength, we have the ability to adjust in-plane momentum scattering and inter-plane potential barrier bending. As both phenomena are intertwined in van der Waals materials, we expect this experiment to yield valuable insights into the conditions that determine the dominance of these phenomena. Furthermore, the impact of the magnetic field direction on the CPP geometry of 1T-VSe_2 has not been explored, which could potentially lead to higher CPP magnetoresistance (MR) at room temperature considering the impact of Lorentz force.

A2: Structural phase transition of VSe_2 and its oxide

The structural phase transition of multilayer VSe_2 is an ongoing field of research and has garnered significant attention in the field of spintronics [236]. Under certain conditions VSe_2 exhibits a fascinating phase transition between two distinct crystal structures: the 1T (octahedral) and 2H (hexagonal) phases. In contrast to other dichalcogenide compounds such as MoS_2 and WSe_2, VSe_2

exists in the crystallographic form of 1T. Theoretically, it has been shown that the 2H-phase of VSe_2 multilayers have a Curie−Weiss temperature up to 425K and behave like high-temperature 2D ferromagnetic semiconductor [84]. In addition, the bilayer of 2H-VSe_2 is predicted to be a 2D antiferromagnetic van der Waals crystal with electrically-induced half-metallicity properties [97]. As part of an on-going project, we expect to achieve the phase transition from the 1T to 2H phases via annealing using RTA. Our initial results indicate that annealing under vacuum at 300-340˚ C did not change the Raman spectroscopic characteristic of 1T, indicating the two Raman active modes at ~137cm^{-1} (E_g) and ~211cm^{-1} (A_{1g}), as shown in Figure A.1(a). Meanwhile, annealing in the presence of Ar flow at the same temperature range results in a change in the Raman peak. It splits the out-of-plane A_{1g} mode of 1T into two prominent peaks at ~190 and ~220cm^{-1}, as shown in Figure A.1(b). These two peaks are assigned as the out-of-plane E_{2g} mode and in-plane A_{1g} mode of 2H- VSe_2 [237, 238].

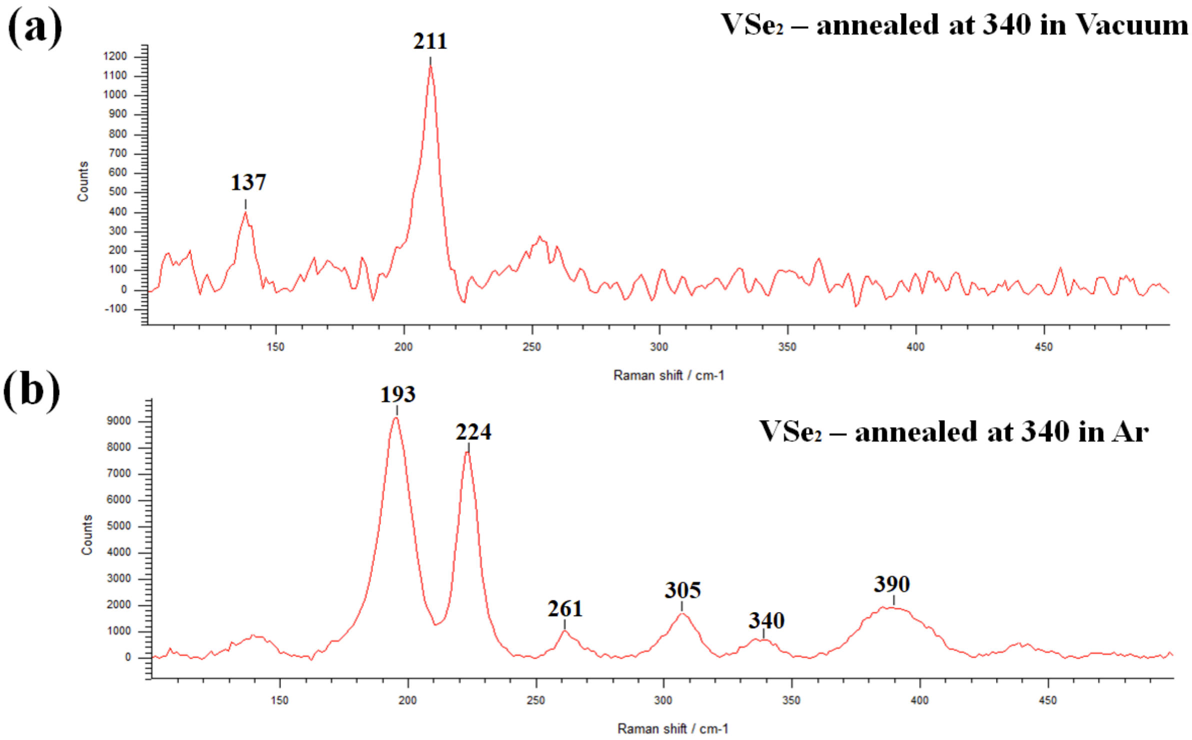

Figure A.1: Raman spectroscopic results of annealed VSe_2 flakes in vacuum **(a)** and in Ar **(b)**

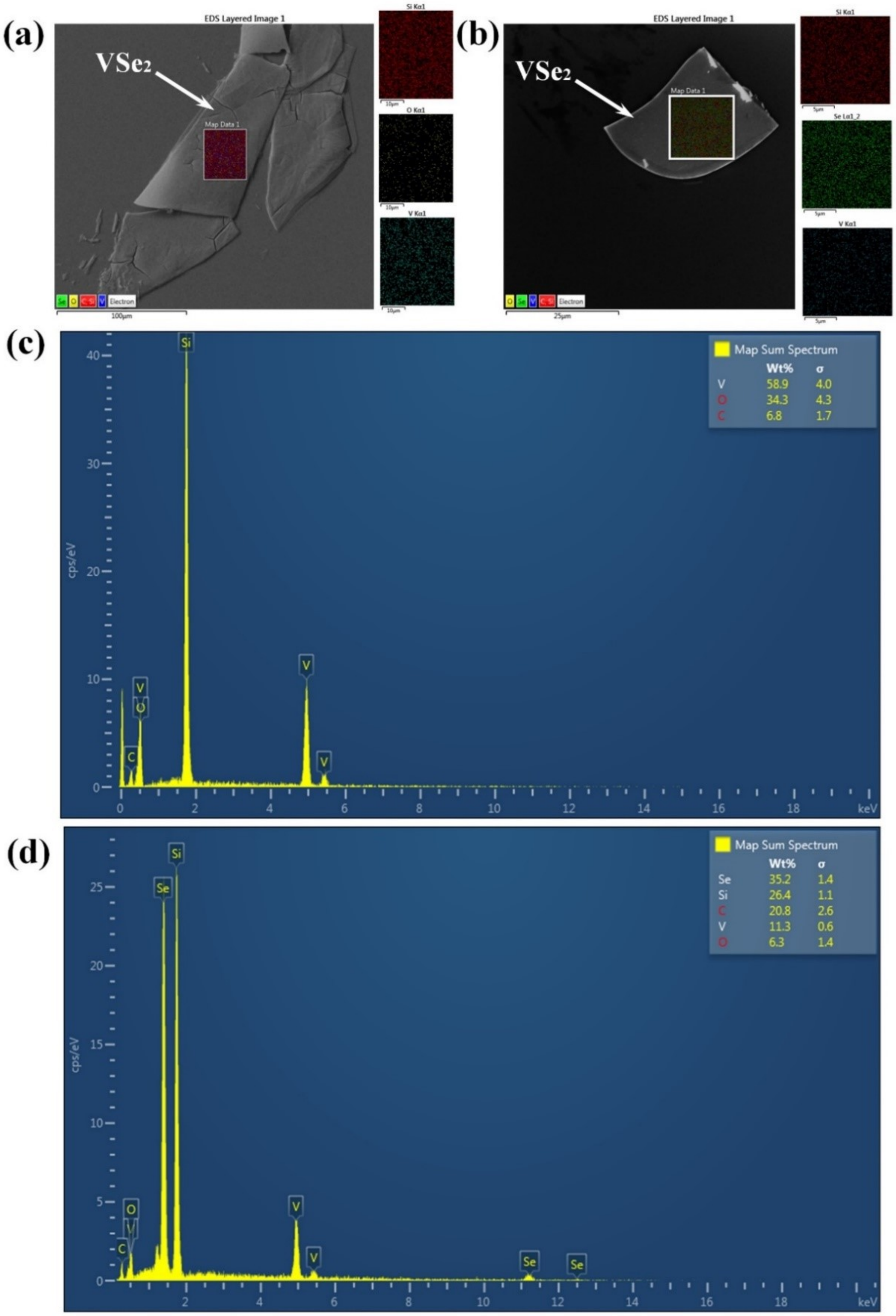

Figure A.2: (a), (b) SEM images of the annealed and non-annealed VSe_2 flakes on Si substrate and elemental analysis, respectively. **(c), (d)** EDX analysis of the annealed and non-annealed VSe_2 flakes on Si substrate, respectively.

However, EDX results shown in Figure A.2(a) and (c), indicate that the Se atoms, which are present in non-annealed flakes as shown in Figure A.2(b) and (d), are substituted by O atoms during the annealing process. Therefore, we aim to fine tune the RTA parameters to preserve the proper stochiometric ratio of VSe_2.

Appendix B: Future Works on CISS effect on 2D system

B: Two-Terminal Asymmetric Magnetoresistance in Peptide Functionalized Graphene Devices - The Role of Chirality and Contacts

As mentioned in previous chapters, the CISS effect in 2D system has recently drawn significant attention, because it can potentially allow magnet-free, chemically tunable, molecular-scale spin sources and detectors [100, 101]. In previous chapters, we showed that chiral hybrid materials inserted between a ferromagnet (FM) and non-magnet (NM) terminals typically exhibit a two-terminal asymmetric magnetoresistance (MR), attributed to the CISS effect. In this work we show that this two-terminal asymmetric MR response is quite *general*, and can arise even in the case of an *achiral* medium contacted by *non-magnetic* electrodes. By introducing chirality in the channel, and via angle-resolved MR measurements we demonstrate how the chirality-dependent CISS MR manifests, superimposed on this general effect, even for non-magnetic electrodes.

B.1: Overview

As discussed before, electronic transport in chiral spintronic devices is commonly studied using a two-terminal stacked geometry, in which a thin chiral film is sandwiched between one ferromagnetic (FM) contact (e.g. Ni), which acts as a spin detector, and one non-magnetic (NM) contact (e.g. Au) [100, 105, 106, 235]. According to the standard CISS picture, spin unpolarized electrons ejected from the NM contact acquire a chirality-dependent spin polarization while traveling through the chiral layer and are detected via the FM spin detector. For a given chirality, the generated spin polarization is fixed, thus, changing the magnetization of the FM spin detector by an external magnetic field B result in different resistance (R) values, generating an *asymmetric two-terminal* CISS magnetoresistance (MR): $R(+B) \neq R(-B)$. The sign of the asymmetric CISS MR will flip for the opposite chirality. It is generally assumed that the generated spins are collinear with the chiral axis and the current (I), and hence, to maximize the measured signal, the FM contact is magnetized collinear with this direction. For the vertical stacked geometry, this means an out-of-plane magnetization of the FM terminal.

Despite the apparent simplicity of the above device, the explanation of the observed two-terminal MR is surprisingly complex. Apart from the standard explanation described above, the two-terminal MR can also be explained by other mechanisms that *do not* depend on spin transport. For example, chiral media are known to exhibit electromagnetochiral anisotropy (EMChA) effect in which $R \approx R_0 + \alpha^{\mathrm{L/D}} B.I$; $\alpha^{\mathrm{L/D}}$ being a chirality dependent parameter with $\alpha^{\mathrm{L}} = -\alpha^{\mathrm{D}}$ [103, 163], as discussed in previous chapter. Some studies have suggested EMChA as the possible mechanism behind CISS MR [103, 163], although no consensus has been reached [103, 164]. Alternatively, some studies have found that the potential barrier between a chiral molecule and a ferromagnet can be tuned by changing FM magnetization or the chirality [239]. It has been argued that this can result in the observed two-terminal MR [240]. Overall, an explanation of the two-terminal CISS MR remains elusive [102, 106, 240, 241].

While chiral systems coupled with FM leads have been studied extensively, *achiral* systems as well as *devices with NM lead pair* have received less attention, presumably due to the fact that *a priori* no CISS phenomenon is expected. In this study we show that even *achiral* systems can result in an asymmetric two-terminal MR response that mimics a CISS MR, while connected between *NM* electrodes. As chirality is introduced in the channel, the typical chirality-dependent CISS MR emerges at certain configurations *even when both electrodes are NM*. As expected, the CISS MR persists when the standard NM-FM contact pairs are used. These findings highlight the importance of NM-chiral media interface along with the well-studied FM-chiral media interface, for a proper interpretation of the CISS MR.

B.2: Results and discussions

In this study we employ a planar geometry, in which a graphene thin film, consisting of multiple few-layer (1– 5) graphene flakes, is contacted by two planar electrodes (Figure B.1(a)). Chirality can be transferred to the graphene channel via attached molecules (such as Fmoc FF L/D: N-Fluorenylmethoxycarbonyl-L/D-diphenylalanine), and this system has already been shown to exhibit the CISS MR, as discussed in Chapter 6 [209]. An *achiral* channel can also be created using Fmoc-GG (Fmoc-diglycine) as the functionalization agent. We first explore the two-terminal MR of this achiral channel with nominally identical Au-Au contacts, before moving on to the conventional Ni-Au setup. Typical contact thickness is ~100 nm in all cases, and the gap between the contacts is ~ 2μm. The graphene film is drop-cast on the contacts from a gel solution and subsequently annealed. Due to the relatively shallow height of the contact walls compared to the contact gap, the drop-cast film is expected to fill the gap completely. Functionalized graphene flakes typically have a folded structure as shown by the TEM image in Figure B.1(a).

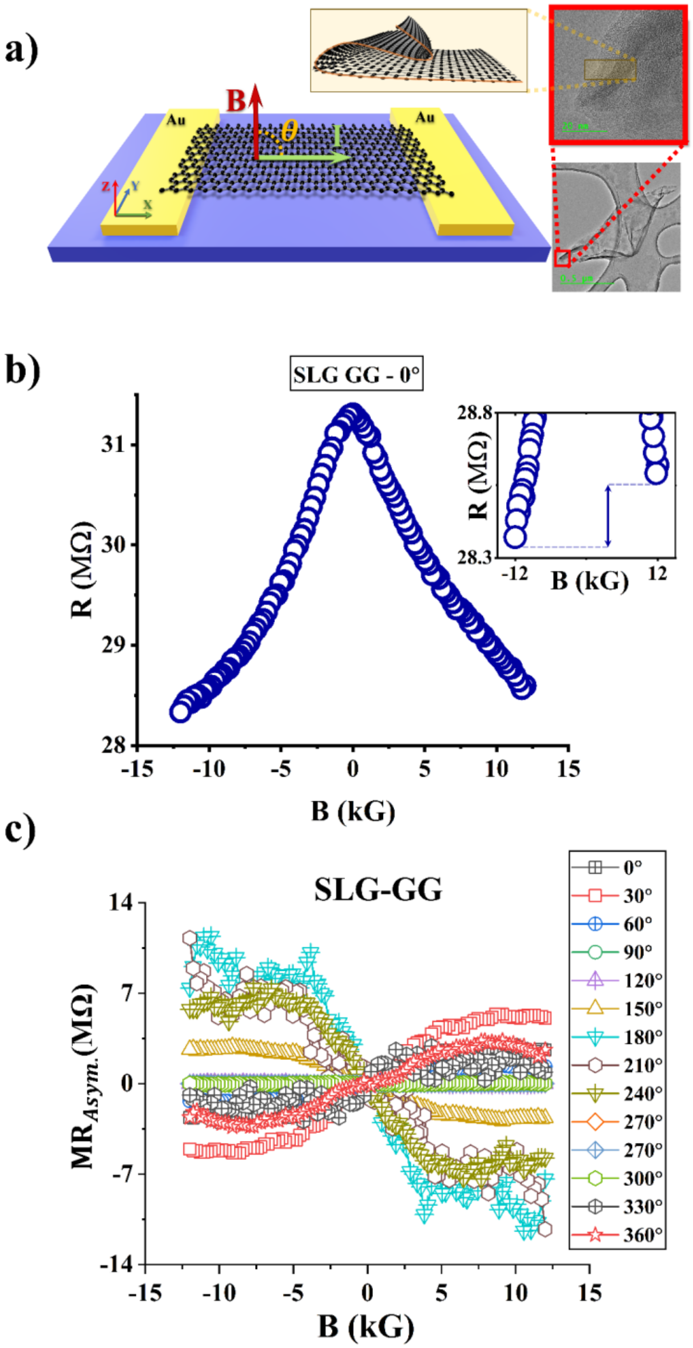

Figure B.1: **(a)** Device schematic, and the TEM image of a typical folded functionalized graphene flake. Such folded flakes constitute the channel. **(b)** Typical asymmetric MR measured with Au-Au electrodes for an achiral (Fmoc-GG functionalized) channel, at $\theta = 0^{o}$. The asymmetric nature of the MR is shown in the *inset*. **(c)** Asymmetric component of the MR as a function of θ.

In contrast to the vertical stacked geometry, in which chiral media sandwich between two terminals, the planar geometry is free from any pinhole contacts and any spurious MR effect originating thereof [242]. Using this system, we report two-terminal asymmetric MR in two non-standard configurations. Contrary to all of the studies in this area, we show that an asymmetric CISS-type MR can exist even when *both contacts are non-FM* (such as Au-Au) and the transport medium is *achiral*. This effect is strongest in a longitudinal configuration where B is collinear with I. As shown in Figure B.1(a), the current paths are in the *x-y* plane, and the *average* "drift" current I flows perpendicular to the edges of the two contacts. The magnetic field angle (θ) is measured with respect to this direction; $\theta = 0^{\circ}$ when the magnetic field is in-plane and parallel with I, and $\theta = 90^{\circ}$, when the magnetic field is perpendicular to the plane, as illustrated in Figure B.1(a). In the $\theta = 90^{\circ}$ configuration, the magnetic field is perpendicular to *all* current paths in the *x-y* plane.

We start with the simplest configuration in which an *achiral* Fmoc-GG functionalized graphene film is contacted by symmetrical Au-Au electrodes. Absence of chirality is confirmed by the CD signal, obtained from Fmoc-GG + graphene solutions (Figure B.2(c)). The two-terminal MR shows a signature global negative MR, with resistance decreasing with increasing magnetic field strength (Figure B.1(b)) [209, 242]. Interestingly, despite the symmetric nature of the contacts and the lack of chirality of the medium, the MR response is found to be *asymmetrical*, i.e. $R(+B) \neq R(-B)$ for several field angles θ. The symmetric and asymmetric MR components are computed as $\mathrm{MR}_{\mathrm{Sym}}(B) = R(+B) + R(-B)/2$ and $\mathrm{MR}_{\mathrm{Asym}}(B) = R(+B) - R(-B)/2$, and an MR "*asymmetry factor*" χ_{Asym} is defined as the ratio of the magnitudes of these components i.e. $\chi_{\mathrm{Asym}} = [\mathrm{MR}_{\mathrm{Asym}}(+12\ \mathrm{kG}) - \mathrm{MR}_{\mathrm{Asym}}(-12\ \mathrm{kG})] / [\mathrm{MR}_{\mathrm{Sym}}(0\ \mathrm{kG}) - \mathrm{MR}_{\mathrm{Sym}}(\pm 12\ \mathrm{kG})] \times 100\%$. The asymmetric MR component $\mathrm{MR}_{\mathrm{Asym}}$ is plotted in Figure B.1(c).

The angular dependence of χ_{Asym} resembles a $\sim\cos(\theta)$ function as shown in Figure B.3(a). The error bars are calculated based on the analysis of two samples per case, each with a minimum of six scans, to confirm the reproducibility of the data. The appearance of an asymmetric MR is counterintuitive, because being achiral, Fmoc-GG is not expected to transfer any chirality to the attached graphene channel. When achiral Fmoc-GG self-assembles to form a supramolecular structure, the flexible graphene flakes (also achiral) attached with the molecules bend as well (Figure B.1(a)). Due to the irregularity of the resulting composite structure, it could be viewed as chiral from a structural point of view. However, since none of the starting ingredients (Fmoc-GG and SLG) is chiral, the functionalized graphene flakes should bend left and right in the same proportion, resulting in an overall achiral film. If there is a symmetry breaking phenomenon during self-assembly [243], there will be a slightly higher percentage of bending to the left than bending to the right or vice versa, resulting in a chiral channel. However, this can be ruled out due to the absence of any significant CD signal (Figure B.2(c)). The lack of chirality excludes EMChA as a possible mechanism, despite it predicting the $\sim\cos(\theta)$ dependence of χ_{Asym} correctly. Also, according to the standard CISS picture, due to the lack of chirality and also owing to the symmetric non-magnetic Au-Au contacts, no CISS-induced asymmetric MR is expected.

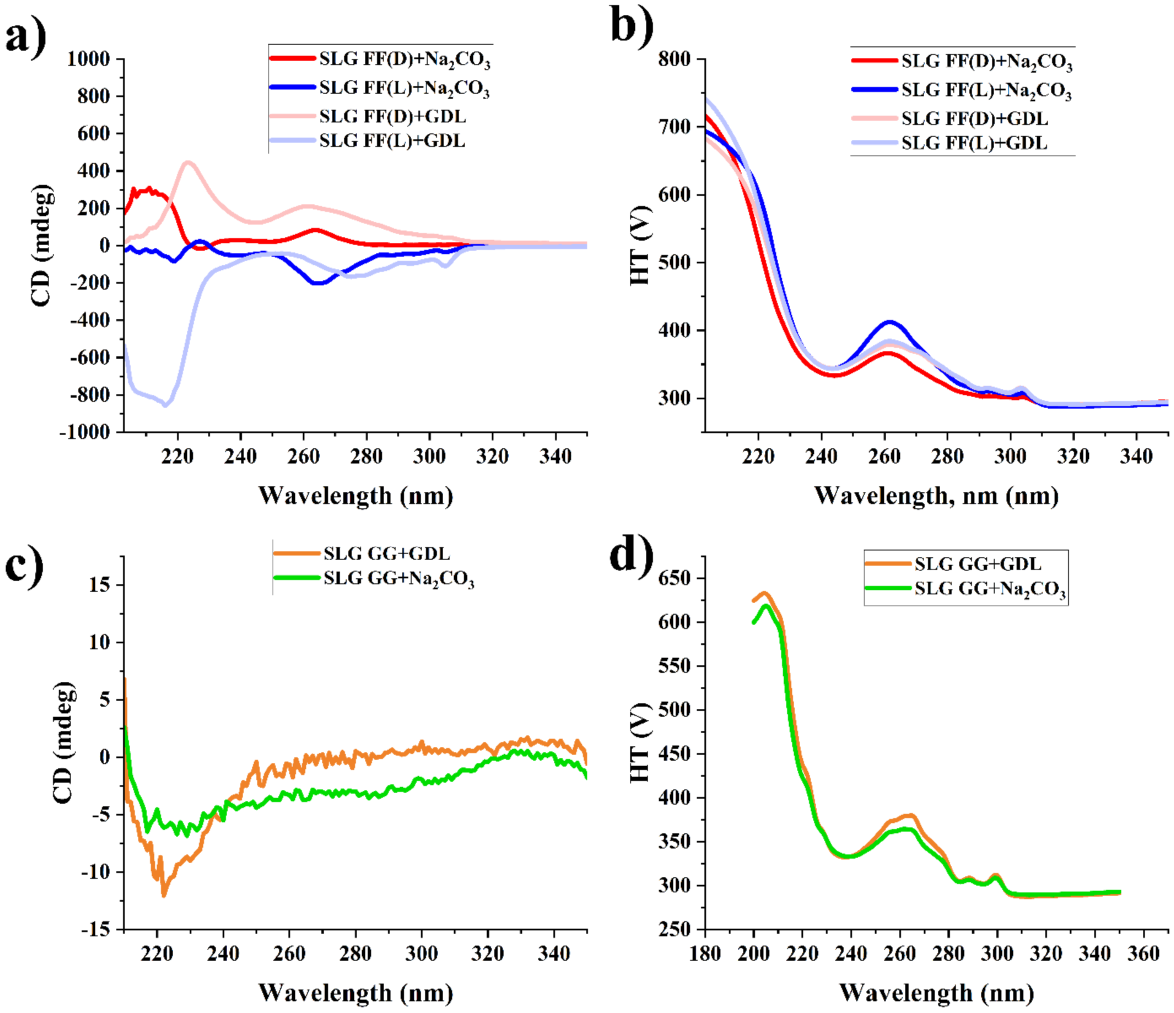

Figure B.2: (a), **(c)** CD characterizations of the functionalized SLG with Fmoc-FF(L/D) and GG. **(b)**, **(d)** HT spectra of the functionalized SLG with Fmoc-FF(L/D) and GG.

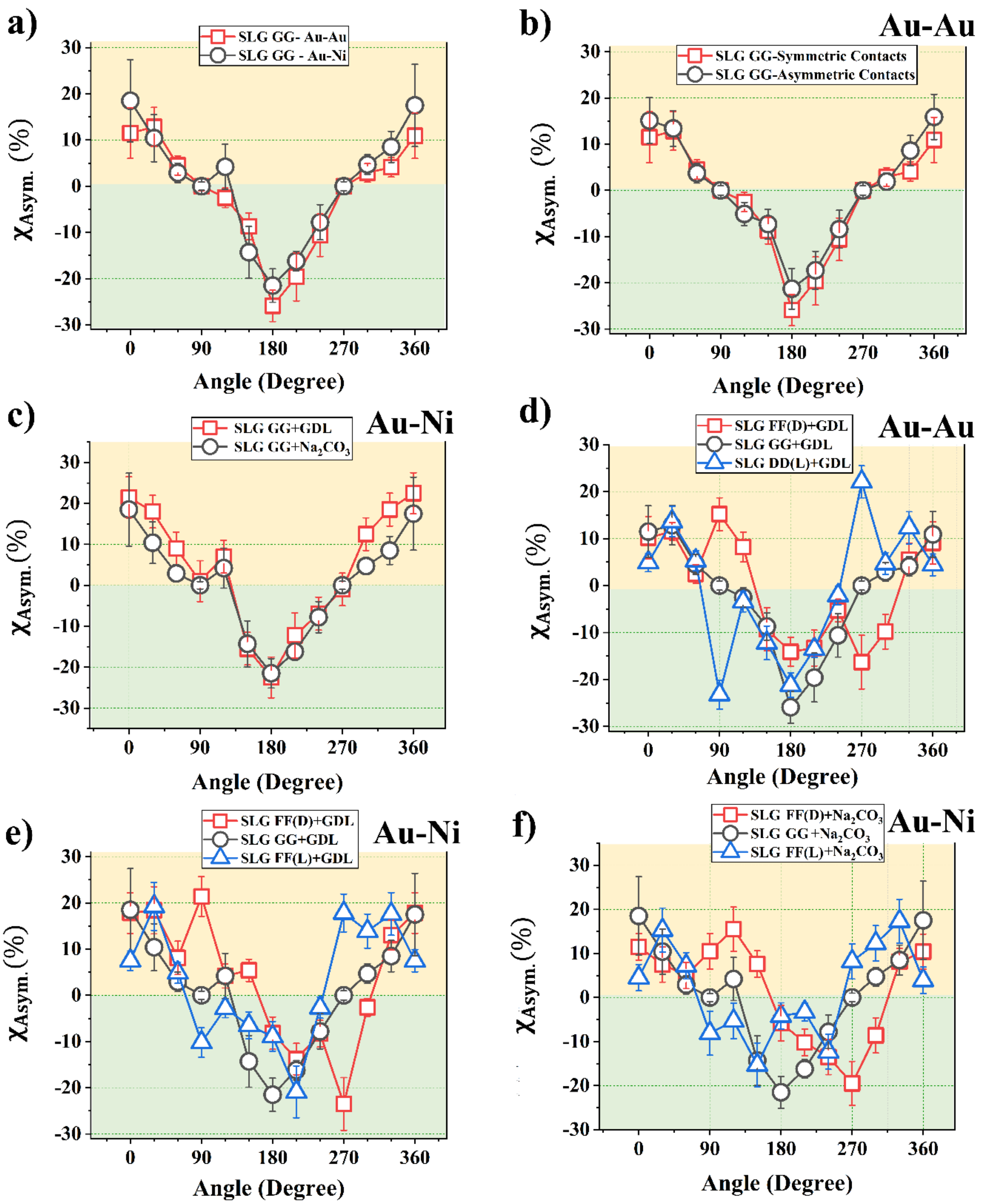

Figure B.3: **(a)** Fmoc-GG functionalized graphene samples with Au-Au and Au-Ni contacts. Nominally identical asymmetric MR responses, resembling a cos θ behavior, have been observed. **(b)** Fmoc-GG functionalized graphene samples with symmetric and asymmetric contacts. The identical MR response rules out the impact of contacts asymmetry. **(c)** Fmoc-GG functionalized graphene samples with two compounds, indicating the consistency of the results. **(d)** Fmoc-GG functionalized graphene samples with Au-Au and Au-Ni contacts. Fmoc-FF L/D functionalized graphene samples with Au-Au contacts. Chirality dependent signal has been observed at $\theta = 90^{\circ}$ and 270º. The Fmoc-GG signal with Au-Au contacts has been shown for reference. **(e)** Fmoc-FF L/D+GDL functionalized graphene samples with Au-Ni contacts. Chirality dependent signal has been observed at $\theta = 90^{\circ}$ and 270º. The Fmoc-GG signal with Au-Ni contacts has been shown for reference. **(f)** Fmoc-FF L/D+Na_2O_3 functionalized graphene samples with Au-Ni contacts. The results confirm the reproducibility of the behavior of chiral composite media in the planar contact geometry.

To explore the role of any unintentional asymmetry in contact geometry, we tested two different geometries, one with nominally symmetrical Au-Au contacts (with symmetric contact geometry and consistent contacts' gap distance), and another one with asymmetric Au-Au contacts. In both cases, nominally identical responses are obtained (Figure B.3(b)). This effectively rules out any role of contact geometry as an asymmetry source. We also tested the Fmoc-GG samples using standard Ni-Au contacts, which did not change the overall *~cos(θ)* response shown in Figure B.3(a). This effect cannot be attributed to any type of anisotropic MR in the system, which remains unchanged when the magnetic field direction is flipped.

Considering the above factors, we conclude that an asymmetric two-terminal MR can be present even in non-standard configurations, where both the contacts are non-magnetic (such as Au-Au) and the medium is achiral. Most theoretical studies predict a null CISS signal for achiral systems and/or when both electrodes are NM. However, reference [244] predicted that achiral systems properly connected with NM leads can generate spin filtering. The physical origin lies in breaking of the mirror symmetry between the left/right contact and the achiral system. While a quantitative comparison of our results with this work is not possible, absence of interfacial mirror symmetry at a microscopic level is highly likely. This could be a possible mechanism behind the observed asymmetric MR in the apparently symmetric achiral system discussed above. As depicted in Figure B.3, the results are consistent with those of Fmoc-GG+GdL, as their circular dichroism (CD) spectra do not exhibit any signs of chirality (Figure B.2(c)). It confirms the reproducibility of results for different achiral compounds.

Next, we measure two terminal MR of Fmoc-FF L/D functionalized graphene film using *Au-Au* contact pair. The measured χ_{Asym} is plotted in Figure B.3(d). The previously observed background *~cos(θ)* response is still present, *except* in the vicinity of 90° and 270°, where χ_{Asym} shows strong deviation from this background, and acquires opposite signs for opposite chiralities. Clearly, this arises due to transfer of chirality from the chiral molecules to the graphene flakes and these MR asymmetries at 90° and 270° represent CISS MR, due to their chirality dependence. This effect cannot be attributed to EMChA because for $\theta \sim 90^{\circ}, 270^{\circ}$, the chirality-dependent contribution $\alpha^{L/D}B.I \approx 0$. Further, the background *~cos(θ)* signal in this case does not flip sign for opposite chiralities, providing further evidence on the absence of EMChA. Overall, the asymmetric two-terminal MR can originate from the mirror asymmetry at the interfaces and/or the chirality of the channel, even with NM contacts.

In addition, chiral molecule adsorption on FM substrates can lead to various effects such as chirality and magnetic field dependent contact potential [239], enantiomer separation [245], pinning of magnetic domains at the interface, local enhancement of the coercive field, and reorientation of the easy axis [246]. Chiral molecular coupling with NMs has received less attention. However, coupling of chiral systems with NMs can result in a charge redistribution in the chiral system, which can produce a concomitant CISS-induced spin polarization at the interface, even under equilibrium conditions [247]. Such locally magnetic interfaces, along with the spins in the channel can result in a two-terminal MR [225]. Finally, we show the angular response of χ_{Asym} for Fmoc-FF L/D using standard Ni-Au contacts (Figure B.3(e-f)). Nominally identical CISS MR response appears in this case, as expected. This confirms that the planar geometry is superior to detect CISS MR signal compared to the vertical stacked geometry, which is prone to pinhole challenges even with addition of insulator layers. Additionally, modulating the insulator material in a vertically stacked geometry adds more complexity to the root cause of the MR signal attributed to the CISS phenomenon. [242]. Furthermore, we have shown that in planar geometry when B is perpendicular to I ($B \perp I$), the *pure* CISS MR signal emerges in either NM-NM or NM-FM terminal pair configurations. Although, the detection mechanism of CISS signal is different in these lead arrangements.

To explore the reproducibility of CISS MR behavior in planar geometry, we tested two different SLG compounds, one functionalized with FmocFF(L/D) and GG with GDL/Na_2O_3. In both cases, nominally identical responses are obtained (Figure B.3(e)(f)), as there is no change in the sign of the CD responses (Figure B.2(a)), showing the reproducibility and variability of these results.

Comparing the CISS results observed in pure chiral molecules [100, 242] to that of the chiral hybrid materials, nanotube or graphene discussed here and previous chapters, one finds some similarities as well as some differences. The differences are not unexpected, since in the hybrid case the superior conductive materials are employed as channels instead of *pure* organic molecules. In terms of similarities, both systems show chirality-dependent asymmetric MR that correlates with the CD response. In addition, in both 1D and 2D hybrid systems, a change in the supramolecular chirality results in a concomitant change in the CISS signal, which is again consistent with the *pure* molecular case [100]. In terms of magnitude or temperature dependence of device setups, we have not observed any systematic difference. In NM-FM leads configuration, the main difference is in the orientation of the Ni magnetization. It appears that the strongest CISS signal occurs when the magnetization is transverse to the current, whereas in the purely molecular case it is parallel. As discussed above, in these hybrid systems the CISS signal strength correlates with spin-orbit interaction, however, such correlation generally is not observed in *pure* chiral systems [100]. In fact, the CISS effect observed in pure chiral systems is much larger than the weak spin-orbit interaction expected in organics, and hence presence of additional mechanisms is expected [100, 101].

Overall, in this appendix, we show that molecular interaction with NMs, irrespective of their chiralities, is non-trivial, and can give rise to an asymmetric MR that mimics the CISS MR often reported in NM/Chiral media/FM devices. These results highlight the importance of NM-chiral media interface for a proper interpretation of the CISS MR, which has been overlooked so far.

References

1. Takagishi, M., et al., *The applicability of CPP-GMR heads for magnetic recording.* IEEE Transactions on Magnetics, 2002. **38**(5): p. 2277-2282.
2. Xia, B., D. Gao, and D. Xue, *Ferromagnetism of two-dimensional transition metal chalcogenides: both theoretical and experimental investigations.* Nanoscale, 2021. **13**(30): p. 12772-12787.
3. Wang, N., et al., *Transition from Ferromagnetic Semiconductor to Ferromagnetic Metal with Enhanced Curie Temperature in $Cr_2Ge_2Te_6$ via Organic Ion Intercalation.* Journal of the American Chemical Society, 2019. **141**(43).
4. Ahn, E.C., *2D materials for spintronic devices.* npj 2D Materials and Applications, 2020. **4**(1): p. 17.
5. Ali, M.N., et al., *Large, non-saturating magnetoresistance in WTe2.* Nature, 2014. **514**(7521): p. 205-208.
6. Cao, Q., et al., *Defect introduced paramagnetism and weak localization in two-dimensional metal VSe2.* Nanotechnology, 2017. **28**(47): p. 475703.
7. Bonilla, M., et al., *Strong room-temperature ferromagnetism in VSe2 monolayers on van der Waals substrates.* Nature nanotechnology, 2018. **13**(4): p. 289-293.
8. Naaman, R. and D.H. Waldeck, *Chiral-induced spin selectivity effect.* The journal of physical chemistry letters, 2012. **3**(16): p. 2178-2187.
9. Xie, Z., et al., *Spin specific electron conduction through DNA oligomers.* Nano Letters, 2011. **11**(11): p. 4652-4655.
10. Göhler, B., et al., *Spin selectivity in electron transmission through self-assembled monolayers of double-stranded DNA.* science, 2011. **331**(6019): p. 894-897.
11. Theis, T.N. and H.-S.P. Wong, *The end of moore's law: A new beginning for information technology.* Computing in science & engineering, 2017. **19**(2): p. 41-50.
12. Finocchio, G., et al., *The promise of spintronics for unconventional computing.* Journal of Magnetism and Magnetic Materials, 2021. **521**: p. 167506.
13. Guo, Z., et al., *Spintronics for energy-efficient computing: An overview and outlook.* Proceedings of the IEEE, 2021. **109**(8): p. 1398-1417.
14. Ohno, H., M.D. Stiles, and B. Dieny, *Spintronics.* Proceedings of the IEEE. Institute of Electrical and Electronics Engineers, 2016. **104**(10): p. 1782.
15. Freitas, P., et al., *Spintronic platforms for biomedical applications.* Lab on a Chip, 2012. **12**(3): p. 546-557.
16. Molina-Calderón, L., et al., *Advances of magnetic nanohydrometallurgy using superparamagnetic nanomaterials as rare earth ions adsorbents: A grand opportunity for sustainable rare earth recovery.* Separation and Purification Technology, 2022: p. 121708.
17. Knobel, M., et al., *Superparamagnetism and other magnetic features in granular materials: a review on ideal and real systems.* Journal of nanoscience and nanotechnology, 2008. **8**(6): p. 2836-2857.
18. Bonnemain, B., *Superparamagnetic agents in magnetic resonance imaging: physicochemical characteristics and clinical applications a review.* Journal of drug targeting, 1998. **6**(3): p. 167-174.
19. Feng, Y.P., et al., *Prospects of spintronics based on 2D materials.* Wiley Interdisciplinary Reviews: Computational Molecular Science, 2017. **7**(5): p. e1313.
20. Zhang, X., et al., *Room temperature magnetoresistance effects in ferroelectric poly (vinylidene fluoride) spin valves.* Journal of Materials Chemistry C, 2017. **5**(21): p. 5055-5062.
21. Firouzeh, S., et al., *Chirality-Induced Spin Selectivity in Composite Materials: A Device Perspective.* Accounts of chemical research, 2024: p. 20056-20066.

22. Hirohata, A., et al., *Review on spintronics: Principles and device applications.* Journal of Magnetism and Magnetic Materials, 2020. **509**: p. 166711.
23. Ennen, I., et al., *Giant magnetoresistance: basic concepts, microstructure, magnetic interactions and applications.* Sensors, 2016. **16**(6): p. 904.
24. Baibich, M.N., et al., *Giant magnetoresistance of (001) Fe/(001) Cr magnetic superlattices.* Physical review letters, 1988. **61**(21): p. 2472.
25. Grünberg, P.A., *Nobel Lecture: From spin waves to giant magnetoresistance and beyond.* Reviews of modern physics, 2008. **80**(4): p. 1531.
26. Reig, C., S. Cardoso, and S.C. Mukhopadhyay, *Giant magnetoresistance (GMR) sensors.* Smart Sensors, Measurement and Instrumentation, 2013. **6**(1): p. 1-301.
27. Yuasa, S. and D. Djayaprawira, *Giant tunnel magnetoresistance in magnetic tunnel junctions with a crystalline MgO (0 0 1) barrier.* Journal of Physics D: Applied Physics, 2007. **40**(21): p. R337.
28. Diény, B., *Giant magnetoresistance in spin-valve multilayers.* Journal of Magnetism and Magnetic Materials, 1994. **136**(3): p. 335-359.
29. Schliemann, J., J.C. Egues, and D. Loss, *Nonballistic spin-field-effect transistor.* Physical review letters, 2003. **90**(14): p. 146801.
30. Radisavljevic, B., et al., *Single-layer MoS2 transistors.* Nature nanotechnology, 2011. **6**(3): p. 147-150.
31. Ataca, C., H. Sahin, and S. Ciraci, *Stable, single-layer MX2 transition-metal oxides and dichalcogenides in a honeycomb-like structure.* The Journal of Physical Chemistry C, 2012. **116**(16): p. 8983-8999.
32. Giubileo, F. and A. Di Bartolomeo, *The role of contact resistance in graphene field-effect devices.* Progress in Surface Science, 2017. **92**(3): p. 143-175.
33. Novoselov, K.S., et al., *Electric field effect in atomically thin carbon films.* science, 2004. **306**(5696): p. 666-669.
34. Geim, A.K. and K.S. Novoselov, *The rise of graphene.* Nature materials, 2007. **6**(3): p. 183-191.
35. Sarno, M. and A. Troisi, *Supercapacitors based on high surface area MoS2 and MoS2–Fe3O4 nanostructures supported on physical exfoliated graphite.* Journal of nanoscience and nanotechnology, 2017. **17**(6): p. 3735-3743.
36. Lv, R., et al., *Transition metal dichalcogenides and beyond: synthesis, properties, and applications of single-and few-layer nanosheets.* Accounts of chemical research, 2015. **48**(1): p. 56-64.
37. Feng, Y., et al., *Linear magnetoresistance in the low-field limit in density-wave materials.* Proceedings of the National Academy of Sciences, 2019. **116**(23): p. 11201-11206.
38. Iqbal, M.Z., et al., *Enhanced magnetoresistance in graphene spin valve.* Journal of Magnetism and Magnetic Materials, 2017. **429**: p. 330-333.
39. Jiang, J., et al., *Signature of strong spin-orbital coupling in the large nonsaturating magnetoresistance material WTe 2.* Physical review letters, 2015. **115**(16): p. 166601.
40. Han, S.A., R. Bhatia, and S.-W. Kim, *Synthesis, properties and potential applications of two-dimensional transition metal dichalcogenides.* Nano Convergence, 2015. **2**(1): p. 1-14.
41. Lin, Y.-C., et al., *Atomic mechanism of the semiconducting-to-metallic phase transition in single-layered MoS2.* Nature nanotechnology, 2014. **9**(5): p. 391-396.
42. Wilson, J.A. and A. Yoffe, *The transition metal dichalcogenides discussion and interpretation of the observed optical, electrical and structural properties.* Advances in Physics, 1969. **18**(73): p. 193-335.
43. Mak, K.F., et al., *Atomically thin MoS 2: a new direct-gap semiconductor.* Physical review letters, 2010. **105**(13): p. 136805.
44. Gusakova, J., et al., *Electronic properties of bulk and monolayer TMDs: theoretical study within DFT framework (GVJ-2e method).* physica status solidi (a), 2017. **214**(12): p. 1700218.

45. Fiori, G., et al., *Electronics based on two-dimensional materials.* Nature nanotechnology, 2014. **9**(10): p. 768-779.
46. Liu, Y., et al., *Van der Waals heterostructures and devices.* Nature Reviews Materials, 2016. **1**(9): p. 1-17.
47. Geim, A.K. and I.V. Grigorieva, *Van der Waals heterostructures.* Nature, 2013. **499**(7459): p. 419-425.
48. Zhu, Z., et al., *Magnetoresistance and valley degree of freedom in bulk bismuth.* Journal of Physics: Condensed Matter, 2018. **30**(31): p. 313001.
49. Hossain, M., et al., *Recent advances in two-dimensional materials with charge density waves: synthesis, characterization and applications.* Crystals, 2017. **7**(10): p. 298.
50. Katzke, H., P. Tolédano, and W. Depmeier, *Phase transitions between polytypes and intralayer superstructures in transition metal dichalcogenides.* Physical Review B, 2004. **69**(13): p. 134111.
51. Kolobov, A.V. and J. Tominaga, *Two-dimensional transition-metal dichalcogenides*. Vol. 239. 2016: Springer.
52. Grüner, G., *The dynamics of charge-density waves.* Reviews of modern physics, 1988. **60**(4): p. 1129.
53. Gor'kov, L.P. and G. Grüner, *Charge density waves in solids*. 2012: Elsevier.
54. Peierls, R. and R.E. Peierls, *Quantum theory of solids*. 1955: Oxford University Press.
55. Singleton, J., *Band theory and electronic properties of solids*. Vol. 2. 2001: Oxford University Press.
56. Kittel, C. and P. McEuen, *Introduction to solid state physics*. 2018: John Wiley & Sons.
57. Feng, X., et al., *Commensurate-to-incommensurate transition of charge-density-wave order and a possible quantum critical point in pressurized kagome metal CsV3Sb5.* npj Quantum Materials, 2023. **8**(1): p. 23.
58. Fazekas, P. and E. Tosatti, *Charge carrier localization in pure and doped 1T-TaS2.* Physica B+ C, 1980. **99**(1-4): p. 183-187.
59. Van Bruggen, C. and C. Haas, *Magnetic susceptibility and electrical properties of VSe2 single crystals.* Solid State Communications, 1976. **20**(3): p. 251-254.
60. Di Salvo, F.J., D. Moncton, and J. Waszczak, *Electronic properties and superlattice formation in the semimetal TiSe 2.* Physical Review B, 1976. **14**(10): p. 4321.
61. Bayard, M. and M. Sienko, *Anomalous electrical and magnetic properties of vanadium diselenide.* Journal of solid state chemistry, 1976. **19**(4): p. 325-329.
62. Thompson, A. and B. Silbernagel, *Correlated magnetic and transport properties in the charge-density-wave states of V Se 2.* Physical Review B, 1979. **19**(7): p. 3420.
63. Rossnagel, K., *On the origin of charge-density waves in select layered transition-metal dichalcogenides.* Journal of Physics: Condensed Matter, 2011. **23**(21): p. 213001.
64. Moncton, D., J. Axe, and F. DiSalvo, *Study of superlattice formation in 2 H-Nb Se 2 and 2 H-Ta Se 2 by neutron scattering.* Physical review letters, 1975. **34**(12): p. 734.
65. Tsutsumi, K., *X-ray-diffraction study of the periodic lattice distortion associated with a charge-density wave in 1 T-V Se 2.* Physical Review B, 1982. **26**(10): p. 5756.
66. Hosen, M.M., et al., *Tunability of the topological nodal-line semimetal phase in ZrSi X-type materials (X= S, Se, Te).* Physical Review B, 2017. **95**(16): p. 161101.
67. Grasso, V., *Electronic structure and electronic transitions in layered materials.* 2012.
68. Qiao, S., et al., *Mottness Collapse in 1 T− TaS 2− x Se x Transition-Metal Dichalcogenide: An Interplay between Localized and Itinerant Orbitals.* Physical Review X, 2017. **7**(4): p. 041054.
69. Zhou, J., et al., *Large tunneling magnetoresistance in VSe2/MoS2 magnetic tunnel junction.* ACS applied materials & interfaces, 2019. **11**(19): p. 17647-17653.
70. Tan, C., et al., *Spin-Momentum Locking Induced Anisotropic Magnetoresistance in Monolayer WTe2.* Nano Letters, 2021. **21**(21): p. 9005-9011.

71. Liu, H., et al., *Observation of the kondo effect in multilayer single-crystalline VTe2 nanoplates.* Nano Letters, 2019. **19**(12): p. 8572-8580.
72. Liu, H., et al., *Quasi-2D transport and weak antilocalization effect in few-layered VSe2.* Nano Letters, 2019. **19**(7): p. 4551-4559.
73. Ashcroft, N.W. and N.D. Mermin, *Solid State Physics, Cornell University*. 1976, Saunders College Publishing, Harcourt Brace Jovanovich College Publishers ….
74. Bergmann, G., *Weak localization in thin films.* Physica Scripta, 1986. **1986**(T14): p. 99.
75. Spirito, D., et al., *Weak antilocalization and spin-orbit interaction in a two-dimensional electron gas.* Physical Review B, 2012. **85**(23): p. 235314.
76. Naylor, C.H., et al., *Monolayer single-crystal 1T′-MoTe2 grown by chemical vapor deposition exhibits weak antilocalization effect.* Nano Letters, 2016. **16**(7): p. 4297-4304.
77. Parish, M. and P. Littlewood, *Non-saturating magnetoresistance in heavily disordered semiconductors.* Nature, 2003. **426**(6963): p. 162-165.
78. Ma, Y., et al., *Evidence of the existence of magnetism in pristine VX2 monolayers (X= S, Se) and their strain-induced tunable magnetic properties.* ACS nano, 2012. **6**(2): p. 1695-1701.
79. Li, F., K. Tu, and Z. Chen, *Versatile electronic properties of VSe2 bulk, few-layers, monolayer, nanoribbons, and nanotubes: A computational exploration.* The Journal of Physical Chemistry C, 2014. **118**(36): p. 21264-21274.
80. Esters, M., R.G. Hennig, and D.C. Johnson, *Dynamic instabilities in strongly correlated VSe 2 monolayers and bilayers.* Physical Review B, 2017. **96**(23): p. 235147.
81. Manchanda, P. and R. Skomski, *2D transition-metal diselenides: phase segregation, electronic structure, and magnetism.* Journal of Physics: Condensed Matter, 2016. **28**(6): p. 064002.
82. Fuh, H.-R., et al., *Newtype single-layer magnetic semiconductor in transition-metal dichalcogenides VX2 (X= S, Se and Te).* Scientific reports, 2016. **6**(1): p. 1-11.
83. Strocov, V.N., et al., *Three-dimensional electron realm in VSe 2 by soft-x-ray photoelectron spectroscopy: Origin of charge-density waves.* Physical review letters, 2012. **109**(8): p. 086401.
84. Wang, X., et al., *Ferromagnetism in 2D vanadium diselenide.* ACS nano, 2021. **15**(10): p. 16236-16241.
85. Xu, K., et al., *Ultrathin nanosheets of vanadium diselenide: a metallic two-dimensional material with ferromagnetic charge-density-wave behavior.* Angewandte Chemie, 2013. **125**(40): p. 10671-10675.
86. Yu, W., et al., *Chemically exfoliated VSe2 monolayers with room-temperature ferromagnetism.* Advanced Materials, 2019. **31**(40): p. 1903779.
87. Xue, Y., et al., *Thickness-dependent magnetotransport properties in 1T VSe2 single crystals prepared by chemical vapor deposition.* Nanotechnology, 2020. **31**(14): p. 145712.
88. Zhu, T., et al., *Coherent growth and characterization of van der Waals 1 T− VSe 2 layers on GaAs (111) B using molecular beam epitaxy.* Physical Review Materials, 2020. **4**(8): p. 084002.
89. Coelho, P.M., et al., *Charge density wave state suppresses ferromagnetic ordering in VSe2 monolayers.* The Journal of Physical Chemistry C, 2019. **123**(22): p. 14089-14096.
90. Chen, P., et al., *Unique gap structure and symmetry of the charge density wave in single-layer VSe 2.* Physical review letters, 2018. **121**(19): p. 196402.
91. Feng, J., et al., *Electronic structure and enhanced charge-density wave order of monolayer VSe2.* Nano Letters, 2018. **18**(7): p. 4493-4499.
92. He, J., Q. Xie, and G. Xu, *Confinement effect enhanced Stoner ferromagnetic instability in monolayer 1T-VSe2.* New Journal of Physics, 2021. **23**(2): p. 023027.
93. Boukhvalov, D.W. and A. Politano, *Unveiling the origin of room-temperature ferromagnetism in monolayer VSe 2: the role of extrinsic effects.* Nanoscale, 2020. **12**(40): p. 20875-20882.

94. Zhang, Z., et al., *Van der Waals epitaxial growth of 2D metallic vanadium diselenide single crystals and their extra-high electrical conductivity.* Advanced Materials, 2017. **29**(37): p. 1702359.
95. Fumega, A.O., et al., *Absence of ferromagnetism in VSe2 caused by its charge density wave phase.* The Journal of Physical Chemistry C, 2019. **123**(45): p. 27802-27810.
96. Gong, S.-J., et al., *Electrically induced 2D half-metallic antiferromagnets and spin field effect transistors.* Proceedings of the National Academy of Sciences, 2018. **115**(34): p. 8511-8516.
97. Wu, B., et al., *High-performance spin filters and spin field effect transistors based on bilayer VSe2.* Advanced Theory and Simulations, 2021. **4**(2): p. 2000238.
98. Jafari, M., et al., *Spin valve effect in two-dimensional VSe2 system.* Journal of Magnetism and Magnetic Materials, 2022. **548**: p. 168921.
99. Yang, W., et al., *Spin-filter induced large magnetoresistance in 2D van der Waals magnetic tunnel junctions.* Nanoscale, 2021. **13**(2): p. 862-868.
100. Aiello, C.D., et al., *A chirality-based quantum leap.* ACS nano, 2022. **16**(4): p. 4989-5035.
101. Evers, F., et al., *Theory of chirality induced spin selectivity: Progress and challenges.* Advanced Materials, 2022. **34**(13): p. 2106629.
102. Yang, X., C.H. van der Wal, and B.J. van Wees, *Spin-dependent electron transmission model for chiral molecules in mesoscopic devices.* Physical Review B, 2019. **99**(2): p. 024418.
103. Rikken, G. and N. Avarvari, *Comparing Electrical Magnetochiral Anisotropy and Chirality-Induced Spin Selectivity.* The journal of physical chemistry letters, 2023. **14**(43): p. 9727-9731.
104. Rahman, M.W., et al., *Chirality-Induced Spin Selectivity in Heterochiral Short-Peptide–Carbon-Nanotube Hybrid Networks: Role of Supramolecular Chirality.* ACS nano, 2022. **16**(10): p. 16941-16953.
105. Kiran, V., et al., *Helicenes—A new class of organic spin filter.* Advanced Materials, 2016. **28**(10): p. 1957-1962.
106. Liu, T., et al., *Linear and nonlinear two-terminal spin-valve effect from chirality-induced spin selectivity.* ACS nano, 2020. **14**(11): p. 15983-15991.
107. Lu, H., et al., *Spin-dependent charge transport through 2D chiral hybrid lead-iodide perovskites.* Science advances, 2019. **5**(12): p. eaay0571.
108. Bloom, B.P., et al., *Spin selective charge transport through cysteine capped CdSe quantum dots.* Nano Letters, 2016. **16**(7): p. 4583-4589.
109. Chappert, C., A. Fert, and F.N. Van Dau, *The emergence of spin electronics in data storage.* Nature materials, 2007. **6**(11): p. 813-823.
110. Nakashima, T., Y. Kobayashi, and T. Kawai, *Optical activity and chiral memory of thiol-capped CdTe nanocrystals.* Journal of the American Chemical Society, 2009. **131**(30): p. 10342-10343.
111. Lee, H.-E., et al., *Cysteine-encoded chirality evolution in plasmonic rhombic dodecahedral gold nanoparticles.* Nature communications, 2020. **11**(1): p. 263.
112. Shi, Y., et al., *Endowing perovskite nanocrystals with circularly polarized luminescence.* Advanced Materials, 2018. **30**(12): p. 1705011.
113. Govorov, A.O., et al., *Theory of circular dichroism of nanomaterials comprising chiral molecules and nanocrystals: plasmon enhancement, dipole interactions, and dielectric effects.* Nano Letters, 2010. **10**(4): p. 1374-1382.
114. Schaaff, T.G. and R.L. Whetten, *Giant gold− glutathione cluster compounds: intense optical activity in metal-based transitions.* The Journal of Physical Chemistry B, 2000. **104**(12): p. 2630-2641.
115. Elliott, S.D., M.P. Moloney, and Y.K. Gun'ko, *Chiral shells and achiral cores in CdS quantum dots.* Nano Letters, 2008. **8**(8): p. 2452-2457.
116. Bungay, A., Y.P. Svirko, and N. Zheludev, *Experimental observation of specular optical activity.* Physical review letters, 1993. **70**(20): p. 3039.
117. Nomura, K., *Optical activity in tellurium.* Physical review letters, 1960. **5**(11): p. 500.

118. Ben-Moshe, A., A.O. Govorov, and G. Markovich, *Enantioselective synthesis of intrinsically chiral mercury sulfide nanocrystals.* Angewandte Chemie, 2013. **4**(125): p. 1313-1317.

119. Behar-Levy, H., et al., *Chirality induction in bulk gold and silver.* Advanced Materials, 2007. **19**(9): p. 1207-1211.

120. Ahn, J., et al., *A new class of chiral semiconductors: chiral-organic-molecule-incorporating organic–inorganic hybrid perovskites.* Materials Horizons, 2017. **4**(5): p. 851-856.

121. Jung, S.H., et al., *Chiral arrangement of achiral Au nanoparticles by supramolecular assembly of helical nanofiber templates.* Journal of the American Chemical Society, 2014. **136**(17): p. 6446-6452.

122. Tabassum, N., et al., *Size-dependent chiro-optical properties of CsPbBr 3 nanoparticles.* Nanoscale, 2023. **15**(5): p. 2143-2151.

123. Wang, J., B. Mao, and Z.V. Vardeny, *Chirality induced spin selectivity in chiral hybrid organic–inorganic perovskites.* The Journal of Chemical Physics, 2023. **159**(9).

124. Huizi-Rayo, U., et al., *An ideal spin filter: Long-range, high-spin selectivity in chiral helicoidal 3-dimensional metal organic frameworks.* Nano Letters, 2020. **20**(12): p. 8476-8482.

125. Qian, Q., et al., *Chiral molecular intercalation superlattices.* Nature, 2022. **606**(7916): p. 902-908.

126. Bian, Z., et al., *Hybrid Chiral MoS2 Layers for Spin-Polarized Charge Transport and Spin-Dependent Electrocatalytic Applications.* Advanced Science, 2022. **9**(17): p. 2201063.

127. Contreras-Montoya, R., et al., *Catalytic and Electron Conducting Carbon Nanotube–Reinforced Lysozyme Crystals.* Advanced Functional Materials, 2019. **29**(5): p. 1807351.

128. Zheng, M., et al., *DNA-assisted dispersion and separation of carbon nanotubes.* Nature materials, 2003. **2**(5): p. 338-342.

129. Perlitz, Y. and K. Michaeli, *Helical liquid in carbon nanotubes wrapped with DNA molecules.* Physical Review B, 2018. **98**(19): p. 195405.

130. Alam, K.M. and S. Pramanik, *Spin Filtering through Single-Wall Carbon Nanotubes Functionalized with Single-Stranded DNA.* Advanced Functional Materials, 2015. **25**(21): p. 3210-3218.

131. Alam, K.M. and S. Pramanik, *Spin filtering with poly-T wrapped single wall carbon nanotubes.* Nanoscale, 2017. **9**(16): p. 5155-5163.

132. Rahman, M.W., K.M. Alam, and S. Pramanik, *Long carbon nanotubes functionalized with DNA and implications for spintronics.* ACS omega, 2018. **3**(12): p. 17108-17115.

133. Rahman, M.W., et al., *Carrier transport engineering in carbon nanotubes by chirality-induced spin polarization.* ACS nano, 2020. **14**(3): p. 3389-3396.

134. Rahman, M.W., S. Firouzeh, and S. Pramanik, *Carrier localization and magnetoresistance in DNA-functionalized carbon nanotubes.* Nanotechnology, 2021. **32**(45): p. 455001.

135. Rahman, M.W., et al., *Molecular functionalization and emergence of long-range spin-dependent phenomena in two-dimensional carbon nanotube networks.* ACS nano, 2021. **15**(12): p. 20056-20066.

136. Adams, D.J., et al., *A new method for maintaining homogeneity during liquid–hydrogel transitions using low molecular weight hydrogelators.* Soft Matter, 2009. **5**(9): p. 1856-1862.

137. Wang, Z., et al., *Very large tunneling magnetoresistance in layered magnetic semiconductor CrI3.* Nature communications, 2018. **9**(1): p. 2516.

138. Bass, J., *CPP magnetoresistance of magnetic multilayers: A critical review.* Journal of Magnetism and Magnetic Materials, 2016. **408**: p. 244-320.

139. Voiry, D., A. Mohite, and M. Chhowalla, *Phase engineering of transition metal dichalcogenides.* Chemical Society Reviews, 2015. **44**(9): p. 2702-2712.

140. Kwak, J.Y., et al., *Electrical characteristics of multilayer MoS2 FET's with MoS2/graphene heterojunction contacts.* Nano Letters, 2014. **14**(8): p. 4511-4516.

141. Li, H., et al., *From bulk to monolayer MoS2: evolution of Raman scattering.* Advanced Functional Materials, 2012. **22**(7): p. 1385-1390.
142. Yang, J., et al., *Thickness dependence of the charge-density-wave transition temperature in VSe2.* Applied Physics Letters, 2014. **105**(6): p. 063109.
143. Toriumi, A. and S. Tanaka, *Galvanomagnetic properties of 1T-VSe2.* Physica B+ C, 1981. **105**(1-3): p. 141-145.
144. Terashima, K., et al., *Charge-density wave transition of 1 T− V S e 2 studied by angle-resolved photoemission spectroscopy.* Physical Review B, 2003. **68**(15): p. 155108.
145. Sato, T., et al., *Three-Dimensional Fermi-Surface Nesting in 1 T-VSe2 Studied by Angle-Resolved Photoemission Spectroscopy.* journal of the physical society of japan, 2004. **73**(12): p. 3331-3334.
146. Sun, Y., et al., *Memristive phase switching in two-dimensional 1T′-VSe2 crystals.* Applied Physics Letters, 2020. **116**(3): p. 033101.
147. Sugai, S., et al., *INVESTIGATION OF THE CHARGE DENSITY WAVES IN 2H-TaSe2 BY ONE AND TWO PHONON RAMAN SCATTERING.* Le Journal de Physique Colloques, 1981. **42**(C6): p. C6-728-C6-730.
148. Pandey, J. and A. Soni, *Electron-phonon interactions and two-phonon modes associated with charge density wave in single crystalline 1 T− V Se 2.* Physical Review Research, 2020. **2**(3): p. 033118.
149. Abrikosov, A., *Quantum magnetoresistance.* Physical Review B, 1998. **58**(5): p. 2788.
150. Abrikosov, A., *Quantum linear magnetoresistance.* EPL (Europhysics Letters), 2000. **49**(6): p. 789.
151. Kawabata, A., *Positive magnetoresistance induced by Zeeman splitting in two-dimensional systems.* journal of the physical society of japan, 1981. **50**(8): p. 2461-2462.
152. Klein, D.R., et al., *Probing magnetism in 2D van der Waals crystalline insulators via electron tunneling.* science, 2018. **360**(6394): p. 1218-1222.
153. Kim, H.H., et al., *One million percent tunnel magnetoresistance in a magnetic van der Waals heterostructure.* Nano Letters, 2018. **18**(8): p. 4885-4890.
154. Song, T., et al., *Giant tunneling magnetoresistance in spin-filter van der Waals heterostructures.* science, 2018. **360**(6394): p. 1214-1218.
155. Kim, H.H., et al., *Tailored tunnel magnetoresistance response in three ultrathin chromium trihalides.* Nano Letters, 2019. **19**(8): p. 5739-5745.
156. Parish, M.M. and P.B. Littlewood, *Classical magnetotransport of inhomogeneous conductors.* Physical Review B, 2005. **72**(9): p. 094417.
157. Hu, J., M.M. Parish, and T. Rosenbaum, *Nonsaturating magnetoresistance of inhomogeneous conductors: comparison of experiment and simulation.* Physical Review B, 2007. **75**(21): p. 214203.
158. Jin, Z., et al., *Strong charge-density-wave order of large-area 2D metallic VSe2 nanosheets discovered by temperature-dependent Raman spectra.* Applied Physics Letters, 2020. **116**(3): p. 033102.
159. Pásztor, Á., et al., *Dimensional crossover of the charge density wave transition in thin exfoliated VSe2.* 2D Materials, 2017. **4**(4): p. 041005.
160. Michaeli, K., et al., *A new approach towards spintronics–spintronics with no magnets.* Journal of Physics: Condensed Matter, 2017. **29**(10): p. 103002.
161. Liu, Y., et al., *Chirality-driven topological electronic structure of DNA-like materials.* Nature materials, 2021. **20**(5): p. 638-644.
162. Atzori, M., et al., *Magneto-chiral anisotropy: From fundamentals to perspectives.* Chirality, 2021. **33**(12): p. 844-857.
163. Xiao, J. and B. Yan, *Nonreciprocal Nature and Magnetochiral Charge Polarization in Chiral Molecular Devices.* arXiv preprint arXiv:2201.03623, 2022.
164. Hossain, M.A., et al., *Transverse magnetoconductance in two-terminal chiral spin-selective devices.* Nanoscale Horizons, 2023. **8**(3): p. 320-330.

165. Ando, T., *Spin-orbit interaction in carbon nanotubes.* journal of the physical society of japan, 2000. **69**(6): p. 1757-1763.
166. Huertas-Hernando, D., F. Guinea, and A. Brataas, *Spin-orbit coupling in curved graphene, fullerenes, nanotubes, and nanotube caps.* Physical Review B, 2006. **74**(15): p. 155426.
167. Jeong, J.-S. and H.-W. Lee, *Curvature-enhanced spin-orbit coupling in a carbon nanotube.* Physical Review B, 2009. **80**(7): p. 075409.
168. Kuemmeth, F., et al., *Coupling of spin and orbital motion of electrons in carbon nanotubes.* Nature, 2008. **452**(7186): p. 448-452.
169. Cousins, B.G., et al., *Enzyme-activated surfactants for dispersion of carbon nanotubes.* Small, 2009. **5**(5): p. 587-590.
170. Piao, Y., et al., *Comparative study of multiwall carbon nanotube nanocomposites by Raman, SEM, and XPS measurement techniques.* Composites Science and Technology, 2021. **208**: p. 108753.
171. Zdrojek, M., et al., *Studies of multiwall carbon nanotubes using Raman spectroscopy and atomic force microscopy.* Solid State Phenomena, 2004. **99**: p. 265-268.
172. Kim, G., et al., *Magnetoresistance of an entangled single-wall carbon-nanotube network.* Physical Review B, 1998. **58**(24): p. 16064.
173. Baumgartner, G., et al., *Hall effect and magnetoresistance of carbon nanotube films.* Physical Review B, 1997. **55**(11): p. 6704.
174. Jaiswal, M., et al., *Magnetotransport in transparent single-wall carbon nanotube networks.* Physical Review B, 2007. **76**(11): p. 113401.
175. Yanagi, K., et al., *Transport mechanisms in metallic and semiconducting single-wall carbon nanotube networks.* ACS nano, 2010. **4**(7): p. 4027-4032.
176. Ksenevich, V., J. Galibert, and V. Samuilov, *Charge transport in carbon nanotube films and fibers*. 2010: IntechOpen.
177. Kaiser, A., G. Düsberg, and S. Roth, *Heterogeneous model for conduction in carbon nanotubes.* Physical Review B, 1998. **57**(3): p. 1418.
178. Lee, S.H., et al., *Hall effect in carbon nanotube thin films.* Synthetic Metals, 2014. **198**: p. 84-87.
179. Song, S.N., et al., *Electronic properties of graphite nanotubules from galvanomagnetic effects.* Physical review letters, 1994. **72**(5): p. 697.
180. Langer, L., et al., *Electrical resistance of a carbon nanotube bundle.* Journal of Materials Research, 1994. **9**(4): p. 927-932.
181. Maity, K.P. and V. Prasad, *Effect of chemical functionalization on charge transport of multiwall carbon nanotube.* Materials Research Express, 2019. **6**(8): p. 0850a2.
182. Bachtold, A., et al., *Aharonov–Bohm oscillations in carbon nanotubes.* Nature, 1999. **397**(6721): p. 673-675.
183. Schoenenberger, C., et al., *Interference and Interaction in multi-wall carbon nanotubes.* Applied Physics A, 1999. **69**: p. 283-295.
184. Hueso, L.E., et al., *Transformation of spin information into large electrical signals using carbon nanotubes.* Nature, 2007. **445**(7126): p. 410-413.
185. Liu, M., L. Zhang, and T. Wang, *Supramolecular chirality in self-assembled systems.* Chemical reviews, 2015. **115**(15): p. 7304-7397.
186. Liu, G.F., et al., *Inversion of the Supramolecular Chirality of Nanofibrous Structures through Co-Assembly with Achiral Molecules.* Angewandte Chemie International Edition, 2016. **55**(7): p. 2411-2415.
187. Yue, B. and L. Zhu, *Dynamic modulation of supramolecular chirality driven by factors from internal to external levels.* Chemistry–An Asian Journal, 2019. **14**(13): p. 2172-2180.
188. Gong, Y., et al., *Chirality Inversion in Self-Assembled Nanocomposites Directed by Curvature-Mediated Interactions.* Angewandte Chemie International Edition, 2022. **61**(10): p. e202117406.

189. Gila-Vilchez, C., et al., *Insights into the co-assemblies formed by different aromatic short-peptide amphiphiles.* Polymer Chemistry, 2021. **12**(47): p. 6832-6845.
190. Geim, A.K., *Graphene: status and prospects.* science, 2009. **324**(5934): p. 1530-1534.
191. Novoselov, K.S., et al., *Room-temperature quantum Hall effect in graphene.* science, 2007. **315**(5817): p. 1379-1379.
192. Tombros, N., et al., *Electronic spin transport and spin precession in single graphene layers at room temperature.* Nature, 2007. **448**(7153): p. 571-574.
193. Han, W., et al., *Graphene spintronics.* Nature nanotechnology, 2014. **9**(10): p. 794-807.
194. Qing, G., et al., *Chiral effect at protein/graphene interface: a bioinspired perspective to understand amyloid formation.* Journal of the American Chemical Society, 2014. **136**(30): p. 10736-10742.
195. Guo, L., et al., *The application of thionine–graphene nanocomposite in chiral sensing for tryptophan enantiomers.* Bioelectrochemistry, 2013. **94**: p. 87-93.
196. Cheng, Q., et al., *Chiral graphene materials for enantiomer separation.* Chemical Engineering Journal, 2023. **452**: p. 139499.
197. Zhao, B., et al., *Chiral graphene hybrid materials: structures, properties, and chiral applications.* Advanced Science, 2021. **8**(7): p. 2003681.
198. Azlouk, M., et al., *Graphene-based recyclable and bifunctional heterogeneous chiral catalyst for direct asymmetric aldol reaction.* Materials Chemistry and Physics, 2020. **239**: p. 122298.
199. Mao, X., et al., *Highly sensitive chiral recognition of amino propanol in serum with R-mandelic acid-linked calix [4] arene modified graphene.* Journal of Materials Chemistry C, 2015. **3**(6): p. 1325-1329.
200. Huang, H., et al., *Preparation of chiral graphene oxides by covalent attachment of chiral cysteines for voltammetric recognition of tartrates.* Microchimica Acta, 2019. **186**: p. 1-9.
201. Shang, X., et al., *Highly enantioselective graphene-based chemical sensors prepared by chiral noncovalent functionalization.* ACS applied materials & interfaces, 2018. **10**(42): p. 36194-36201.
202. Suzuki, N., et al., *Chiral graphene quantum dots.* ACS nano, 2016. **10**(2): p. 1744-1755.
203. Furlan de Oliveira, R., et al., *Liquid-gated transistors based on reduced graphene oxide for flexible and wearable electronics.* Advanced Functional Materials, 2019. **29**(46): p. 1905375.
204. Fowler, J.D., et al., *Practical chemical sensors from chemically derived graphene.* ACS nano, 2009. **3**(2): p. 301-306.
205. Eda, G., G. Fanchini, and M. Chhowalla, *Large-area ultrathin films of reduced graphene oxide as a transparent and flexible electronic material.* Nature nanotechnology, 2008. **3**(5): p. 270-274.
206. Zheng, M., et al., *Structure-based carbon nanotube sorting by sequence-dependent DNA assembly.* science, 2003. **302**(5650): p. 1545-1548.
207. Jayawarna, V., et al., *Nanostructured hydrogels for three-dimensional cell culture through self-assembly of fluorenylmethoxycarbonyl-dipeptides.* Advanced Materials, 2006. **18**(5): p. 611-614.
208. Mañas-Torres, M.C., et al., *In situ real-time monitoring of the mechanism of self-assembly of short peptide supramolecular polymers.* Materials Chemistry Frontiers, 2021. **5**(14): p. 5452-5462.
209. Firouzeh, S., et al., *Chirality-induced spin selectivity in functionalized carbon nanotube networks: The role of spin–orbit coupling.* The Journal of Chemical Physics, 2023. **159**(3).
210. Contreras-Montoya, R., et al., *Iron nanoparticles-based supramolecular hydrogels to originate anisotropic hybrid materials with enhanced mechanical strength.* Materials Chemistry Frontiers, 2018. **2**(4): p. 686-699.
211. Illescas-Lopez, S., et al., *Short-peptide supramolecular hydrogels for in situ growth of metal–organic framework-peptide biocomposites.* ACS applied materials & interfaces, 2023. **15**(27): p. 32597-32609.

212. Fichman, G., et al., *Seamless metallic coating and surface adhesion of self-assembled bioinspired nanostructures based on di-(3, 4-dihydroxy-L-phenylalanine) peptide motif.* ACS nano, 2014. **8**(7): p. 7220-7228.
213. Mañas-Torres, M.C., et al., *Organic/Inorganic hydrogels by simultaneous self-assembly and mineralization of aromatic short-peptides.* Inorganic Chemistry Frontiers, 2022. **9**(4): p. 743-752.
214. Malard, L.M., et al., *Raman spectroscopy in graphene.* Physics reports, 2009. **473**(5-6): p. 51-87.
215. Wang, X.Y., et al. *Thermoelectric enhancement of polyaniline grafting from graphene oxide*. in *Materials Science Forum*. 2016: Trans Tech Publ.
216. Zhang, K., et al., *Analysis of carboxylate groups in oxidized never-dried cellulose II catalyzed by TEMPO and 4-acetamide-TEMPO.* Carbohydrate polymers, 2012. **87**(1): p. 894-900.
217. Abid, et al., *Reduced graphene oxide (rGO) based wideband optical sensor and the role of Temperature, Defect States and Quantum Efficiency.* Scientific reports, 2018. **8**(1): p. 3537.
218. Iacovella, F., et al., *Magneto-transport properties of a random distribution of few-layer graphene patches.* Journal of Applied Physics, 2014. **116**(19).
219. Kaiser, A.B., et al., *Electrical conduction mechanism in chemically derived graphene monolayers.* Nano Letters, 2009. **9**(5): p. 1787-1792.
220. Gómez-Navarro, C., et al., *Electronic transport properties of individual chemically reduced graphene oxide sheets.* Nano Letters, 2007. **7**(11): p. 3499-3503.
221. Eda, G., et al., *Insulator to semimetal transition in graphene oxide.* The Journal of Physical Chemistry C, 2009. **113**(35): p. 15768-15771.
222. Joung, D., L. Zhai, and S.I. Khondaker, *Coulomb blockade and hopping conduction in graphene quantum dots array.* Physical Review B, 2011. **83**(11): p. 115323.
223. Pichard, J.-L., et al., *Broken symmetries and localization lengths in Anderson insulators: Theory and experiment.* Physical review letters, 1990. **65**(14): p. 1812.
224. Bloom, B.P., et al., *Chirality control of electron transfer in quantum dot assemblies.* Journal of the American Chemical Society, 2017. **139**(26): p. 9038-9043.
225. Dalum, S. and P. Hedegård, *Theory of chiral induced spin selectivity.* Nano Letters, 2019. **19**(8): p. 5253-5259.
226. Ortuño, A.M., et al., *Extended enantiopure ortho-phenylene ethylene (o-OPE)-based helical systems as scaffolds for supramolecular architectures: a study of chiroptical response and its connection to the CISS effect.* Organic Chemistry Frontiers, 2021. **8**(18): p. 5071-5086.
227. Ortuño, A.M., et al., *Chiral Single-Molecule Potentiometers Based on Stapled ortho-Oligo (phenylene) ethynylenes.* Angewandte Chemie, 2023. **135**(16): p. e202218640.
228. Liu, T., et al., *Spin selectivity through chiral polyalanine monolayers on semiconductors.* arXiv preprint arXiv:2001.00097, 2019.
229. Feicht, P. and S. Eigler, *Defects in graphene oxide as structural motifs.* ChemNanoMat, 2018. **4**(3): p. 244-252.
230. Augustyniak-Jabłokow, M.A., et al., *Electron spin echo studies of hydrothermally reduced graphene oxide.* The Journal of Physical Chemistry C, 2021. **125**(7): p. 4102-4109.
231. Neto, A.C. and F. Guinea, *Impurity-induced spin-orbit coupling in graphene.* Physical review letters, 2009. **103**(2): p. 026804.
232. Gmitra, M., D. Kochan, and J. Fabian, *Spin-orbit coupling in hydrogenated graphene.* Physical review letters, 2013. **110**(24): p. 246602.
233. Ertler, C., et al., *Electron spin relaxation in graphene: The role of the substrate.* Physical Review B, 2009. **80**(4): p. 041405.
234. Sofo, J., et al., *Magnetic structure of hydrogen-induced defects on graphene.* Physical Review B, 2012. **85**(11): p. 115405.

235. Kulkarni, C., et al., *Highly efficient and tunable filtering of Electrons' spin by supramolecular chirality of nanofiber-based materials.* Advanced Materials, 2020. **32**(7): p. 1904965.
236. Li, D., et al., *Structural phase transition of multilayer VSe2.* ACS applied materials & interfaces, 2020. **12**(22): p. 25143-25149.
237. Saito, R., et al., *Raman spectroscopy of transition metal dichalcogenides.* Journal of Physics: Condensed Matter, 2016. **28**(35): p. 353002.
238. Zhang, X., et al., *Phonon and Raman scattering of two-dimensional transition metal dichalcogenides from monolayer, multilayer to bulk material.* Chemical Society Reviews, 2015. **44**(9): p. 2757-2785.
239. Ghosh, S., et al., *Effect of chiral molecules on the electron's spin wavefunction at interfaces.* The journal of physical chemistry letters, 2020. **11**(4): p. 1550-1557.
240. Tirion, S.H. and B.J. van Wees, *Mechanism for Electrostatically Generated Magnetoresistance in Chiral Systems without Spin-Dependent Transport.* ACS nano, 2024.
241. Liu, T. and P.S. Weiss, *Spin Polarization in Transport Studies of Chirality-Induced Spin Selectivity.* ACS nano, 2023. **17**(20): p. 19502-19507.
242. Das, T.K., R. Naaman, and J. Fransson, *Insights into the Mechanism underlying the Chiral-Induced Spin Selectivity: The effect of an Angle-Dependent Magnetic Field and Temperature.* arXiv preprint arXiv:2312.15466, 2023.
243. Karunakaran, S.C., et al., *Spontaneous symmetry breaking in the formation of supramolecular polymers: implications for the origin of biological homochirality.* Angewandte Chemie, 2019. **131**(5): p. 1467-1471.
244. Guo, A.-M., et al., *Spin selectivity effect in achiral molecular systems.* Physical Review B, 2016. **94**(16): p. 165409.
245. Banerjee-Ghosh, K., et al., *Separation of enantiomers by their enantiospecific interaction with achiral magnetic substrates.* science, 2018. **360**(6395): p. 1331-1334.
246. Kapon, Y., et al., *Magneto-optical imaging of magnetic-domain pinning induced by chiral molecules.* The Journal of Chemical Physics, 2023. **159**(6).
247. Fransson, J., *Charge redistribution and spin polarization driven by correlation induced electron exchange in chiral molecules.* Nano Letters, 2021. **21**(7): p. 3026-3032.